

THE UNIVERSITY OF MANITOBA

PRECIPITATION BEHAVIOUR IN THE Al-1.5%Cu-0.75%Mg ALLOY

By

ALOK KUMAR GUPTA

A Dissertation Submitted to the Faculty of
Graduate Studies of the University of Manitoba
in Partial Fulfillment of the Requirements of the Degree of

DOCTOR OF PHILOSOPHY

DEPARTMENT OF MECHANICAL ENGINEERING
METALLURGY

Winnipeg, Manitoba

 MAY, 1987

Permission has been granted to the National Library of Canada to microfilm this thesis and to lend or sell copies of the film.

The author (copyright owner) has reserved other publication rights, and neither the thesis nor extensive extracts from it may be printed or otherwise reproduced without his/her written permission.

L'autorisation a été accordée à la Bibliothèque nationale du Canada de microfilmer cette thèse et de prêter ou de vendre des exemplaires du film.

L'auteur (titulaire du droit d'auteur) se réserve les autres droits de publication; ni la thèse ni de longs extraits de celle-ci ne doivent être imprimés ou autrement reproduits sans son autorisation écrite.

ISBN 0-315-48064-5

PRECIPITATION BEHAVIOUR IN THE Al-1.5% Cu-0.75% Mg ALLOY

BY

ALOK KUMAR GUPTA

A thesis submitted to the Faculty of Graduate Studies of
the University of Manitoba in partial fulfillment of the requirements
of the degree of

DOCTOR OF PHILOSOPHY

© 198

Permission has been granted to the LIBRARY OF THE UNIVERSITY OF MANITOBA to lend or sell copies of this thesis, to the NATIONAL LIBRARY OF CANADA to microfilm this thesis and to lend or sell copies of the film, and UNIVERSITY MICROFILMS to publish an abstract of this thesis.

The author reserves other publication rights, and neither the thesis nor extensive extracts from it may be printed or otherwise reproduced without the author's written permission.

ABSTRACT

The precipitation strengthening of Al-Cu-Mg alloys with a Cu/Mg ratio close to 2.2:1 has been attributed primarily to the precipitation of the orthorhombic S' phase. However, very little is known about the precipitation process in dilute Al-Cu-Mg alloy in terms of the kinetic parameters controlling the precipitation rates and the effect of Si additions on them. Therefore, a series of dilute Al-1.5%Cu-0.75%Mg alloys containing 0, 0.23, 0.49, 0.76 and 1.03% Si were chosen to study their precipitation behaviour by transmission electron microscopy (TEM) and differential scanning calorimetry (DSC).

The alloys were solution treated and water quenched, stabilized at room temperature for 48 h and further aged at 130° and 190°C. TEM studies on the Si-free alloy showed that on ageing at 130° and 190°, S' precipitates nucleated on dislocation loops and helical dislocations and grew as rods parallel to $\langle 100 \rangle_M$ matrix directions with a slight tendency to cluster in groups on $\{110\}_M$ matrix planes. These groups of precipitates did not however coalesce to form laths on the $\{110\}_M$ or $\{210\}_M$ matrix planes as has been reported in more concentrated alloys with similar Cu/Mg ratios. The orientation relationships determined from the x-ray investigations were used to simulate a detailed and complete S' phase diffraction pattern which was consistent with the morphology and crystal structure. Measurements of relative changes in lattice parameters suggested that the S' phase is simply a strained version of the equilibrium S phase. With increase in the time of ageing at 190°C the b lattice parameter of the S' phase increased significantly and the c value declined without any change

in the cell volume. Grouping of rods on $\{110\}_M$ fcc matrix planes were explained on the basis of expansion of the b parameter and contraction of the c parameter.

The kinetics of the precipitation processes were studied by using differential scanning calorimetry (DSC). Various exothermic and endothermic DSC peaks were associated with specific precipitation and dissolution processes. Appropriate equations were developed to calculate the heat effects, mole fractions and reactions rates of the processes which occurred at heating rates 5°, 10°, 15° and 20°C/min. The first exothermic (25°-170°C) and endothermic (140°-240°C) peaks were found to be due to precipitation of GPB zones and dissolution of Guinier-Preston-Bagaryatsky (GPB) zones and complexes respectively. The second exothermic (253°-367°C) and endothermic (380°-434°C) peaks were associated with the precipitation and dissolution respectively of the S' phase. Except the process of dissolution of the S' phase, all others were found to be kinematically controlled processes. The dissolution of S' phase was interpreted as a thermodynamically controlled process. All the kinematically controlled processes were analysed for the determination of activation energy for each process using the following relationship

$$\frac{dY}{dt} = f(Y) K_0 e^{-Q^*/RT}$$

The expression for $f(Y)$ was $(1-Y)$ for all the peaks analysed. The activation energy, Q^* , and the value of K_0 for the precipitation and dissolution of GPB zones were determined to be 55.6 kJ/mole, $5.7 \times 10^5 \text{ s}^{-1}$, 123.9 kJ/mole and $1.1 \times 10^{10} \text{ s}^{-1}$ respectively. These results were found to be in good agreement with the published

information. The Q^* and K_0 values for the precipitation of the S' phase were 129.9 kJ/moles and $2.7 \times 10^9 \text{ s}^{-1}$ respectively.

The addition of Si $\geq 0.49\%$ caused the formation of insoluble particles. The back scattered scanning electron microscopic images of the polished sections of the alloys showed the presence of very small particles of nearly spherical shape at the grain boundaries of the alloys except the one that contained 0.23% Si. Alloys with 0.76 and 1.03% Si also contained large particles of well defined geometrical shapes. The volume percentage of insolubles in the 1.03% Si alloy was 1.34. An electrolytic technique was used to extract the insolubles from the matrix. The extracted particles were analysed by energy dispersive x-ray analysis in SEM. They contained $20.6 \pm 0.4\%$ Cu, $32.6 \pm 0.4\%$ Mg, $30.2 \pm 0.4\%$ Si and $16.6 \pm 0.1\%$ Al by weight. X-ray diffraction analysis of these particles showed that they have a hexagonal structure with a and c parameters of $1.036 \pm 0.004 \text{ nm}$ and $0.404 \pm 0.004 \text{ nm}$ respectively. The insoluble particles were identified as the quaternary phase, Q. Ageing for extended periods of time at 190°C did not alter the composition or morphology of the insoluble particles. The presence of insoluble particles changed the solute contents of the matrix so that the Cu, Mg and Si contents 1.45, 0.63 and 0.39% respectively in the 0.49% Si alloy to 1.16, 0.05 and 0.44% in the 1.03% Si. The Cu/Mg ratio also changed from 2 in 0.23% Si alloy to 23 in 1.03% Si alloy.

The Al-1.52%Cu-0.74%Mg alloy which retained 0.23% Si in solid solution exhibited precipitation of the S' phase like the Si free alloy. At Si concentrations of 0.49% and greater, the matrix became depleted in solute due to the formation of the Q phase

($\text{Al}_5\text{Cu}_2\text{Mg}_8\text{Si}_6$) and the subsequent precipitation behaviour changed. The TEM microstructure of the aged alloy containing 0.49% Si showed three kinds of precipitates. One of them was found to be plate shaped θ' phase while the other two had small needle-like and square shaped morphology. The alloy containing 1.03% Si also showed plate type θ' phase along with needle-like and dot shaped precipitates. Ageing of this alloy for extended time (1000 h) at 190°C resulted in a more complex structure.

ACKNOWLEDGEMENTS

I was fortunate in having Prof. M.C. Chaturvedi as my thesis advisor. He provided excellent supervision and unique support throughout the period of my research. He gave me the opportunity to work in my own way but helped me so that I could conduct some of my experiments outside the Department. I wish to express my sincere gratitude to him.

I shall remain indebted to Prof. A.K. Jena, Department of Metallurgical Engineering, IIT, Kanpur, India and Prof. P. Gaunt, Physics Department, University of Manitoba, for their immense help and valuable guidance. Their suggestions broadened my horizons and gave me a better understanding of the problem. I wish to express my sincere gratitude to both. I am grateful to Dr. D.J. Lloyd and Prof. J.R. Cahoon for their keen interest in my work and their valuable suggestions.

The co-operation extended to me by John Van Dorp, Don Mardis and Roy Hartle during the course of this investigation is greatly appreciated. I would like to thank all the graduate students of this Department and my friends who were always willing to help.

I wish to thank Prof. E.D. Murray, Food Science Department, University of Manitoba, for allowing me to use the DSC facility and S. Arntfield for providing me the necessary help with the DSC experiments. My sincere thanks are due to Neil Ball, Earth Science Department, University of Manitoba, for his co-operation and help with the x-ray experiments.

I wish to express my appreciation to Horst Weiss for his

excellent drafting work. Mrs. Ingrid K. Trestrail has done an excellent job in typing this thesis within the limited time of one week. My sincere thank are due to her.

I will fail in fulfilling my duty if I did not thank my family and Prof. A.K. Jena and his family for their encouragement during the course of this study.

The funding provided by NSERC through grants to Prof. M.C. Chaturvedi is gratefully acknowledged.

Finally, I pursued the Ph.D. program to fulfill the ambitions of my parents. I wish to dedicate this thesis to them.

TABLE OF CONTENTS

	<u>Page</u>
ABSTRACT	i
ACKNOWLEDGEMENTS	v
TABLE OF CONTENTS	vii
CHAPTER I INTRODUCTION	1
CHAPTER II LITERATURE REVIEW	4
2.1 THEORY OF PRECIPITATION IN SOLIDS	4
2.1.1 Nucleation of precipitates	6
2.1.2 Growth of precipitates	11
2.1.3 Transformation kinetics	12
2.1.4 Factors influencing the activation energy of transformation	14
2.1.4.1 Interfacial energy	14
2.1.4.2 Strain energy	15
2.1.4.3 Hetrogeneous nucleation sites	16
2.1.4.4 Quenched-in vacancies	16
2.1.5 Formation of transition phases and the precipitation sequence	21
2.2 PRECIPITATION IN THE BINARY Al-Cu ALLOY	24
2.2.1 GP(I) zones	27
2.2.2 GP(II) zones (or θ'' phase)	32
2.2.3 The θ' phase	41
2.2.4 The θ phase (CuAl_2)	48
2.3 PRECIPITATION IN THE BINARY Al-Mg ALLOY	51
2.3.1 GP zones	51
2.3.2 The β' phase	53
2.3.3 The β phase	54
2.4 PRECIPITATION IN THE TERNARY Al-Cu-Mg ALLOY	54
2.4.1 GPB(I) zones	58
2.4.2 GPB(II) zones	61
2.4.3 The S' phase	63
2.4.4 The S phase	65
2.4.5 The distinction between S' and S phases	66
2.4.6 Effect of precipitation on hardness and tensile properties	67

	<u>Page</u>
2.5 EFFECT OF SMALL QUARTERNARY ADDITIONS ON THE PRECIPITATION BEHAVIOUR OF Al-Cu-Mg ALLOYS	70
2.5.1 Silver	71
2.5.2 Transition elements, Ti, Mn, Fe and Ni	72
2.5.3 Silicon	72
2.6 SCOPE OF THE PRESENT WORK	77
CHAPTER III EXPERIMENTAL TECHNIQUES AND PROCEDURE	80
3.1 MATERIALS AND PROCESSING	80
3.2 EXTRACTION OF INSOLUBLE PARTICLES	82
3.3 OPTICAL MICROSCOPY	83
3.4 ELECTRON MICROSCOPY	83
3.4.1 Transmission electron microscopy	83
3.4.2 Scanning electron microscopy	84
3.4.2.1 Chemical analysis	84
3.4.2.2 Volume fraction of insoluble particles	85
3.5 DIFFERENTIAL SCANNING CALORIMETRY (DSC)	85
3.6 X-RAY DIFFRACTION	88
3.7 DENSITY MEASUREMENTS	88
CHAPTER IV PRECIPITATION IN THE Al-1.50%Cu-0.75%Mg ALLOY ..	90
4.1 MICROSTRUCTURAL CHARACTERIZATION	90
4.1.1 Initial stages of ageing: defect structure and GPB zones	90
4.1.2 Formation of the S' phase	97
4.1.2.1 Nucleation of the S' phase	100
4.1.2.2 Theoretical predictions of the electron diffraction pattern of the S' phase ...	100
4.1.2.3 Analysis of the SAD patterns and the morphology of the S' phase	112
4.1.2.3.1 Morphology from bright field images	112
4.1.2.3.2 Interpretation of dark field (CDF) images	113
4.1.2.3.3 Effect of ageing on the lattice parameters of the S' phase	118
4.1.3 The S phase	121
4.2 KINETICS OF PRECIPITATION	123
4.2.1 Introduction	123
4.2.2 Theory of DSC operation	124
4.2.2.1 Cell calibration constant	126
4.2.2.2 Heat effects of reactions	129

	<u>Page</u>
4.2.3 Peak identification	136
4.2.4 Evaluation of heat effects and reaction rates from DSC data	144
4.2.5 Kinetic analysis	151
4.2.5.1 Determination of activation energy	152
4.2.5.1.1 The integral technique	152
4.2.5.1.2 A new differential technique	153
4.2.5.2 Determination of the function f(Y)	154
4.2.5.3 The GPB zone precipitation peak	159
4.2.5.4 The first dissolution peak	173
4.2.5.5 The S' precipitation peak	188
4.2.5.6 The S' dissolution peak	198
 CHAPTER V EFFECTS OF Si ADDITIONS ON THE Al-1.50%Cu-0.75%Mg ALLOY	 207
5.1 THE INSOLUBLE PHASE IN Si CONTAINING ALLOYS	207
5.1.1 Effect of the insolubles on the grain size of the alloys	212
5.1.2 Morphology and distribution of insolubles	214
5.1.3 Volume fractions of the insoluble particles	216
5.1.4 Energy dispersive analysis of the insoluble particles	216
5.1.4.1 Analysis of the extracted particles ...	219
5.1.4.2 Analysis of the particles in the bulk specimens	221
5.1.5 Crystal structure of the insolubles	229
5.1.6 Effect of ageing at 190°C	233
5.2 EFFECTS OF INSOLUBLE PARTICLES ON THE SOLUTE CONTENT OF THE MATRIX	234
5.3 PRECIPITATION BEHAVIOUR IN THE INSOLUBLE FREE Al-1.52%Cu-0.74%Mg-0.23%Si ALLOY	241
5.4 EFFECTS OF AGEING ON THE INSOLUBLE CONTAINING 0.49, 0.76 AND 1.03% Si ALLOYS of Al-1.50%Cu-0.75%Mg	243
5.4.1 Kinetic investigations	246
5.4.2 Microstructural studies	250
5.4.2.1 The Al-1.51%Cu-0.75%Mg-0.49%Si alloy ..	250
5.4.2.2 The Al-1.52%Cu-0.77%Mg-1.03%Si alloy ..	261
 CHAPTER VI SUMMARY AND CONCLUSIONS	 268
6.1 THE Al-1.53%Cu-0.79%Mg ALLOY	268
6.2 EFFECT OF SILICON ADDITIONS	271
6.3 SUGGESTIONS FOR FUTURE WORK	273
 REFERENCES	 274

CHAPTER I

INTRODUCTION

The resistance to plastic deformation of metals and alloys is generally improved by three methods; namely, cold working, solid solution strengthening and introducing particles of a second phase. Many modern high strength alloys are based on the use of one or more of these methods of strengthening. The first two of these techniques have been known since ancient times, but the latter did not become known until the early 19th century. Wilm,⁽¹⁾ while searching for an aluminum alloy which could be strengthened by quenching from elevated temperature, in a manner similar to that used for steel, discovered that hardness of an Al-Cu-Mg-Mn alloy increased when it was quenched from elevated temperatures. The extent of hardening depended upon time and temperature of ageing. These observations were different from those made on steels and gave birth to the phenomenon of "age hardening". The fundamental reasons for age-hardening of aluminum alloy remained unknown to Wilm.⁽¹⁾ However, Mercia, Waltenberg and Scott⁽²⁾ suggested later that hardening observed in aluminum alloys resulted due to their resistance to deformation by slip caused by "submicroscopic dispersion" of the second phase particles formed throughout the grains as a result of ageing for a sufficient period of time at a particular temperature.

Since that time many more alloy systems have been developed which can be hardened by the precipitation of second phase particles. However, progress in the understanding of the microstructural changes during ageing remained a mystery until sophisticated techniques like

x-ray diffraction and electron microscopy were developed. Use of these techniques has resulted in a significantly improved understanding of the process of precipitation hardening. Nevertheless it cannot be regarded as being a completely understood phenomenon until two goals suggested by Kelly and Nicholson⁽³⁾ are met. Firstly, the number and arrangement of precipitates that are formed after a given alloy is aged at a given temperature for a given period of time must be predictable by its phase diagram and the properties of the individual elements. Secondly, yield stress and work hardening properties of the alloy must be capable of being predicted. This is not yet possible even for less complex alloys despite the availability of theoretical models and a wealth of experimental data.

Understanding and predicting the effects of minor or trace elements on the precipitation process in alloys have been another goal that has been pursued during the last 30 years. Although trace element effects are being widely studied, only limited progress has been made in establishing the rules governing their behaviour. In some cases the trace element effect appears unique to a particular alloy system, whereas in others the same trace elements may simulate precipitate nucleation in several systems. The effect of trace elements on aluminum alloys has been reviewed by Hardy and co-workers.⁽⁴⁾

The Al-Cu-Mg alloys are capable of age hardening and retaining their age hardened strength at relatively high temperatures.⁽⁵⁾ Some of these alloys are widely used for various industrial applications.⁽⁶⁾ It has been shown that for alloys having a Cu/Mg ratio close to 2, ageing causes an increase in strength of as much as 275% due to precipitation of the S' phase.⁽⁷⁾ Small additions of Si increase

the strength of these alloys by about 350%.⁽⁷⁾ Silicon containing alloys like AA 2038 are being considered as possible alternative sheet materials for automotive applications.⁽⁸⁾ Because of the high potential of the Al-Cu-Mg alloys, the precipitation behaviour in these alloys was selected for investigation in this study. The silicon free and silicon containing (0.25, 0.50, 0.75 and 1.03%) Al-1.5%Cu-0.75%Mg alloys have been examined by transmission electron microscopy (TEM), differential scanning calorimetry (DSC) and scanning electron microscopy (SEM) in order to characterize the crystallography, precipitation kinetics and effects of small additions of silicon. It is hoped that a little understanding of the phenomena occurring during age hardening of these alloys will result in the development of alloys having improved and predictable properties.

CHAPTER II

LITERATURE REVIEW

The theory of solid state precipitation reactions has been discussed by Christian⁽⁹⁾ and Martin and Doherty⁽¹⁰⁾ and critically reviewed by Russell.⁽¹¹⁾ The literature dealing with precipitation in aluminum alloys has also been reviewed by Hardy and Heal⁽¹²⁾ in 1954, Kelly and Nicholson⁽³⁾ in 1963, Mondolfo⁽¹³⁾ in 1976, Lorimer⁽¹⁴⁾ in 1978 and Shchegoleva⁽¹⁵⁾ in 1982. In the review presented here an outline of the theory of solid state precipitation reactions and the precipitation behaviour in binary Al-Cu and Al-Mg alloys and ternary Al-Cu-Mg alloys will be presented. The literature on the effects of the small additions of solute to ternary Al-Cu-Mg alloys will also be included. Emphasis will be given on the recent developments in our understanding of precipitation processes in the above mentioned alloys.

2.1 THEORY OF PRECIPITATION IN SOLIDS

Precipitation in the solid state in alloys occurs by thermally activated atomic movements. It can be expressed as:



where α' is a metastable supersaturated solid solution, β is a stable or metastable precipitate and α is a more stable solid solution with the same crystal structure as α' , but with a composition closer to the equilibrium composition of α_e (Fig. 2.1). The decomposition of a phase into one or more phases may be divided into three stages:

- (i) creation of nuclei of the new phase by concentration and structural

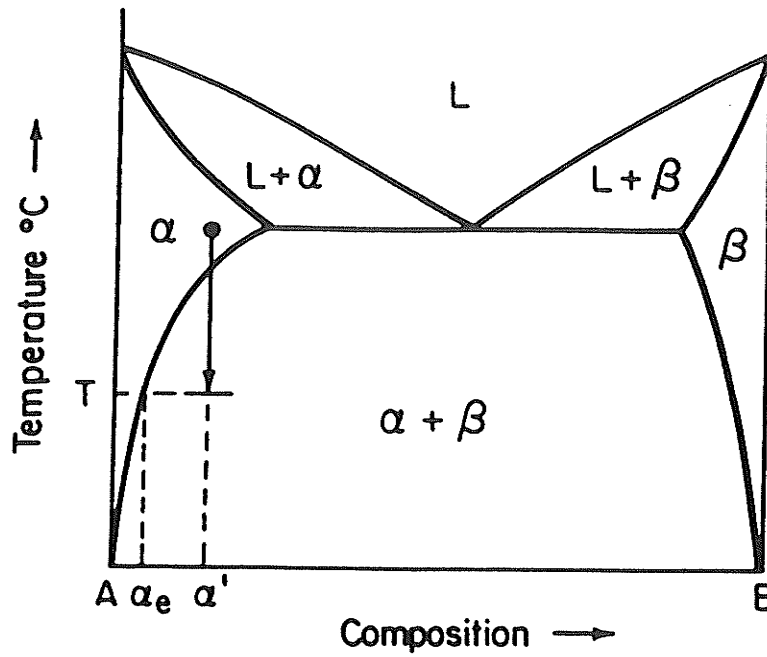


Fig. 2.1 Schematic equilibrium diagram representing precipitation of β from supersaturated α' at temperature T .

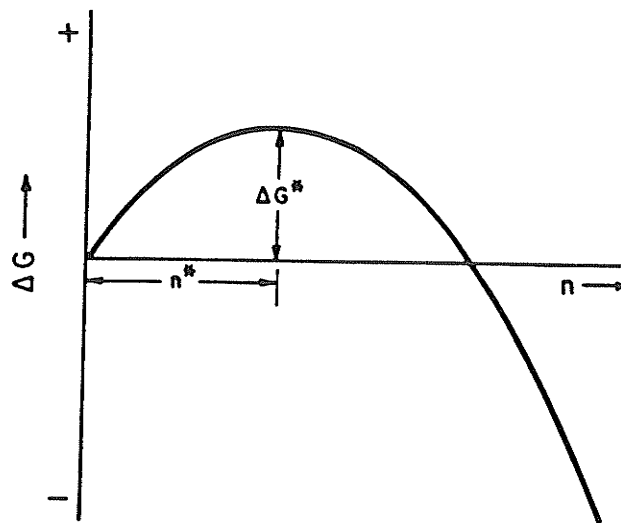


Fig. 2.2 Free energy (ΔG) of a precipitate as a function of the number of atoms it contains (n)⁽¹⁰⁾

fluctuations, (ii) growth of the nuclei directly from supersaturated medium and (iii) growth of larger particles at the expense of smaller ones when the particles have reached appreciable size and the degree of supersaturation in the matrix has become negligible. The first two stages of precipitation are called nucleation and growth respectively. The third stage is called coarsening.

2.1.1 Nucleation of Precipitates

Nucleation is the formation of a microscopic volume of the product phase β in the parent α' phase. Creation of the nucleus is associated with the formation of a surface between β and α' . Hence the total free energy change associated with the nucleation process is given by:

$$\Delta G = a \sigma n^{2/3} + (\Delta g_c + g_e) n V \quad (2.2)$$

where, ΔG - free energy change

a - shape factor

σ - surface energy of β/α' interface per unit area

n - number of atoms

g_e - elastic strain energy (per unit volume of β) associated with nucleus

Δg_c - chemical free energy/unit volume of β

V - atomic volume of nucleus

The variation in ΔG with n is shown in Fig. 2.2. The condition for continued growth of the embryo is that the number of atoms it contains should exceed n^* , i.e. $(\frac{d\Delta G}{dn})_{n=n^*} = 0$. Hence,

$$n^* = \left[\frac{2 a \sigma}{-3V (\Delta g_c + g_e)} \right]^3 \quad (2.3)$$

and

$$\Delta G^* = 1/3 \sigma n^{*2/3} \quad (2.4)$$

For a spherical nucleus of radius r , the surface area is given by $4\pi r^2 = an^{2/3}$ and $n = \frac{4\pi r^3}{3V}$, Hence

$$r^* = \frac{2\sigma}{-(\Delta g_c + g_e)} \quad (2.5)$$

and
$$\Delta G^* = \frac{16 \pi \sigma^3}{3 (\Delta g_c + g_e)^2} \quad (2.6)$$

The chemical free energy term is negative below the equilibrium temperature and increases almost linearly with undercooling. The rate of nucleation \dot{N}_V is given by,

$$\dot{N}_V = \omega C_0 \exp \left\{ -\frac{\Delta G^*}{kT} \right\} \exp \left\{ -\frac{\Delta G_m^*}{kT} \right\} \quad (2.7)$$

where, ω = factor that includes vibration frequency and area of nucleus

C_0 = number of atoms per unit volume in the nuclei

k = Boltzman's constant

ΔG_m^* = activation energy for migration of atoms

The values of ω and ΔH_m^* are assumed to be independent of temperature, but ΔG^* is strongly dependent upon temperature. (16)

$$r^* \propto \frac{1}{\Delta T} \quad \text{and} \quad \Delta G^* \propto \frac{1}{(\Delta T)^2} \quad (2.8)$$

Fig. 2.3(a) shows the variation of the two exponential terms in Equation 2.7, T_e in the Figure is the equilibrium solvus temperature above which α' is single phase. The term $\exp \{ \Delta G^* / kT \}$ is the potential concentration of nuclei which is essentially zero until a critical undercooling, ΔT_c , is reached, below which the term rises very rapidly. On the other hand, the term, $\exp \left(\frac{\Delta G_m^*}{kT} \right)$ is essentially the atomic mobility factor and decreases rapidly with decreasing temperature. The combination of these terms, i.e. the homogeneous nucleation rate is shown in Fig. 2.3(b). Maximum nucleation rate is obtained after a finite undercooling. During precipitation the nucleation rate is initially low, then generally rises and finally decreases as the mean concentration of solute atoms in the matrix decreases.

The chemical free energy change Δg_c in Equation 2.6 is given by $(\Delta G_n / V)$, where ΔG_n is the change in free energy for a mole of precipitate and V is molar volume. ΔG_n is given as

$$\Delta G_n = (G_\beta - G_0) - (X_\beta - X_0) \left(\frac{\partial G}{\partial X} \right)_{X_0} \quad (2.9)$$

The value of ΔG_n can be obtained from the free energy versus composition diagram as shown in Fig. 2.4. If the composition of α is greater than the spinodal composition $\left(\frac{\partial^2 G}{\partial X^2} = 0 \right)$, spinodal decomposition may first take place. For example, if the composition of α is X'_0 , α of composition X_β may form by spinodal decomposition before the formation of the β phase.

The shape of the nucleus is governed by its surface energy and strain energy. The free energy of the nucleus is minimal with respect to its shape. When the atomic size difference is small

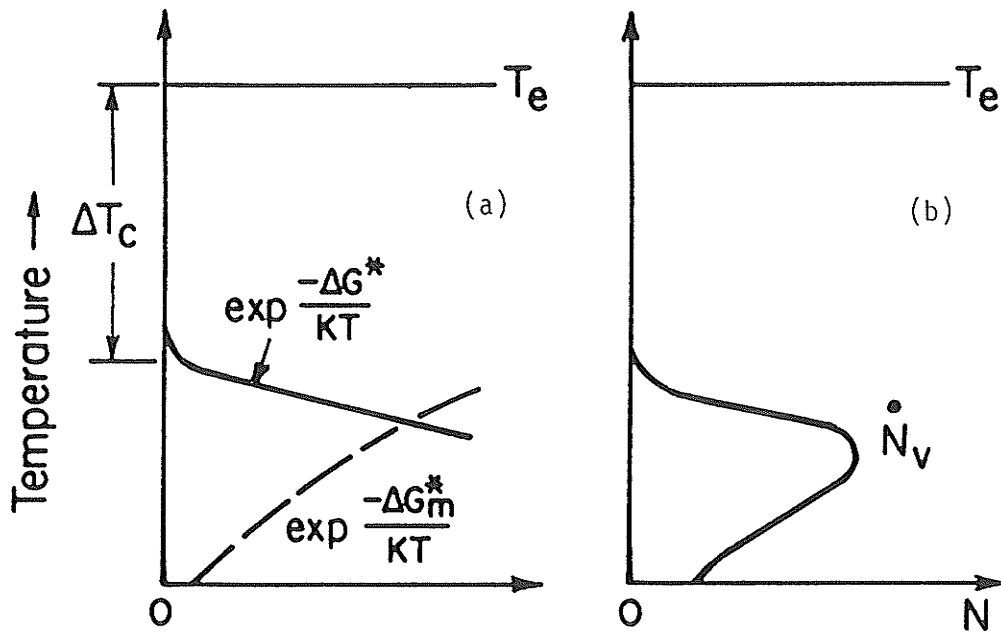


Fig. 2.3 Variation of the rate of homogeneous nucleation with undercooling⁽¹⁶⁾

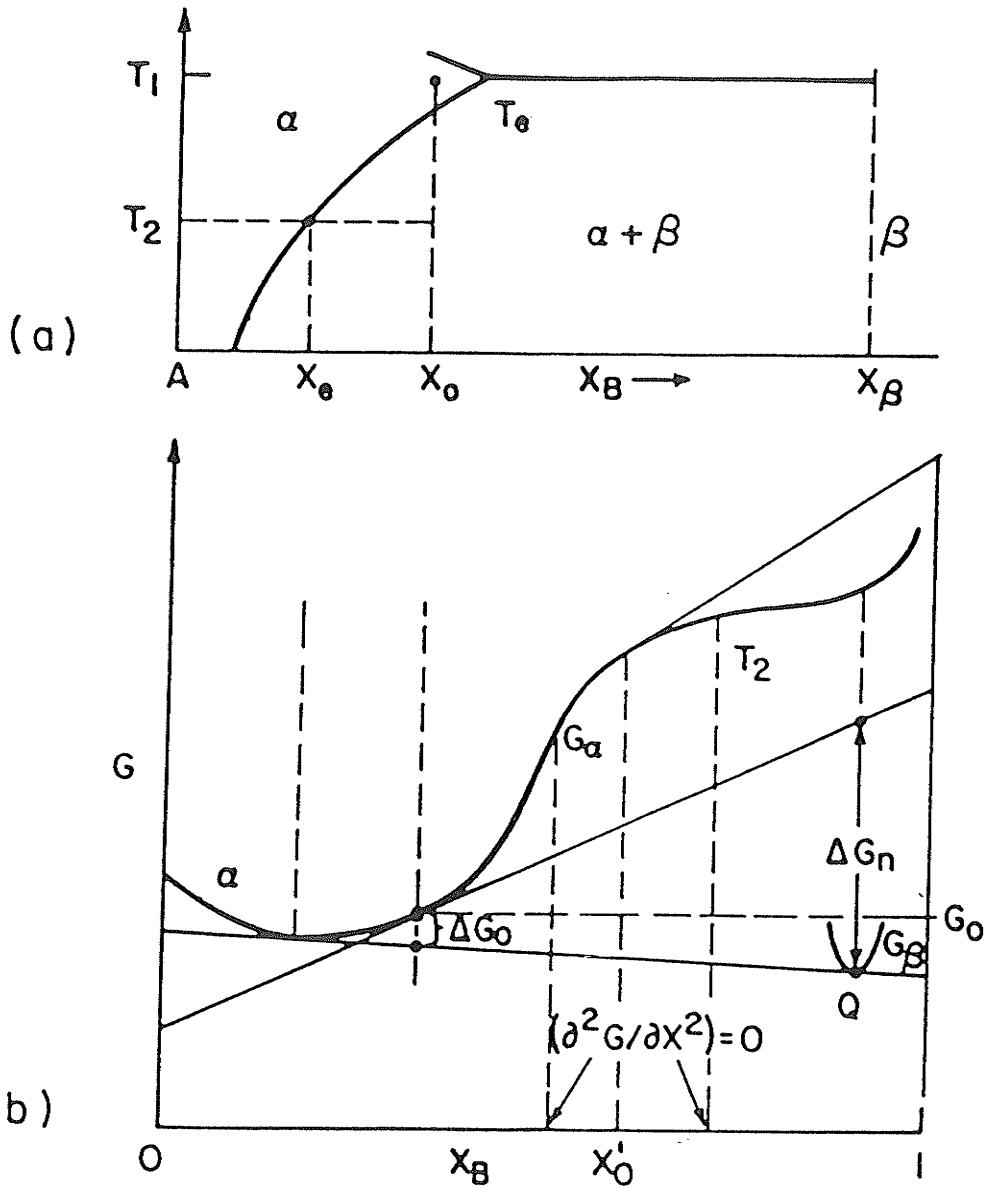


Fig. 2.4(a) Schematic phase diagram showing precipitation at T_2 from supersaturated alloy of composition X_0

(b) Variation of the free energies of phases with composition at temperature T_2 and determination of the molar free energy change due to precipitation, ΔG_n

($\leq 3\%$) spherical GP zones are formed. But at higher misfits ($> 5\%$) plate shaped zones are formed. The largest strain due to lattice misfit is usually along the matrix direction of lowest elastic modulus. For example, in the face centred cubic lattice of aluminum $\langle 100 \rangle$ directions are the ones of minimum modulus, and the GP zones form as discs perpendicular to these directions. The strain energy of the nucleus increases faster than the interfacial energy term until the point is reached where the free energy of the system is lowered by the loss of coherency. GP zones in Al-Zn and Al-Ag alloys are exceptions to this type of behaviour. In these systems, the atomic mismatch between solute and solvent atoms is less than two percent and the strain energy is less than the surface energy. GP zones in such systems form in spherical clusters in order to minimize surface energy.

2.1.2 Growth of Precipitates

Martin and Doherty⁽¹⁰⁾ have reviewed the growth of precipitates in detail. The likely limiting factors for the growth of precipitates in solid solutions are the rates at which the atoms are brought to or removed from the interface by diffusion and the rates at which they cross the interface. The interface reaction is likely to be a slower step during early stages of growth, since diffusion distance tends to be zero in this situation. At later stages, however, diffusion is likely to be the rate controlling step since the continuous removal of solute from the solution reduces the concentration gradient, which is the driving force for diffusion.

For the growth of spherical precipitates of radius R ⁽⁹⁾,

$$R = \alpha (D t)^{\frac{1}{2}} \quad (2.10)$$

where, D is the volume diffusion coefficient and α is a function of super saturation. A similar expression has been deduced for planar precipitates,

$$S = \alpha (D t)^{\frac{1}{2}} \quad (2.11)$$

where S is the half thickness of planar precipitates.

Nuclei are usually bounded by a combination of coherent, semi-coherent and smoothly curved incoherent interfaces. Generally the incoherent interfaces are highly mobile. The precipitates grow by the movement of these interfaces. The shape that develops during growth depends on the relative rates of migration of the interfaces.

2.1.3 Transformation Kinetics

The overall transformation can be represented by plotting temperature for a given fraction transformed (Y) as a function of time. This is called a TTT diagram (Fig. 2.5). For precipitation reactions $\alpha' \rightarrow \alpha + \beta$, Y at a given temperature is defined as the volume of β at a time t divided by the final volume of β . The value of Y varies from 0 to 1.

Among the factors that determine $Y(t, T)$ are the nucleation rate and the growth rate. If the quenched metastable α is allowed to transform at a constant temperature, nuclei will form in the alloy. One possible sequence of events shown in Fig. 2.6(a) is that nuclei form throughout the transformation process so that at any given time a wide range of sizes of particles exist. Another possibility is that all nuclei form at the beginning of the transformation as shown in Fig. 2.6(b). If all potential nucleation sites are consumed in the process, "site saturation" is said to occur. In Fig. 2.6(a) Y

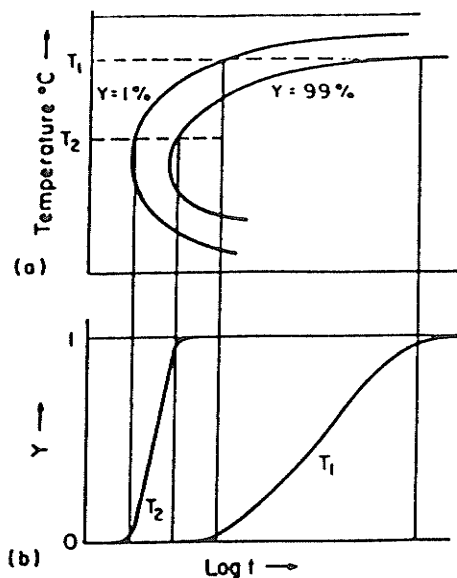


Fig 2.5(a) The time-temperature transformation diagram
 (b) Transformed fraction (Y) vs. time plots at two different temperatures⁽¹⁶⁾

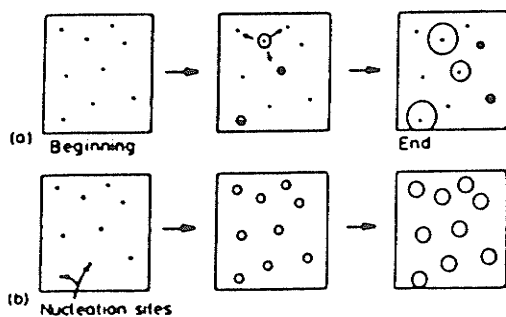


Fig. 2.6(a) Nucleation at constant rate during the whole transformation
 (b) All nuclei appear at the beginning of transformation⁽¹⁶⁾

depends upon the nucleation rate and the growth rate, while in Fig. 2.6(b), Y depends only on the number of nucleation sites and the growth rate. In both cases the overall fraction transformed can be represented by the following:⁽⁹⁾

$$Y = 1 - \exp(-Kt^n) \quad (2.12)$$

This is known as the Johnson-Mehl-Avrami equation, where n is a numerical exponent whose value may vary from ≈ 1 to 4. If there is no change in the nucleation mechanism, n is independent of the transformation temperature. The constant K on the other hand depends on the nucleation and growth rates and is therefore very sensitive to the transformation temperature. It can be shown that the rate constant is $K^{1/n}$ and

$$K^{1/n} = K_0 \exp \{ - Q^*/RT \} \quad (2.13)$$

where, Q^* is the activation energy. It is the value of Q^* which determines the rate of transformation at a given temperature.

2.1.4 Factors Influencing the Activation Energy of Transformation

2.1.4.1 Interfacial Energy

Assuming constant homogeneous nucleation rate and constant growth rate, it can be shown that $n = 4$ and

$$K^{1/n} = K' \exp \left(- \frac{\Delta G_m^* + 0.25 \Delta G_H^*}{kT} \right) \quad (2.14a)$$

Hence,

$$Q^* \approx \Delta G_m^* + 0.25 \Delta G_H^* \quad (2.14b)$$

and from Equation (2.6), $\Delta G^* \propto \frac{\sigma^3}{(\Delta g_c + g_e)^2}$ (2.14c)

It is evident from these equations that the interfacial energy is one of the barriers to nucleation. This barrier can be minimized if the interfacial energy is small. Thus, metastable precipitates capable of forming coherent interfaces can have lower values of Q^* and precipitate in preference to the stable precipitates. The GP zones are often the first precipitates to form because of their low surface energy, typically $10\text{-}30 \text{ mJ/m}^2$ as compared with 500 mJ/m^2 for larger intermediate precipitates.⁽⁹⁾ The volume free energy change for GP zone formation is also small as shown in Fig. 2.7. It may be noted that the free energy change accompanying the transformation of an alloy of composition α_0 into GP zones of composition α_{GP} and matrix of composition α_1 is $(G_1 - G_0)$. Similarly the transformation to θ' is driven by the volume free energy change $(G_3 - G_0)$. Although at equilibrium, θ phase has the largest thermodynamic driving force Δg_c , it also has the greatest interfacial energy due to the incoherent nature of the interface. GP zones have a very low value of surface energy and hence they precede the formation of the equilibrium and intermediate precipitates, provided the alloy is quenched below the appropriate metastable GP zone solvus. At high ageing temperatures, the equilibrium phase may form because it is the only phase with a negative Δg_c term at that temperature.

2.1.4.2 Strain Energy

Coherent precipitates are associated with elastic strains. Equation (2.14b) and (c) show that elastic strain energy increases the activation barrier to transformation as the positive value of g_e reduces the magnitude of the negative Δg_c . The transition of the

coherent state to the incoherent state takes place when the magnitude of the strain energy increases with the growth of the coherent phase. At some stage it becomes energetically more favourable for the interfacial misfit to be accommodated by dislocations lying on the interface. This phenomenon is called loss of coherency. There are several mechanisms in which coherency may be lost and some of these are illustrated in Fig. 2.8 and are described in detail by Martin and Doherty⁽¹⁰⁾ and Porter and Easterling.⁽¹⁶⁾

2.1.4.3 Heterogeneous Nucleation Sites

From the expression for ΔG^* (Equations (2.6) and (2.8)), it can be seen that if nucleation is to be made easier at lower degree of undercooling, the chemical free energy term must be increased in magnitude. In supersaturated solid solutions various non-equilibrium defects such as vacancies and interstitials, dislocations, stacking faults, twin boundaries, grain boundaries, etc. which are present in the system, are expected to increase the free energy of the system. Creation of a nucleus on any of these sites results in the destruction of defects which causes the free energy of the system to decrease. This in turn reduces the activation energy required for nucleation to occur in the system. Details of the nucleation process in heterogeneous sites have been described by Christian,⁽⁹⁾ Martin and Doherty⁽¹⁰⁾ and Porter and Easterling.⁽¹⁶⁾

2.1.4.4 Quenched-in Vacancies

As shown in Fig. 2.9⁽¹⁷⁾ the equilibrium concentration of vacancies increases exponentially with temperature. The equilibrium

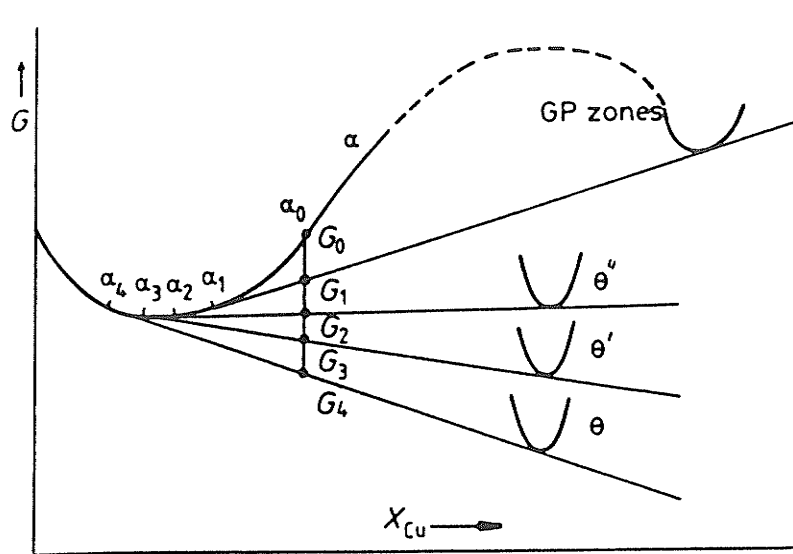


Fig. 2.7 A schematic molar free energy diagram for the Al-Cu system

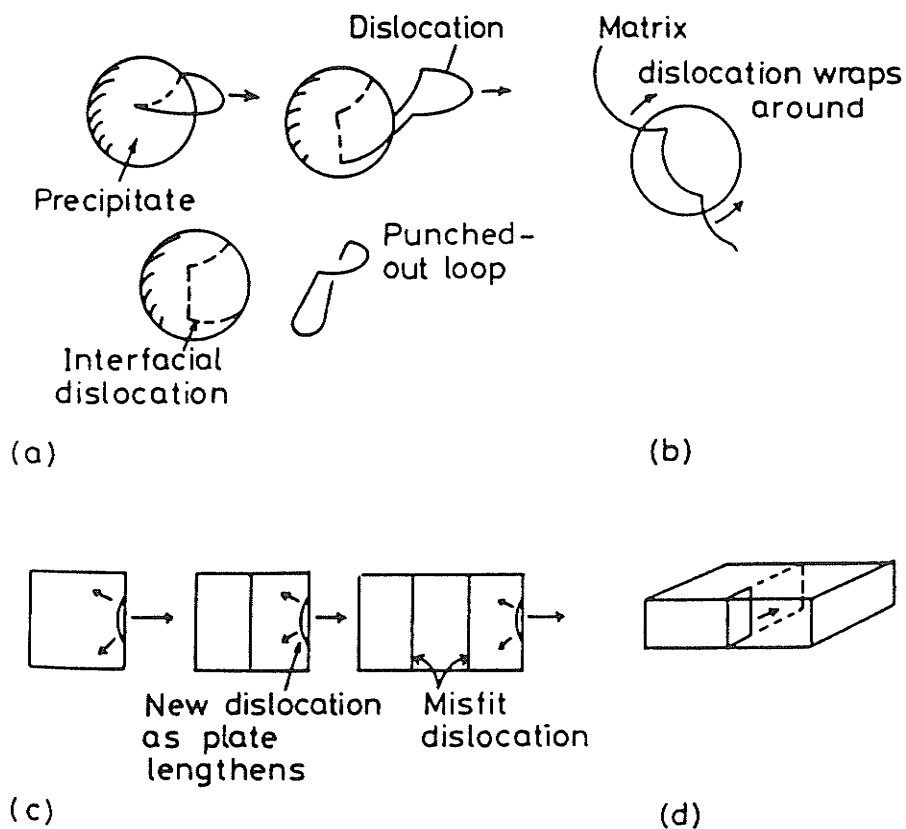


Fig. 2.8 Mechanism of coherency loss

- (a) Dislocation punching from interface
- (b) Capture of matrix dislocation
- (c) Nucleation at edge of plate as plate lengthens
- (d) Loop expansion by vacancy condensation in the precipitate

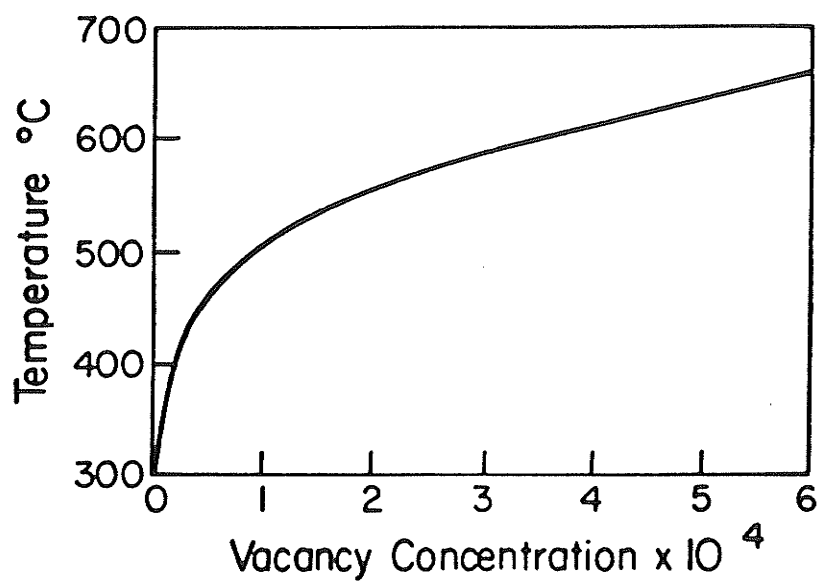


Fig. 2.9 Variation of the equilibrium concentration of vacancies in aluminum with temperature⁽¹⁷⁾

concentration of vacancies is relatively high at the solution temperature and much lower at the ageing temperature. When the alloy is rapidly quenched from the solution treatment temperature to lower temperatures, the high concentration of vacancies present at the solution treatment temperature is quenched-in. The excess vacancies influence the precipitation reaction by providing sites for heterogeneous nucleation and by enhancing diffusion rates at the ageing temperatures.

The quenched-in vacancies in the alloy have a tendency to form small vacancy clusters, dislocation loops and helical dislocations. In dilute Al-Ge and Al-Si alloys, vacancy loops are formed during quenching and the precipitates sequentially form heterogeneously on these dislocation loops.^(3,18,19) Katz and Ryum⁽²⁰⁾ reviewed the precipitation processes in various Al-alloys and found that on quenching dilute Al-alloys the vacancy clusters form, which on up quenching serve as nuclei for the precipitation process. On the other hand, on up quenching concentrated alloys GP zones may form and serve as nuclei for the transition phases. On the basis of studies by Askedale (as quoted by Katz and Ryum)⁽²⁰⁾ on Al-Mg alloys and by Westengen and Ryum⁽²¹⁾ on Al-Mg-Si alloys, Katz and Ryum proposed that vacancy clusters nucleated during quenching, or immediately following quenching, act as sites for nucleation of intermediate precipitates in all alloys in which GP zones do not form due to instability or low solute supersaturation.

Dislocation loops are formed by the collapse of vacancies and they appear on {111} planes. Some loops also lie on {100} and {110} planes as predicted by Kuhlman-Wilsdorf.⁽²²⁾ The loops can

grow by absorbing excess vacancies at the ageing temperature and provide sites for heterogeneous nucleation. The S' precipitates in Al-Cu-Mg alloys⁽²³⁾ and β' in Al-Mg alloys⁽²⁴⁾ are examples of this type of nucleation.

The screw dislocations already present in alloys can absorb excess vacancies by progressive climb to form helical dislocations and provide sites for heterogeneous nucleation.⁽²⁵⁾ The θ' phase in Al-Cu alloys, γ' phase in Al-Ag alloys, and S' phase in Al-Cu-Mg alloys are all found to form on helical dislocations. The addition of solute to aluminum may reduce the effective vacancy supersaturation in the quenched specimen below the level that is necessary for the prismatic loops to be nucleated. The excess vacancies can then only migrate to dislocations to form helices.⁽²⁶⁾

The diffusion rates at the ageing temperatures are greatly enhanced due to quenched-in vacancies and clustering of solute atoms takes place seven or eight orders of magnitude faster than that expected from extrapolation of high temperature diffusion data. In dilute alloys the binding energy between solutes and vacancies may be appreciable. For example, Panseri et al.⁽²⁷⁾ and Christian⁽⁹⁾ report that a solute vacancy cluster may move at an appreciable rate gradually acquiring more solute atoms and vacancies. In this way the quenched-in vacancies may assist diffusion in alloys.

The literature related to increase in diffusion rate due to quenched-in vacancies, has been reviewed by Kelly and Nicholson.⁽³⁾ Due to high diffusivity of the quenched-in vacancies it is very difficult to avoid losing vacancies in the vicinity of grain boundaries and interfaces. This has an important effect on the distribution

of precipitates that form in the vicinity of the grain boundary or interfaces on subsequent ageing. The causes and effects of precipitate free zones (PFZ) at grain boundaries have been reviewed in detail by Starke.⁽²⁸⁾

2.1.5 Formation of Transition Phases and the Precipitation Sequence

Because of changes in the value of Q^* due to various factors discussed in the last section, the rate of precipitation of many metastable phases becomes appreciable compared with that of the stable phase. The intermediate transition phases also help with nucleation of other transition phases. The nucleation of intermediate precipitates at GP zones has been examined in detail by Marth et al.⁽²⁹⁾ Russell⁽³⁰⁾ has shown that change in the free energy associated with the incoherent precipitation is increased by the incorporation of vacancies which relieve the transformation strains. Marth et al. have also shown that the presence of GP zones provides an effective surface for nucleation and makes available a significant amount of GP zone-matrix interfacial energy which reduces the interfacial energy component of the activation energy barrier to nucleation.

Russell and Aaronson⁽³¹⁾ have attempted to summarize the factors affecting the sequential nucleation of precipitates. The early transition phases are predicted to nucleate preferentially at the precipitate matrix interfaces of their predecessors. The reduction in activation energy occurs after initial precipitation of solute atoms. Most of the examples of precipitation sequence cited in the literature were found to be in agreement with this prediction. Baur⁽³²⁾ and Phillips⁽³³⁾ have demonstrated that an in situ transformation from

GP zones to θ'' occurs during isothermal growth. However, some serious objections to the general applicability of sequential nucleation theory have been raised. In the Al-Cu system GP zones form homogeneously, but there is no clear experimental evidence for θ'' being nucleated at GP zones. It has been shown that θ' nucleates on dislocations.⁽¹⁴⁾ Suzuki and Kimura⁽³⁴⁾ demonstrated that θ' is also nucleated on some types of vacancy clusters.

Westengen and Ryum⁽²¹⁾ showed that β'' and β' phases in the Al-Mg-Si system developed continuously from homogeneously nucleated GP zones. However, β phase never nucleated on β' , but rather as plates or cubes on vacancy-solute atom clusters. Lendvai et al.⁽³⁵⁾ also found that vacancy-solute atom clusters are formed in these types of alloys during quenching.

The precipitation reactions in Al-Zn-Mg systems are probably most complex among aluminum alloys. Many investigators⁽³⁶⁻³⁸⁾ have demonstrated that there are two types of GP zones in these alloys. One of these two types is rich in vacancies and probably is best regarded as a vacancy-solute cluster while the other is the GP zone. On up quenching the intermediate η' -phase or the T-phase is nucleated on the vacancy-solute atom clusters, while GP zones are reverted.

On the basis of observation made on different Al-alloy systems, it is evident that precipitation kinetics are quite different from those advocated by Russell and Aaronson.⁽³¹⁾

During or immediately following quenching from the homogenization temperature, two clustering reactions may take place; clustering of solute atoms form GP zones and clustering of vacancies into vacancy clusters. The two clustering reactions are interdependent

through the diffusivity of solute atoms and vacancies. On subsequent ageing the GP zones grow and internal ordering takes place within them. On up quenching the GP zones dissolve either partially or completely, depending upon whether the up quench temperature is below or above the GP zone solvus.

Katz and Ryum⁽²⁰⁾ have proposed a model to generally explain the decomposition of aluminum alloys after quenching and the subsequent nucleation of intermediate precipitates. On quenching from the solution temperature two types of clusters are formed and the subsequent behaviour of these two types depends upon the particular alloy system and alloy composition. In dilute Al-Si and Al-Ge alloys for example, no zones form after quenching to a low temperature (T_q , Fig. 2.10). During ageing, only the vacancy clusters are stable, and they act as a nuclei for Si and Ge precipitates. Al-Cu and Al-Zn-Mg alloys, however, would behave more as X_B^{II} in Fig. 2.10. Precipitation reactions occurring on up quenching depend on the length of time spent at T_q (Fig. 2.10) and whether the ageing temperature is above or below the GP zones solvus. The vacancy clusters grow slowly at low ageing temperatures but are much more stable on up quenching than GP zones and are able to act as nucleation sites for semi-coherent and fully coherent precipitates. Precipitate free zones are formed around vacancy sinks, as a critical vacancy concentration is required for the formation of vacancy clusters. It can be concluded that the vacancy clusters contain both solute atoms and vacancies and some kind of crystallographic character. The critical temperature for nucleation of these defects, which is dependent on the solution temperature, is approximately 20-40°C for Al-Zn-Mg alloys and 0-20°C for Al-Mg-Si

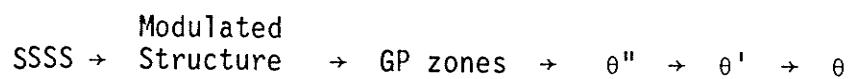
alloys.

This model, then, is a combination of Lorimer and Nicholson's theory and the one first proposed by Ryum.⁽³⁸⁾ It is an attempt to produce a unifying theory, capable of explaining the mechanisms of nucleation of intermediate precipitates in all aluminum alloys.

The TTT diagram of a system which may have many transition phases is shown in Fig. 2.11. This diagram clearly illustrates that, depending upon the ageing temperature, a number of possible sequences of precipitation may be observed. By modifying TTT curves of phases, the precipitation sequence may be altered.

2.2 PRECIPITATION IN THE BINARY Al-Cu ALLOY

The decomposition of a supersaturated solid solution (SSSS) of copper in aluminum depends on the alloy composition, ageing temperature and time. Based on x-ray diffraction, TEM and field ion microscopy (FIM), the following precipitation sequence has been established.⁽³⁹⁾



Each succeeding precipitate in this sequence is in metastable equilibrium with the aluminum-rich matrix below its solvus (Fig. 2.12).

The development of many modern research techniques has led to a much better understanding of the precipitation processes in these alloys. However, there is considerable disagreement about the detailed atomic arrangements of GP zones and the relationship between GP(I) and GP(II) zones, and the GP zones and the intermediate precipitates.

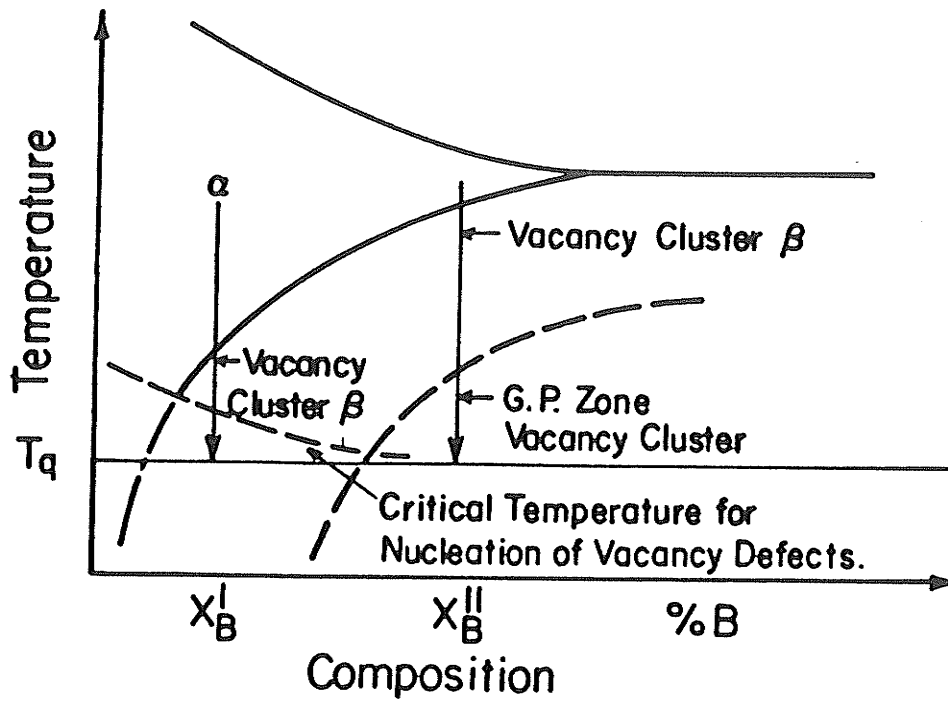


Fig. 2.10 Schematic phase diagram illustrating the different way in which an alloy of composition X_B may decompose, following quenching to T_q and subsequent ageing at a higher temperature⁽²⁰⁾

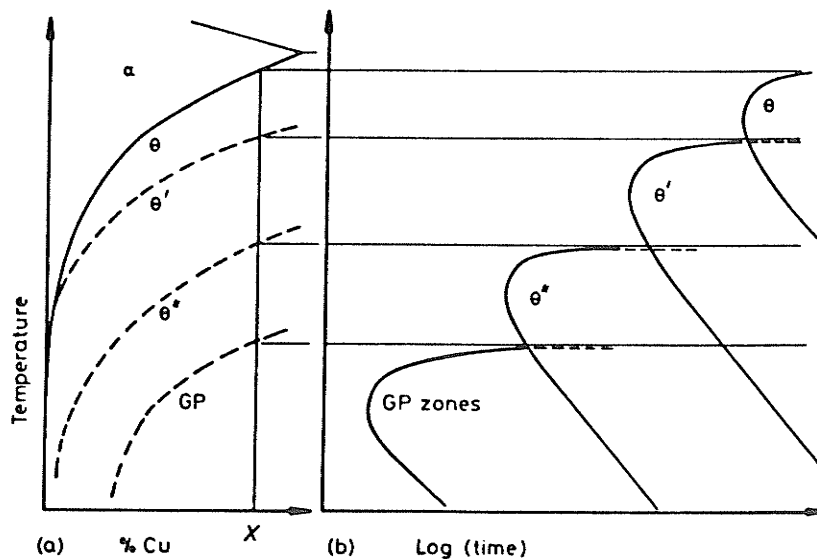


Fig. 2.11(a) Metastable solvus lines in Al-Cu alloys (schematic)
 (b) Time for start of precipitation at different temperatures for alloy X in (a)⁽¹⁶⁾

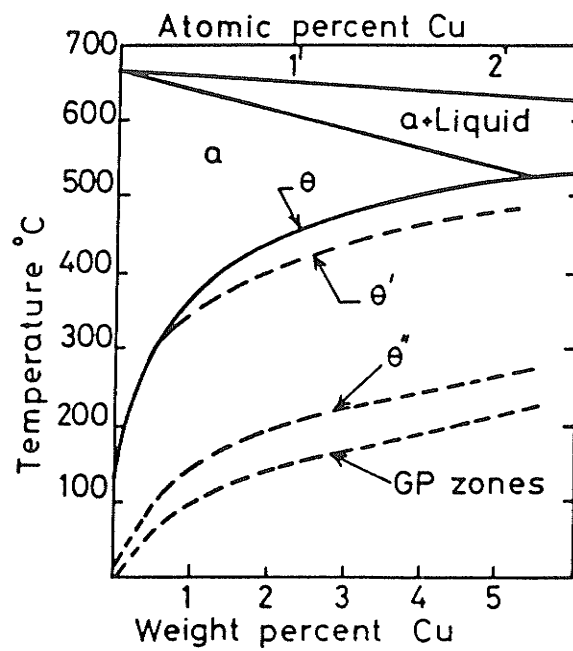


Fig. 2.12 Metastable solvus curves for GP zones, θ'' and θ' precipitation⁽¹⁶⁾

2.2.1 GP(I) Zones

Copper rich clusters in quenched and aged Al-Cu alloys are known as GP zones. Numerous investigations have been carried out on the kinetics of zone formation (see for example Sanderson⁽⁴⁰⁾). Turnbull⁽⁴¹⁾ has made several suggestions regarding zone formation including spinodal decomposition and pipe diffusion through moving dislocations. Lorimer and Nicholson⁽⁴²⁾ favour homogeneous nucleation of GP zones. Naudon and co-workers⁽⁴³⁾ and Rioja and Laughlin⁽⁴⁴⁾ have presented evidence for spinodal decomposition. Rioja and co-worker in a TEM study on a room temperature aged Al-1.7%Cu alloy have reported modulated structures consisting of copper rich and poor regions which resulted in continuous formation of GP zones. However, when an alloy was aged at 130°C the GP zones nucleated directly from the solid solution. Thus, they concluded that the formation of GP zones in Al-1.7%Cu alloy occurs by spinodal mechanism between 20-130°C. This observation has been supported by Matsubara and Cohen⁽⁴⁵⁾ and Desarmot and Quere.⁽⁴⁶⁾

GP zones are detected as streaks in x-ray or electron diffraction patterns parallel to $\langle 100 \rangle$ matrix directions.⁽⁴⁷⁾ The structure of such zones therefore, is characterized by segregation of Cu atoms on (100) matrix planes and the strain fields induced by coherency of zones with the matrix. Several models (illustrated in Fig. 2.13) have been proposed for the structure of zones.⁽⁴⁸⁻⁵²⁾ The generally accepted model is that due to Gerold.⁽⁴⁹⁾ It describes GP zones as single layers of Cu atoms coherent with the (100) matrix planes and forming disc shaped particles. The strain associated with disc shaped particles decreases linearly until it vanishes at the

fifteenth plane from the zone. Nicholson and Nutting⁽⁵⁴⁾ in a TEM study were able to resolve and detect disc shaped zones, 4-6 Å thick and ≈ 90 Å in diameter on $\{100\}_M$ matrix planes of an Al-4%Cu alloy aged for 16 h at 130°C. Later, Phillips^(33,55) used bright field and lattice imaging techniques to study the GP zone structure in an Al-3%Cu alloy aged at 130°C. A direct correspondence between $\{200\}_M$ lattice fringes and atom planes was assumed and measurements were made to determine the strain field surrounding individual zones. These were found to be complex; most exhibited one or two oscillations between the first and the tenth $\{002\}_M$ planes and the exact nature of the displacement varied from zone to zone. The displacement field measurements did not fit either Gerold's or Toman's model of a zone, but were closer to Toman's, while the contrast in the image was interpreted as consistent with the copper monolayer model of Gerold.

Yoshida, Cockayne and Whelan⁽⁵⁶⁾ used the weak beam electron microscopy to investigate plate-like GP zones in aluminum alloy with 1.48 and 3.97%Cu aged at 80°, 100° and 130°C. GP zones were imaged under a variety of diffraction conditions and some common features were noticed under each condition. In dark field images with the value of deviation parameter $|S| \leq 1.1 \times 10^{-2} \text{ \AA}^{-1}$ the zones appeared as pairs of bright lines with a spacing which depended on the value of deviation parameter. The comparison with the computed image agreed well with the observed zones and supported Gerold's model. However, strain around the $\{200\}$ planes was observed to be higher, that is, 0.2 rather than 0.1 for adjacent planes as predicted by Gerold's model.

Field ion microscopy is also being used to study the structure of GP zones.⁽⁵⁷⁻⁵⁹⁾ Abe et al.⁽⁵⁷⁾ have suggested that the GP zones

have complex shapes with inhomogeneity in their thickness which is in close agreement with the structure proposed by Auvray et al.,⁽⁵³⁾ although Mori and co-workers⁽⁵⁸⁾ have reported only single layer of Cu atoms on {100} planes.

Auvray et al.,⁽⁵³⁾ using diffuse x-ray intensity measurements and computer simulations, suggest that the GP zone state is a mixture of single and multilayer regions with (001) faces (Fig. 2.13(e)). The GP zone state is rather complex, unlike previous models. They have suggested that these multilayer zones are due to overlap or initiation of GP(II) zones before ordering. This is appreciably different from the accepted model of GP(I) zone. Matsubura and Cohen⁽⁶⁰⁾ in an investigation on Al-Cu alloys confirmed the presence of single layer and multilayer pure Cu zones on {100} matrix planes. They also found that strain around GP(I) zones oscillates with distance from them and vanishes near the fourth or fifth Al plane. In a recent study⁽⁵⁹⁾ using FIM, Hono and co-workers confirmed results of Matsubura and Cohen on the presence of single and multilayer zones. Phillips⁽⁵⁵⁾ using lattice imaging techniques has also reported the presence of zones two atom layers thick and a zone density of $1.3 \times 10^{14} \text{ cm}^{-3}$ in the quenched material. Several investigators have used high resolution electron microscope to observe GP zones in Al-Cu alloys.⁽⁶¹⁻⁶⁴⁾ Sato et al.⁽⁶¹⁾ in a study using the lattice imaging technique have confirmed the presence of the multiple Cu-rich layer structure and also have shown that these various periodic structures are composed of several Cu-rich layers and Al (200) planes which are different and more complex than GP(I) and GP(II) structures. Sato and Takahashi⁽⁶³⁾, in a further study, found that periodicity of these

complex atypical structures is similar to that of a θ' precipitate. Moreover, these complex structures transform more smoothly to the θ' precipitate as a result of ageing.

Most investigations in the last six years have shown the presence of multilayer complex zones. Their existence has, however, become questionable as they have high strain energy. Several studies^(53,59) suggest that these zones may grow from single layer to multilayer zones. Hono et al.⁽⁵⁹⁾ have related their existence to a pre-precipitation stage in these alloys. It is now increasingly clear that GP zones form by spinodal decomposition. Therefore the zones are expected to be formed through concentration fluctuation and, in early stages of the precipitation, the interface of the precipitates (Cu clusters) must be diffused. It is also suggested that if these clusters continuously grow into GP zones, it is probable that these zones, formed at room temperature, are multilayer on (001) planes. Moreover, the ratio of the number of multilayer to single layer GP zones must depend upon ageing temperature and time.

The stability of GP zones has been studied recently using calorimetry.⁽⁶⁵⁻⁶⁷⁾ Zahra et al.^(65,66) have found that the results of reversion experiments carried out by Beton and Rollason⁽⁶⁸⁾ accurately describe the solubility limits of GP zones in alloys excepting those with Cu contents less than 1%. For these alloys it was found that the results of Beton and Rollason were below the true values. The maximum temperature for stability of GP zones in an Al-4%Cu alloy was found to be 170°C. In another calorimetric investigation, Papazian⁽⁶⁷⁾ found good agreement with the results of Beton and Rollason.

Yoshida⁽⁶⁹⁾ studied the distribution and size of GP zones

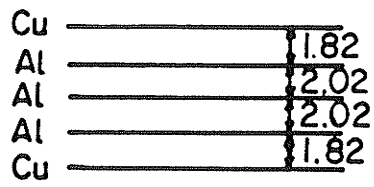
using the weak beam technique and found that GP(I) zones show normal distribution even in the transient stage from GP(I) to GP(II) zones. It was suggested that nucleation and growth of GP zones was due to the random walk of solute atoms, although Cu atoms could be supplied from the compression side near the edge of GP zones.

2.2.2 GP(II) Zones or (θ'') Phase

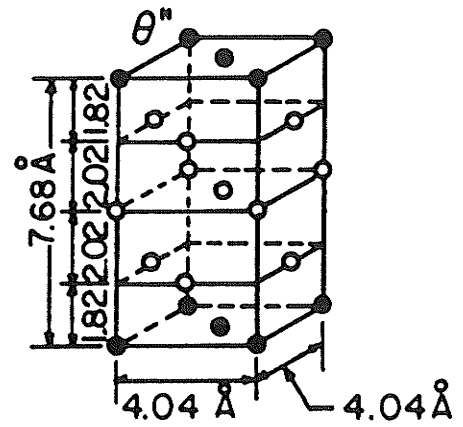
After longer ageing time and at higher temperatures (130°-170°C), the streaks in diffraction patterns transform into well defined intensity maxima. The precipitate at this stage is designated as θ'' .^(48,70) The structure of θ'' proposed by Guinier⁽⁴⁸⁾ does not fit the diffuse intensity maxima measurement along [h00] direction in reciprocal space.⁽⁷¹⁾ Another model proposed by Gerold⁽⁴⁹⁾ suggested two pure Cu {100} layers separated by three Al layers (Fig. 2.14(c)). The interplanar spacings involving Cu planes are 0.182 nm and those involving only Al planes are 0.202 nm. The structure which is usually accepted is tetragonal (Fig. 2.14(b)) with $a = 0.404$ nm and $c = 0.79$ nm. The orientation relationship with the matrix is

$$(001)_{\theta''} \parallel (001)_M ; [001]_{\theta''} \parallel [001]_M$$

The composition of θ'' was deduced to be about 17%Cu by comparing the θ'' lattice parameter with that of splat quenched fcc alloys.⁽⁷²⁾ Silcock and co-workers⁽⁴⁷⁾ and Gerold⁽⁴⁹⁾ showed that the c parameter varies with ageing time and temperature. The model of Gerold for θ'' has been verified by the x-ray measurements of Baur,⁽⁷³⁾ the weak beam study by Yoshida et al.⁽⁵⁶⁾ and the high voltage lattice imaging study of Satoh and Takahashi.⁽⁶³⁾ Satoh and Takahashi



(a)



(b)

Fig. 2.14 (a) Schematic diagram of a model of GP(II) zones⁽⁴⁹⁾
 (b) A θ'' unit cell

suggest θ'' to be a distinct phase structure which is different from single layer GP(I) zones. Recent single crystal x-ray work on the structure of the θ'' showed that the generally accepted structure of θ'' is probably quite correct and that multilayer arrays of (θ'') may account for 20% of zones in alloys aged to produce GP(I) zones.⁽⁷⁴⁾

There is considerable argument about the ambiguous nomenclature, GP(II) vs. θ'' . It arises from the debate, whether θ'' is to be considered a phase distinct from GP zones or whether the zone and θ'' are considered as two stages of development of one phase. There have been two arguments for θ'' to be designated as a distinct phase: (i) θ'' has a distinct ordered crystal structure, and (ii) the existence of two stage ageing processes and the possibility of complete reversion of GP zones before the formation of θ'' . Gaylor and Parkhouse⁽⁷⁵⁾ distinguished θ'' from GP zones metallographically and argued on this basis that θ'' is a distinct phase. Nicholson and co-workers⁽⁷⁶⁾ noted that "... GP(II) was best described as a coherent intermediate precipitate rather than a zone, since it has a definite crystal structure ... and that ... Guinier's symbol for the θ'' phase was preferred". On the other hand, the experimental observations by direct lattice imaging in HVEM, weak beam microscopy, FIM, and DSC suggest continuous change from GP(I) to θ'' . Phillips⁽⁵⁵⁾ used lattice imaging and suggested that "there is a continuous structure progression from monolayer zones, to groups of parallel staggered zones, to GP(II) to θ' platelets". Papazian⁽⁶⁷⁾ in his DSC study on 2219 Al alloy found that transformation of GP(I) zones to θ'' were not abrupt, but rather more evolutionary in nature. He concluded that θ'' is not a required transitional step in the ageing sequence

and is consistent with the concept of θ'' as a regular spaced array of monolayer GP zones that evolve during long term ageing.

Yoshida et al.⁽⁵⁶⁾ have suggested a definite sequence for formation of GP(II) from GP(I) zones. As shown schematically in Fig. 2.15 the extra layer of copper atoms are envisaged to nucleate and grow on either side of the two main layers. This would be a state intermediate between a two layer GP(II) and a multilayer GP(II) zone. Finally, GP(II) zones may become ordered and approach θ'' precipitate structures. In another investigation⁽⁶³⁾ on Al-4%Cu alloy, it was found that GP(I) and GP(II) with typical structures, are formed predominantly as pre-precipitates in the early stage of ageing and that GP(I) zones grow into GP(II) zones. They also found that the GP(II) zone structure agreed well with Gerold's model. The GP(II) zones nucleate at the edge of Cu-rich layer, thicken and transform continuously to the semi-coherent θ' phase losing coherency gradually.

Matsubura and Cohen⁽⁶⁰⁾ found that the GP(II) zones or θ'' are on the average five layers thick, and consist, as in the GP(I) zones, of essentially pure Cu. The structure is tetragonal, not because of ordering, but because of constraint imposed by the matrix. The structure is thus suggested to be identical with GP(I) zones except for the thickness of the precipitate. Moreover, they argued on the basis of the study due to Matsubura, Wu and Cohen⁽⁷⁷⁾ that the extra peaks which supposedly characterize the GP(II) or θ'' state can be detected even at ageing times that are assumed to produce only GP(I). These extra peaks are due to the thickness of the GP(II) zones in the later processes rather than a unique structural difference between GP(I) and GP(II).

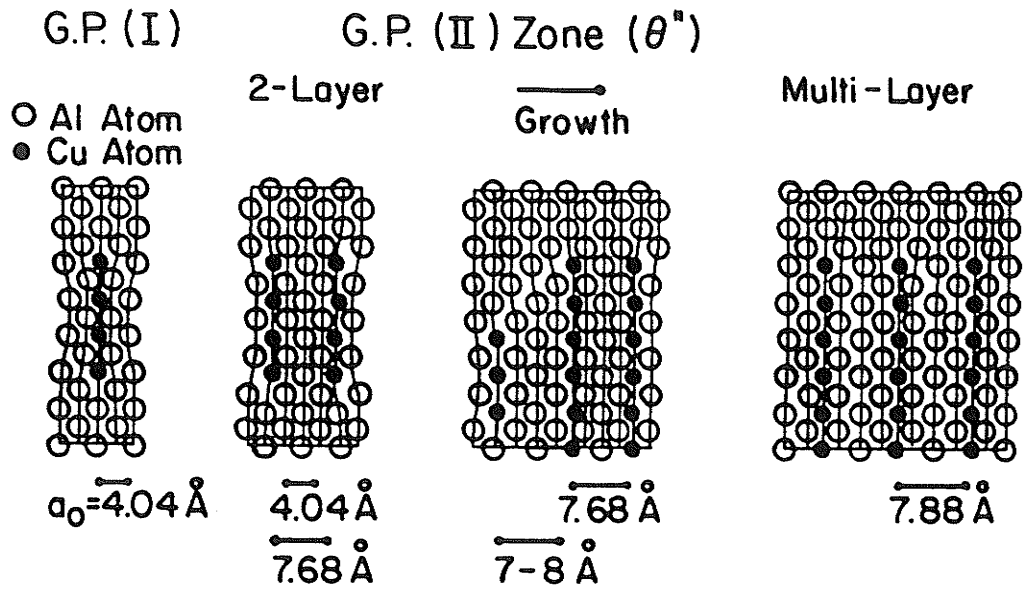


Fig. 2.15 Schematic diagrams of models of GP(I) and GP(II) zones⁽⁵⁶⁾

Hono and co-workers⁽⁵⁹⁾ have recently distinguished multilayer GP(II) or θ'' from single layer GP(I) zones. Schematic views of (001) planes containing multilayer GP(I) zones and GP(II) zones or θ'' are shown in Fig. 2.13(e). Multilayer zones have no spacing among the Cu rich layers, so that the zones are observed to have a thickness of a few atomic layers, while θ'' has a structure suggested by Gerold. Hence "images of multilayer zones might represent θ'' or GP(II) zones". In light of these observations, it appears that GP(II) or θ'' in the later stage of ageing is not very different from GP(I) zones other than in thickness.^(59,60) Results of various studies on the structure of GP(II) or θ'' have been summarized in Table 2.1.

The possibility of complete reversion of GP zones after formation of GP(II) or θ'' has been studied widely by two step ageing techniques. The solvus for GP zones determined by resistivity measurements⁽⁷⁹⁾ is vastly different from that obtained by x-ray and hardness measurements.^(47,68,80) Also the theoretical estimates made by Merjering⁽⁸¹⁾ are quite different from those of Baur.⁽⁷³⁾

The most widely quoted GP zone and θ'' solvi are those determined by the hardness-reversion experiments of Beton and Rollason.⁽⁶⁸⁾ Their results were, however, accurate for a high level of Cu content. Nakamura et al.,^(82,83) in a study on Al-1.7 at %Cu alloy, investigated solvus curves for GP zones and θ'' using the nuclear magnetic resonance (NMR) technique. They found that the precipitation of the GP(I) zone mainly occurs in substage a_1 (Fig. 2.16). At the end of substage a_1 at which the precipitation of the GP(I) zone is much slowed down, the formation of θ'' becomes active. It results in a decrease in the solute concentration of the matrix

Table 2.1 Summary of structural studies for GP(II) zones.

Reference Number	Authors	Type of Measurements	Results
78	Guinier	X-ray	Al: (1/6 Cu + 5/6 Al): Cu: (1/6 Cu + 5/6 Al): Al: 2.10: 1.85: 1.85: 2.10 Å
49	Gerold	X-ray	Two Cu layers separated by three Al layers (Cu: Al: Al: Al: Cu); 1.82: 2.02: 2.02: 1.82 Å
54	Nicholson & Nutting	TEM	Consisting of alternate Cu and Al layers.
55	Phillips	TEM	Two Cu rich layers separated by 6-14 Å.
56	Yoshida et al.	TEM	Gerold's model.
57	Abe et al.	FIM	Two Cu or Cu rich layers separated by matrix layers.
63	Sato & Takahashi	TEM	Two Cu rich layers separated by 3 matrix layers and few multilayer and complex layer structures.
64	Yoshida et al.	TEM	Two Cu rich layers separated by 2 or 3 matrix layers and unexplicable structures.
74	Wu et al.	X-ray	GP(II) state is an ordered array of Cu rich and Al layers.
58	Mori et al.	FIM	Two Cu rich layers separated by 3 Al layers.
60	Matsubura & Cohen	X-ray	GP(II) zone is on average 5 layers thick. Cu rich and multilayer regions are always present. Upon ageing there are fewer thin zones but more thick zones. Designation GP(I) and GP(II) is unnecessary.
63	Hono et al.	FIM	Multilayer zones with no matrix layer spacing might be

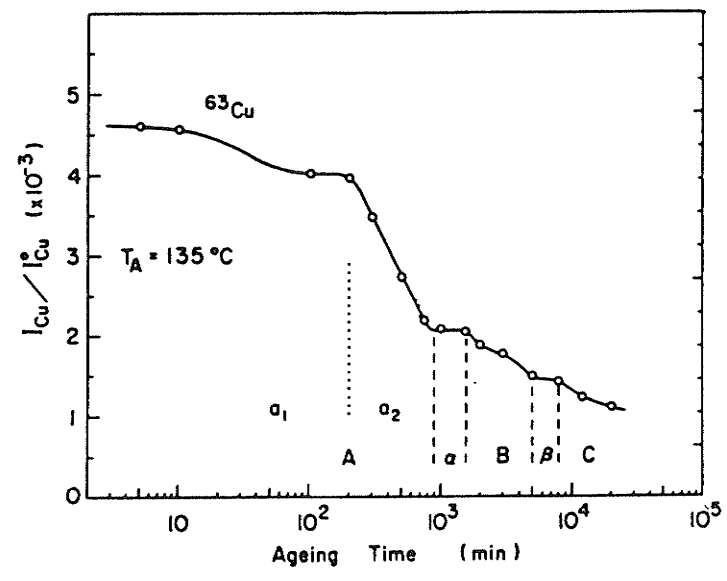


Fig. 2.16 The copper intensity curve for a solution treated Al-1.7at%Cu alloy aged at 135°C(82)

in sub-stage a_2 . However, once solute concentration reaches the solvus of the GP(I) zone, the existing GP(I) zones begin to dissolve. The plateau α comes to an end when all the GP(I) zones are exhausted, and thereafter the solute concentration in the matrix is again decreased with further precipitation of θ'' . Recently, Matsubara and Cohen⁽⁶⁰⁾ have shown that the appearance of the plateau in resistivity (or hardness)^(80,68) curves for times which were thought to be incubation periods for GP(II) zones is in fact related to the coarsening process of GP(I) zones. Different solvus curves presented earlier are merely an expression of the differences in zone thickness for different ageing times as these solvi were determined by reversion experiments.

In spite of the availability of results of detailed studies carried out by TEM, x-ray scattering, FIM, hardness measurements, NMR and DSC on the structure and properties of zone development, it is not possible to unambiguously establish whether θ'' is a distinct phase from GP(I) zones or whether the GP(I) zone and θ'' are to be considered as two stages of development of one phase. As pointed out by Lorimer,⁽¹⁴⁾ there is general agreement that the θ'' forms from the preceding GP(I) zones. Evidence for this comes from several sources. Eto and co-workers⁽⁸⁴⁾ have found that tensile stress applied in the [001] direction of an Al-Cu single crystal favours formation of GP(II) zones preferentially on [100] and (010) variants. On subsequent ageing without stress some variants are preferentially found for the transformation of θ'' , indicating a definite relationship between the two phases.

2.2.3 The θ' Phase

The x-ray diffraction studies have shown that the θ' has a body centred tetragonal CaF_2 type lattice structure with parameters, $a = 0.404 \text{ nm}$, and $c = 0.58 \text{ nm}$.^(47,49,78) It has the same composition as equilibrium compound θ (CuAl_2). This structure is considered as a modification of the LI_0 super lattice in which two of the copper atom positions are vacant. The orientation relationship with the matrix is:

$$(001)_{\theta'} \parallel (001)_M ; [110]_{\theta'} \parallel [110]_M .$$

Fig. 2.17 shows the arrangement of aluminum and copper atoms in the CuAl_2 lattice. The size of the θ' phase precipitates depends upon the time and temperature of ageing and ranges from 10 to 600 nm or more in length with a thickness of about 10-15 nm.⁽³⁾

There are two points of view concerning nucleation of the θ' phase. Many experimental observations indicate that the θ' phase forms from GP(II) zones and is a continuous process.⁽⁸⁵⁻⁸⁷⁾ On the other hand, many other investigators⁽⁸⁸⁻⁸⁹⁾ have reported that θ' nucleates independently on certain preferential sites like dislocations, subgrain boundaries, regions near active slip planes and vacancy clusters. Lorimer,⁽¹⁴⁾ in a recent review, ignored the former point of view and advocated that θ' preferentially nucleates on dislocations and is able to relieve misfit around the periphery of the plates. This is in support of the observations of Headly and Hren⁽⁹⁰⁾ and theoretical predictions of Russell and Aaronson.⁽³¹⁾ Lorimer has also proposed that subsequent nucleation and growth may occur in an autocatalytic fashion (Ref. 11, p. 269). This theory holds that the

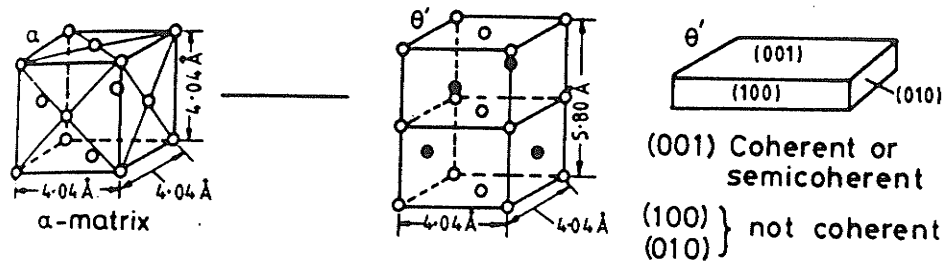


Fig. 2.17 Crystal structure and shape of the θ' precipitates

stress field around a particular θ' plate may aid in the nucleation of the other plates at a region nearby.

Many recent investigations suggest that θ' evolves out of the θ'' phase as a result of ageing. The stress ageing experiments of Eto et al.⁽⁸⁴⁾ have shown that prolonged two step ageing treatments yield the same variants of the θ'' and θ' as were initially present in the GP (Cu) zones strengthened microstructure. This observation was further confirmed by the x-ray diffraction and high resolution microscopic study of Takahashi and Sato.⁽⁹¹⁾ Their results suggest that θ' may nucleate at either GP(I) zones or θ'' precipitates. Phillips⁽⁵⁵⁾ and Sato and Takahashi,⁽⁶³⁾ through electron microscopic studies, have supported this view and demonstrated that as ageing proceeds the GP(II) zones or θ'' grow, thicken and transform continuously to the semi-coherent θ' phase and continuously lose coherency. Clearer evidence about the nucleation of θ' has come from HVEM study by Suzuki and Kanno⁽⁹²⁾ on the Al-4%Cu alloy. They show that θ' nucleates mainly on dislocation loops leading to homogeneous distribution of θ' in an as-quenched and aged alloy while on direct ageing both homogeneous and heterogeneous distribution are observed depending upon available nucleation sites for θ' . It appears therefore, that θ' phase may nucleate at many different sites depending upon the prehistory of the material.

The loss of coherency due to the formation of dislocations at the interface of θ' has been studied by many investigators.⁽⁹³⁻⁹⁵⁾ Weatherly and Nicholson⁽⁹⁴⁾ have shown by contrast experiments in electron microscope that the broad faces of θ' plates are fully coherent at lower ageing temperatures and may contain widely spaced misfit

dislocations at higher ageing temperatures. Moreover, the structure of the planar interface contains misfit dislocations of the type $a \langle 100 \rangle$. Nemoto et al.⁽⁹⁵⁾ and Vaughan⁽⁹⁶⁾ confirmed these results through high voltage electron microscopic studies and x-ray diffraction. Laird and Aaronson,⁽⁹³⁾ however, found that dislocation arrays at the interface are due to plastic deformation accompanying transformation. In a recent study using lattice imaging of θ' , Sato et al.⁽⁹⁷⁾ observed complicated contrast effects which they related to the loss of coherency of θ' with the matrix.

Various studies^(93,98-101) have shown that the precipitates of θ' plates grow by a diffusional lengthening process. Sankaran and Laird⁽⁹⁸⁾ have suggested that the strain field around the growing plate influences the diffusional field and growth rate. During initial growth and coarsening, the coherent broad faces are immobile with respect to normal migration under the full range of driving forces available. This has been emphasized by both Laird and Aaronson⁽⁹³⁾ and Weatherly.⁽¹⁰²⁾ These interfaces move perpendicular to the habit plane by the lateral movement of ledges and the growth of precipitates takes place by ledge mechanism.⁽¹⁰³⁾ The heights of these ledges were proposed to be small multiples of c parameters, i.e. 20 nm.⁽⁹³⁾ Weatherly and Sargent's⁽¹⁰⁴⁾ study, by contrast, determined ledge step height to be 1.5-6.5 nm using TEM, which is somewhat larger than predicted by Laird and Aaronson. Bouazra and Reynaud⁽¹⁰⁵⁾ recently determined the values to be 0.29 and 2 nm using the convergent beam electron diffraction pattern and lattice plane imaging technique. The overall length and thickness of θ' precipitates grow continuously with square root of ageing time.⁽¹⁰¹⁾

Recently, Dahmen and Westmacott⁽¹⁰⁶⁾ have proposed a model of precipitate plate growth of θ' in Al-4.0%Cu alloy similar to the principles of conservative and non-conservative growth ledges proposed for {100} plate precipitate in Pt-C.⁽¹⁰⁷⁾ Fig. 2.18(a) is the [010] projection of the fcc lattice sites and Figs. 2.18(b) and (c) show the schematic representation of the transformation of the matrix to the body centred tetragonal (bct) unit cell of θ' . The total transformation can be visualized as consisting of two simple steps: (i) the shear vector of homogeneous transformation is $a/2 \langle 100 \rangle$ and may be envisaged as the passage of the partial dislocation with this burgers vector (Fig. 2.18(b)); (ii) the shuffles indicated in Fig. 2.18(c) are necessary to obtain the final bct arrangement shown in Fig. 2.18(d). The two steps describe the simplest way to achieve the structural part of the transformation. Solute diffusion is still necessary to accomplish the compositional part of the transformation. It is a homogeneous transformation. Lattice sites are conserved during the process, and the transformed and untransformed unit cells are separated by the shear vector $a/2 \langle 100 \rangle$ of the transformation. Dahmen and Westmacott have also mentioned that θ' can grow in a heterogeneous or non-conservative growth mode. This is illustrated in Fig. 2.19. Here the number of the lattice sites are not conserved and the sheared shell in Fig. 2.19(a) may be sheared by vector $a/2 \langle 100 \rangle$ and expanded to transform to the θ' structure the addition of Cu atoms at the sites indicated in Fig. 2.19b. This will "create" extra sites by leaving behind vacancies in the fcc lattice sites. The result is the formation of a $1/2$ unit cell of θ' (Fig. 2.19(c)) as opposed to the unit cell formed by the conservative process. These two processes are building

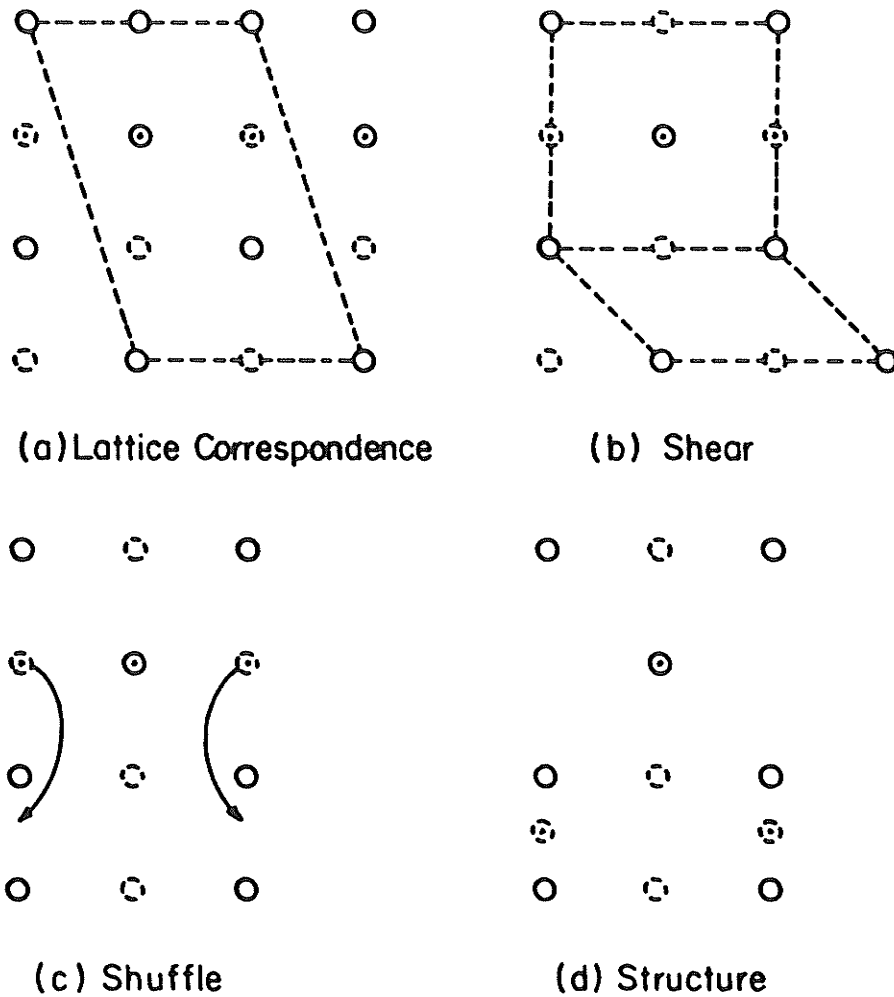


Fig. 2.18 [010] projection of the conservative fcc to θ' transformation. Full circles represent atoms at $Y = 0, 1$ and broken circles are atoms at $Y = 1/2$. Circles with dot in centre show a possible positioning of the Cu atoms. In (a) a 6-atom unit cell is outlined in the fcc lattice. The same cell is shown in (b) where the $a/2$ [100] shear component is resolved onto one plane. In (c) shuffles necessary after the shear are indicated (107)

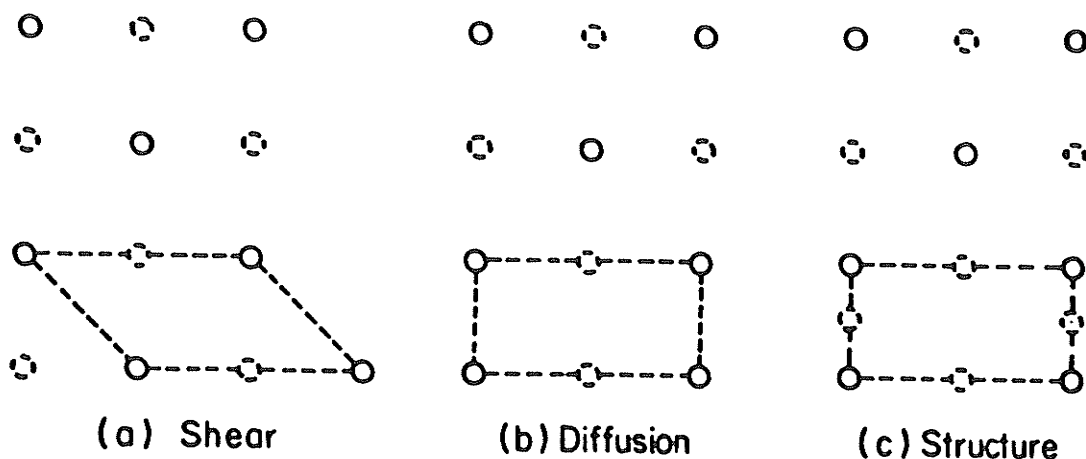


Fig. 2.19 [010] projection of the non-conservative fcc to θ' transformation with symbols as used in Fig. 2.18. The cell outlined in (a) is sheared into the AAA stacking by $a/2$ [100] shown in (b), and diffusion of Cu into the sites marked with arrows completes half a θ' unit cell as shown in (c) (107)

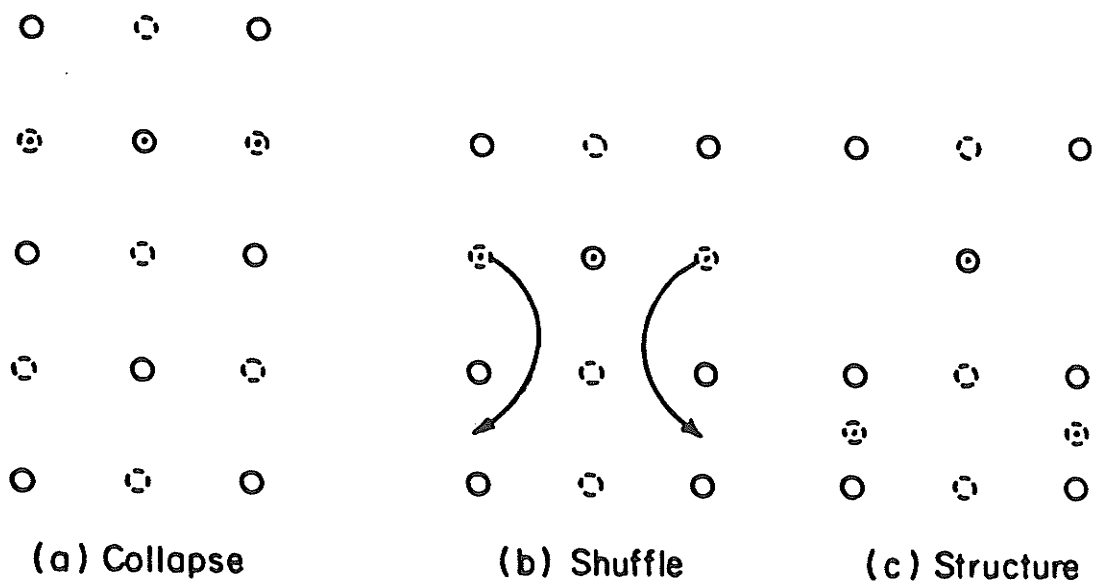


Fig. 2.20 [010] projection of non-conservative transformation from θ'' to θ' using symbols as in Fig. 2.18. In a θ'' precipitate of composition Al_3Cu a layer of vacancies condensing on the line indicated in (a) changes the local stoichiometry to Al_2Cu and produces a layer of AAA stacking. A shuffle of Cu atoms (b) completes the full θ' cell (c) (107)

blocks for the structural transformation that describes the precipitation of θ' in Al-Cu alloys. Multiple growth steps are made up of the combination of these two building blocks. In addition to studying θ' formation from solid solution, Dahmen and Westmacott also proposed a model for θ' formation from θ'' . They have suggested that in non-conservative ledge growth there is emission of vacancies. However, collapse of vacancies is also possible in the Al-Cu system during transition from θ'' to θ' as shown that in Fig. 2.20. The structural transformation is essentially the same as shown in Fig. 2.20(a). Dahmen and Westmacott compared these models with the results of several studies and found them to be in agreement with the available experimental data.

After an extended period of ageing, antiphase boundaries are observed in the ordered precipitates and are found to increase with increase in ageing time.⁽¹⁰⁸⁾ Kajiwara⁽¹⁰⁹⁾ observed striations in θ' precipitates in samples aged at 240°C for 4 days. He interpreted the striations to be stacking faults.

2.2.4 The θ Phase (CuAl_2)

The phase, θ (CuAl_2), is the final product of decomposition of the supersaturated solid solution, Al-Cu. It has a body centred tetragonal lattice (space group I14/mcm) with lattice parameters $a = 0.6054$ nm and $c = 0.4864$ nm. The arrangement of atoms in the unit cell is shown in Fig. 2.21. Guinier⁽⁷⁸⁾ investigated the orientation relationship of θ phase with the matrix and categorized it as follows:

$$\text{Group I} \quad : \quad [001]_{\theta} \parallel [001]_{\text{M}} ; [100]_{\theta} \parallel [110]_{\text{M}}$$

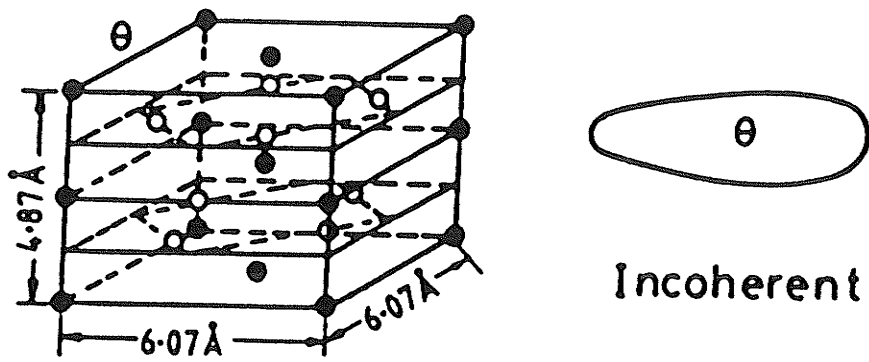


Fig. 2.21 Structure and shape of θ phase in Al-Cu alloys

Group II/III: $[001]_{\theta} \parallel [110]_M$; $[100]_{\theta} \parallel [001]_M$

Group IV/V: $[001]_{\theta} \parallel [001]_M$ with $[100]_{\theta}$ making an angle of $\pm 20^\circ$ with $[100]_M$

In addition to these Vaughan and Silcock⁽¹¹⁰⁾ have summarized more crystallographic relationships reported by other investigators.

An atomic fit at the interface between precipitate and matrix leads to a low value of interfacial energy and low activation energy for nucleation. The large number of orientation relationships gives rise to different kinds of precipitate morphology. The θ phase can form from θ' , or directly from the matrix with somewhat different orientation relationships.⁽¹¹⁰⁾ Direct formation of θ from θ' by rearrangement of atoms has been suggested.^(4,85,86) Maximum amount of θ' is present when θ begins to form and θ' disappears when the amount of θ is maximum.⁽¹¹¹⁾ However, most of the investigators accept independent nucleation and growth near or with θ' phase (for example, Heimendahl and Wasserman⁽¹¹²⁾ and Laird and Aaronson⁽⁹³⁾). The difference in suppositions on nucleation of θ phase is due to absence of an easy manner in which the perfect fcc lattice can rearrange into a perfect (Al_2Cu) lattice.⁽¹¹³⁾ Shchegoleva⁽¹¹³⁾ has proposed a model in which θ may be formed from a perfect fcc lattice as a result of small atomic displacements. The phase that appears may contain periodically distributed stacking faults which disappear as a result of ageing. However, it appears that nucleation of θ phase, like θ' , depends upon the prehistory of the material.

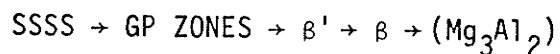
Heterogeneous nucleation of this phase also occurs at grain boundaries. Orientation relationships presented above, however, do not correspond to grain boundary precipitates.⁽³⁾ Vaughan and

Silcock⁽¹¹⁰⁾ have noted that additional abnormal orientations are obtained from these phases at grain boundaries. At longer ageing time the grain boundary precipitates drain the solute from nearby regions and narrow precipitate free zones (≈ 0.25 nm) are formed.⁽¹¹⁴⁾

The lengthening kinetics of θ precipitates have been studied in detail by Laird and Aaronson.⁽¹¹¹⁾ They found that growth is controlled by volume interdiffusion of aluminum and copper in the matrix.

2.3 PRECIPITATION IN THE BINARY Al-Mg ALLOY

The Al-Mg equilibrium diagram exhibits extensive solid solubility at the Al-rich end (Fig. 2.22). An alloy quenched from the α phase field shows the following precipitation sequence⁽¹⁴⁾



2.3.1 GP Zones

It can be seen from the solvus curve of GP zones in Fig. 2.22 that the critical temperature above which these zones do not form is very low ($47^\circ\text{-}67^\circ\text{C}$). Formation of GP zones occurs within seconds from quenching in high energy areas (grain boundaries, dislocations, etc.).⁽¹³⁾ Dauger et al.⁽¹¹⁵⁾ in an x-ray study on Al-12%Mg alloy aged at room temperature reported them to be spherical. They are very small in size during initial stages of ageing at room temperature (1.0-1.5 nm dia.) and most of the quenched-in vacancies remain around them as clouds. As a result there is little strain and no appreciable hardening. Upon continued ageing at room temperature

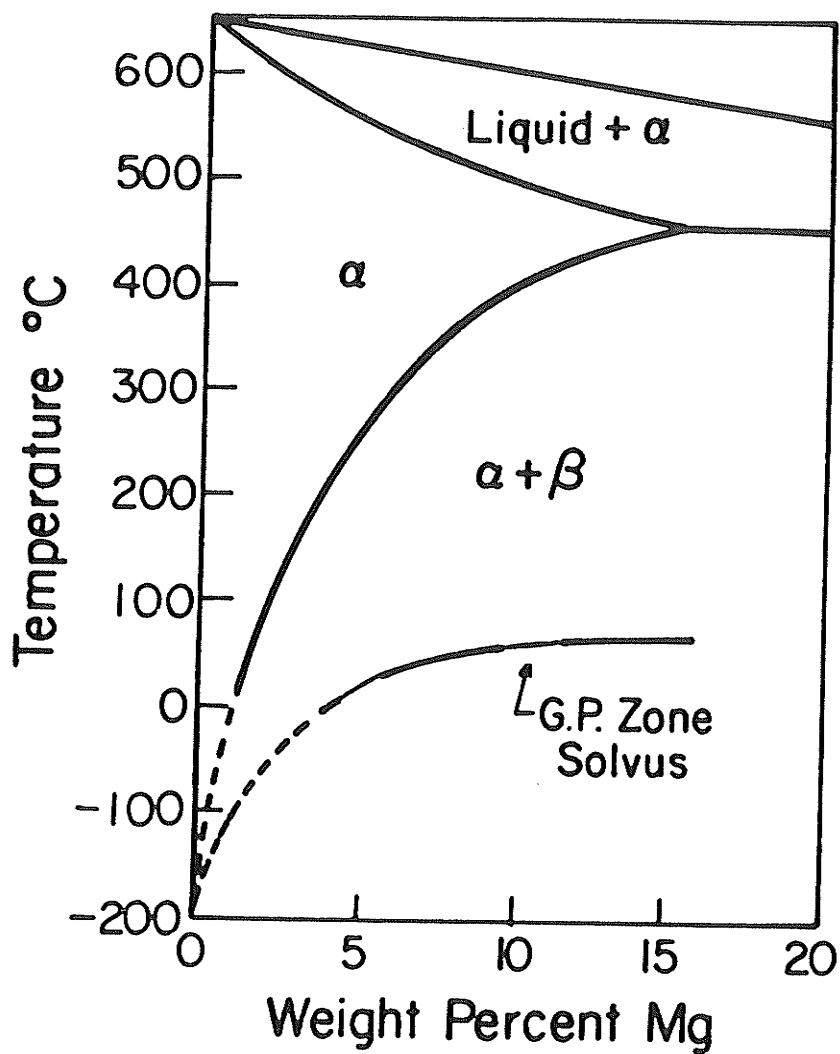


Fig. 2.22 Al-Mg equilibrium diagram to which the GP zone metastable boundary has been added⁽¹⁴⁾

these zones grow to up to 10 nm diameter. Bernole et al.^(116,117) used TEM to detect coherent Mg rich zones of density of approximately 10^{17} m^{-3} in an Al-10.0%Mg alloy which had been aged at room temperature for 13 years.

Boudili et al.⁽¹¹⁸⁾ used TEM and x-ray small angle scattering to study Al-9.5 and 14.8% Mg alloys aged at 20°C. They have reported that the dilute alloy decomposed to form ordered GP zones with the Li_2 (Al_3Mg) superstructure. The concentrated alloy decomposed to produce a modulated structure in the $\langle 100 \rangle$ directions which they interpreted as evidence of spinodal decomposition.

2.3.2 The β' Phase

This phase has a hexagonal crystal structure with $a = 0.1002 \text{ nm}$ and $c = 0.1636 \text{ nm}$ ⁽¹³⁾ Saulnier and Mirand⁽¹¹⁹⁾ have reported the particles of the β' phase to be irregularly shaped plates formed on $\{100\}_M$ planes of an Al-12%Mg alloy aged at 120°C. Bernole⁽¹²⁰⁾ has carried out an extensive x-ray and TEM investigation of the precipitation behaviour of β' and β phases in an Al-10.0%Mg alloy. It is reported that β' phase nucleates heterogeneously on dislocations. It is often surrounded by extensive dislocation debris and, at the later states of ageing it is internally faulted on $\{10\bar{1}0\}$ planes. After ageing for 20 h at 200°C or 5 h at 250°C, irregular plates up to 0.5 μm thick were observed on $\{100\}_M$. The plates were usually oval shaped and elongated along $\langle 100 \rangle_M$. The orientation relationship between the β' plates and the aluminum matrix was reported by Bernole to be:

$$(0001)_{\beta'} \parallel (001)_M ; [01\bar{1}0]_{\beta'} \parallel [110]_M .$$

2.3.3 The β Phase

The equilibrium β phase (Mg_3Al_2) has a fcc crystal structure with $a = 2.824 \text{ nm}$ ⁽¹²¹⁾ Bernole⁽¹²⁰⁾ reported that β phase forms preferentially at grain boundaries and at the matrix/ β' interface. Both plate and lath morphology were reported and the former exhibited the following orientation relationship:

$$(111)_{\beta} \parallel (001)_{M} ; [110]_{\beta} \parallel [010]_{M} .$$

2.4 PRECIPITATION IN THE TERNARY Al-Cu-Mg ALLOY

The Al-rich corner of the Al-Cu-Mg equilibrium diagram is shown in Fig. 2.23(a). The isothermal section of the ternary diagram shows that phases which may be in equilibrium with Al-rich terminal solid solution, are θ , S, T and Mg_2Al_3 . The composition and crystal structures of these phases are listed in Table 2.2.

It can be seen from Fig. 2.23(b) that the formation of different phases due to ageing depends upon the Cu/Mg ratio. Results of various studies on high purity alloys are summarized in Table 2.3. When the Cu/Mg ratio is 0.46, T' (Al_6CuMg_4) precipitates form along with S' (Al_2CuMg) phase. However, an increase in Cu/Mg ratio to 2.2 results in precipitation of only the S' phase. On further increase in the Cu/Mg ratio, θ' ($CuAl_2$) phase forms along with the S' phase.

The Al-Cu-Mg alloys having a Cu/Mg ratio of 2.6 form pseudo-binary Al- $Al_2CuMg(S)$ system⁽¹²⁴⁾. Bagaryatsky⁽¹²¹⁾ and Silcock⁽¹²²⁾ used x-ray diffraction techniques to show that the decomposition of the supersaturated solid solution (SSSS) of the pseudo-binary alloy takes place in the following general sequence.

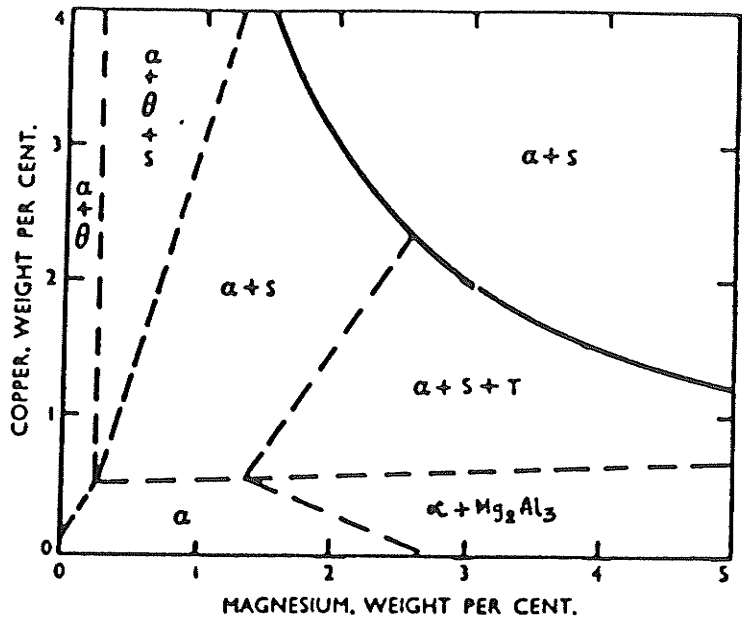


Fig. 2.23(a) Phases present in Al-Cu-Mg system after long term ageing at 190°C (123)

— Phase boundaries at 500°C
- - - Possible boundaries at 190°C

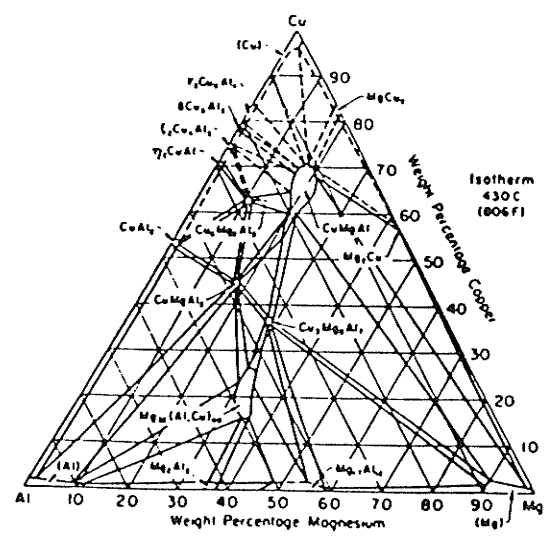


Fig. 2.23(b) Isotherm of the Al-Cu-Mg system at 430°C (124)

Table 2.2 Phases present at the aluminum corner of Al-Cu-Mg equilibrium diagram (Isotherm 430°C)(124)

Phases	Composition	Crystal Structure
T	Al_6CuMg_4	Cubic
S	CuMgAl_2	Orthorhombic
θ	CuAl_2	bct
β	Mg_2Al_3	Cubic

Table 2.3 Summary of published information on the ageing characteristics of high purity ternary Al-Cu-Mg alloys

S. No.	Alloy composition (wt%)			Phases reported after ageing at temp. T		Ref. Nos.
	Cu	Mg	Cu/Mg Ratio	Phases	T (°C)	
1	0.96	2.10	0.46	S + T	200	125
2	2.00	1.10	1.82	S	200	125
3	2.7	1.36	1.98	S	325	94
4	3.3	1.58	2.08	S'	190	126, 127
5	1.29	0.69	2.2	S'	190	122
6	3.15	1.52	2.2	S'	190	122
7	2.00	0.9	2.2	S'	200	128
8	3.00	1.15	2.61	S'	180-240	129-131
9	2.5	0.5	5.0	S' + θ'	190	151
10	3.53	0.48	7.00	S' + θ'	190	122
11	1.71	0.33	7.00	S' + θ'	190	122
12	3.3	0.27	12.22	S' + θ'	230	132

SSSS → GPB ZONES → S'' → S' → S

2.4.1 GPB(I) Zones

Most of the early work, notably by Bagaryatsky⁽¹²¹⁾ indicated that room temperature ageing of Al-Cu-Mg alloys caused the formation of clusters of atoms composed of 1 Cu, 1 Mg and several Al atoms. Silcock⁽¹²²⁾ termed these clusters of atoms GPB zones, in honour of Bagaryatsky, and in order to distinguish them from the GP zones observed in binary Al-Cu alloys. Many models have been proposed to describe the crystal structure of GPB zones.^(122,129,130,133,134) Gerold⁽¹³³⁾ has suggested that these are regions of an ordered CuAuI type phase with tetragonal lattice in the initial stages of ageing. Silcock⁽¹²²⁾ has shown the GPB zones to be an ordered phase with a tetragonal lattice. Shchegoleva and Buynov⁽¹³⁴⁾ determined the structure of the zones to be similar to the S'' phase and preferred to call them S'' phase instead of GPB zones. Alekseyev et al.⁽¹²⁹⁾ however, have presented a different model for GPB zones. They have suggested that GPB zones have the same crystal structure as equilibrium S phase and a lattice isomorphous to the matrix. Mondolfo⁽¹³⁾ has shown the arrangement of atoms in the GPB zone lattice as shown in Fig. 2.24 which also illustrates its crystallographic relationship with the matrix. In a recent study⁽¹³⁵⁾ which used hardness, Laue x-ray diffraction and high resolution microscopy to study the precipitation behaviour of the Al-4%Cu-1.5%Mg alloy, it was concluded that the GPB zones are divided into two zones, namely GPB(I) and GPB(II). The GPB(I) zones have a random arrangement of atoms while GPB(II) zones

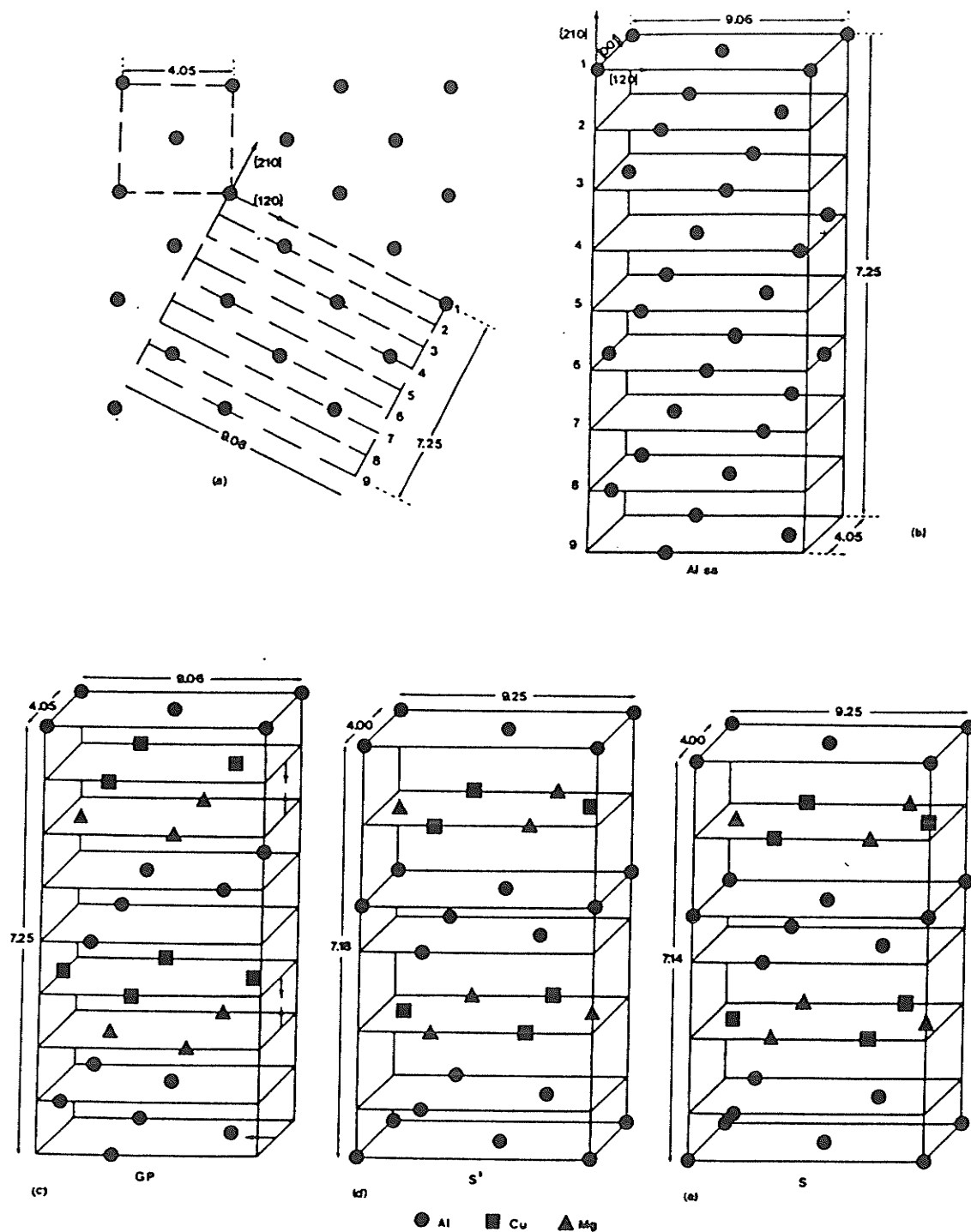


Fig. 2.24 Formation of S phase from supersaturated solid solution. (a) the relative orientation of the precipitate with respect to the matrix; (b) Al solid solution; (c) GPB zones; (d) S' phase; (e) S phase(13)

are similar to the S'phase and have an ordered arrangement of atoms. The GPB(II) zones are rod shaped, lying parallel to $\langle 100 \rangle$ matrix direction.

Gerold and Haberkorn⁽¹³³⁾ considered the zones to be spherical while Alekseyev et al.⁽¹²⁹⁾ reported equiaxial particles with a minimum size of 7.0 nm. Most of the investigators, for example Silcock,⁽¹²²⁾ suggest GPB zones to be cylindrical particles lying along $\langle 100 \rangle_M$ directions. She found the zones to be 2.0 nm in diameter and 4.0 nm long.

The zone formation in an Al-3%Cu-1%Mg alloy has been examined by Pabi and Mallik⁽¹³⁶⁾ using a resistivity technique. It was reported that quenched-in vacancies were strongly bound to the solute atoms or zones. Consequently, a slow reaction should be maintained for several weeks during room temperature ageing.⁽¹³⁷⁾ Cho⁽¹³⁸⁾, using resistivity, hardness and TEM, confirmed the presence of the slow reaction in the Al-2%Cu-1.1%Mg alloy. It was also shown that pre-precipitation in this alloy occurs in three different stages; (i) GPB zone formation during quenching and ageing for less than 1 min (known as fast reaction); (ii) GPB zone formation in the early stages of ageing below 200°C (known as slow reaction), and (iii) GPB(II) zone formation in the early stages of ageing at about 250°C.

When the concentration of solutes is increased at the same Cu/Mg ratio the density of dislocation loops and helices increases. Consequently, the rate of GPB zone formation is high in alloys with a higher solute content for a given Cu/Mg ratio.⁽¹³⁸⁾ The rate of zone formation is critically related to the ageing temperature. Cho⁽¹³⁸⁾ studied an Al-2%Cu-1.1%Mg alloy and found that the rate of

GPB zone formation is highest when ageing is carried out at a temperature between 70°-120°C.

The GPB zone solvus curve has been determined by many investigators.^(68,126,138) Beton and Rollason⁽⁶⁸⁾ determined the reversion temperature of GPB zones to be 260°C using hardness experiments and this was confirmed by Sen and West.⁽¹²⁶⁾ Cho,⁽¹³⁸⁾ on the basis of his resistivity measurements on Al-2%Cu-1.1%Mg alloy, found that reversion rate of zones is very slow up to 230°C, while at 240°C it increases anomalously and zones dissolve in 7 min. He concluded that the thermal stability of the GPB zones in Al-Cu-Mg alloys is higher than their counterpart in Al-Cu alloys. DSC curves of Al-3.15%Cu-1.52%Mg alloy due to Howie,⁽¹⁴²⁾ support the observation of Cho.

The solubility curves of GPB(I) zones have not been widely studied. They can be represented by an equation of the type⁽⁶⁸⁾

$$\log [X] = A - K/T$$

where X is solute concentration, A and K are constants, and T is absolute temperature.

2.4.2 GPB(II) Zones (or S" Phase)

In an x-ray study on Al-4.0%Cu-1.2%Mg, Lambot⁽¹⁴⁰⁾ observed a "checkerboard" pattern which could not be explained. Bagaryatsky⁽¹²¹⁾ associated this pattern to the presence of a distinct phase, named S", which has a slightly distorted equilibrium S structure, but with different matrix coherence. Silcock,⁽¹²²⁾ using the x-ray diffraction technique on low temperature aged Al-Cu-Mg alloy single crystals did

not observe any structure resembling the S'' as reported by Bagaryatsky. However, a new structure termed GPB(II) zone was observed after ageing at elevated temperatures (i.e. $\geq 240^\circ\text{C}$). These zones were larger in size and sharper in shape than GPB(I) zones. Wilson and Partridge⁽²³⁾ and Weatherly⁽¹⁴¹⁾ using TEM technique also did not observe S'' phase after ageing at 190°C . On the other hand, Althof et al.,⁽¹⁴³⁾ using TEM, observed S'' particles 1.0 nm wide and 5.0 nm long in a naturally aged sample. Schegoleva and Buynov,⁽¹³⁴⁾ in an x-ray study on Al-3.0%Cu-1.15%Mg alloy, inferred that a cluster of solute atoms with internal ordering is formed on quenching this alloy. They called it S'' phase instead of the GPB zones mentioned in Section 2.4.1. The S'' phase is cylindrical in shape and is formed at the very beginning of isothermal ageing. During the initial period of ageing, the S'' phase particles grow in length but do not alter in diameter. In later stages, however, diameter is also increased and causes strong elastic distortion of cylindrical symmetry within the matrix. In another study, Schegleyeva and Buynov⁽¹³⁴⁾ determined the crystal structure of S'' phase and proposed that it has a peculiar structure with abnormal orientation relationships with the matrix. Cuisat and co-workers,⁽¹⁴⁴⁾ in a study of an aged Al-2.8%Cu-1.4%Mg alloy by TEM, confirmed the presence of S'' phase during the initial stages of ageing. They also reported that S'' phase contains antiphase domains within the structure. Takahashi and Sato⁽¹³⁵⁾ in a high voltage lattice imaging study reported the presence of ordered rod shaped GPB(II) zones lying in $\langle 100 \rangle$ matrix. They pointed out that these zones have a crystal structure similar to that of the S phase.

In spite of a detailed study carried out by several workers,

as presented in this and the previous section, the crystal structure of GPB zones is not unambiguously established.

2.4.3 The S' Phase

The crystal structure of S' phase is orthorhombic with lattice parameters $a = 0.404$ nm, $b = 0.925$ nm, and $c = 0.718$ nm. The stoichiometric formula of this phase is reported to be CuMgAl_2 (Fig. 2.24). From x-ray investigations, S' has been found to form with the following orientation relationship^(121,122)

$$[100]_{S'} \parallel [100]_M ; [010]_{S'} \parallel [021]_M ; [001]_{S'} \parallel [01\bar{2}]_M$$

giving a total of 12 possible orientations in the matrix.⁽⁹⁴⁾ A detailed study on the nucleation and growth of S' phase was carried out by Wilson and Partridge.⁽²³⁾ An Al-2.5%Cu-1.5%Mg alloy aged at 190°C was examined by TEM, and S' precipitates were found to nucleate heterogeneously on dislocations. The precipitates grew as laths on $\{210\}_M$ planes in $\langle 100 \rangle_M$ directions. Corrugated sheets of precipitates are formed by laths which have a common $\langle 100 \rangle$ growth direction and which form on alternating $\{210\}$ planes (Fig. 2.25). At low magnification these sheets appear to be large precipitates on $\{110\}_M$ planes. Wilson and Partridge also showed that deformation of the alloy prior to ageing had the effect of refining S' precipitate distribution.

Alekseyev and co-workers⁽¹³⁰⁾ proposed a model to explain the coherency loss in Al-Cu-Mg alloys. According to this model the coherency of S' phase is lost along the b-axis and accompanied by an absorption of excess vacancies. Alekseyev et al. have also explained

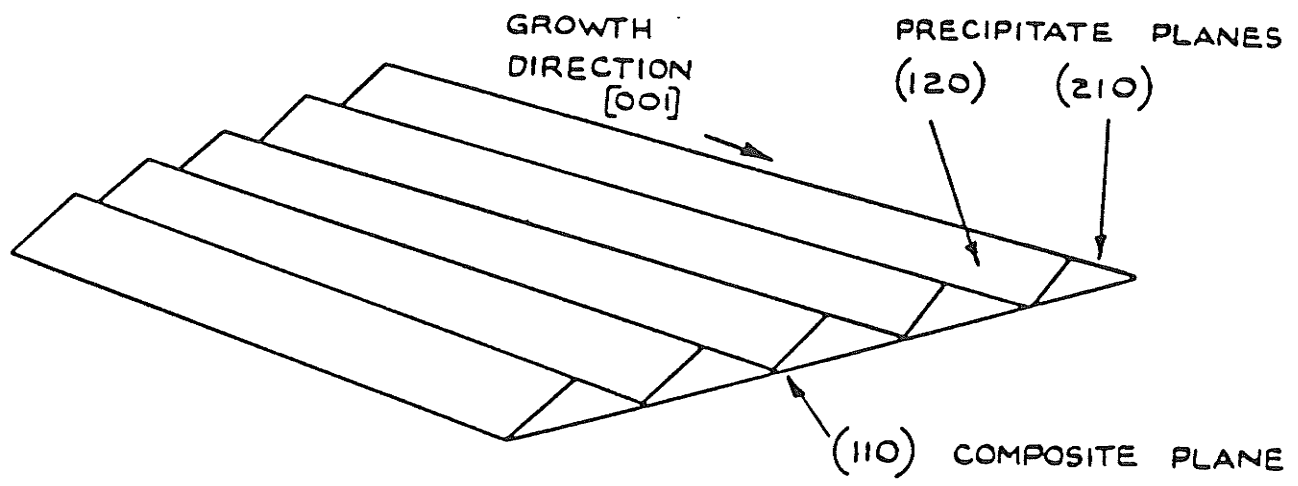


Fig. 2.25 The formation of a composite precipitate sheet on a (110) plane by the growth of precipitate paths on (120) and (210) planes in [001] direction (23)

the development of S' particles. As a result of ageing, the GPB zones (4.0 nm) grow in size along $\langle 021 \rangle_M \parallel \langle 010 \rangle_{S'}$ (b-direction) with simultaneous flattening in the $(01\bar{2})_M \parallel (001)_{S'}$ plane.⁽¹²⁹⁾ After a certain size the mismatch between the precipitate particles and matrix becomes zero along the b-direction and the particles lose coherency. Growth in c-direction is difficult because the elastic strain due to "shear mismatch" between phase and matrix is greater. The growth remains most rapid in a-direction and the S' acquires the shape of laths.

The kinetics of coarsening in an Al-2.0%Cu-1.1%Mg alloy aged at 200°C and 230°C has been studied using TEM.⁽¹⁴⁵⁾ The coarsening of S' precipitates takes place by Ostwald ripening and the distribution of precipitates remains uniform. Cho⁽¹⁴⁵⁾ also showed that the diffusion coefficient ($D_{Cu-Mg} = 7.03 \times 10^{-14}$ cm²/sec at 200°C) calculated from kinetic analysis, was 10^3 times the diffusion coefficient of Cu and Mg in pure aluminum. The aspect ratio of lath shaped S' precipitates increased with temperature and time.

2.4.4 The S Phase

The S phase is orthorhombic (space group CmCm) with lattice parameters⁽¹⁴⁶⁾ $a = 0.400$ nm, $b = 0.923$ nm and $c = 0.714$ nm (Fig. 2.24). It has the same orientation relationship with the matrix as S' phase.

Weatherly and Nicholson⁽⁹⁴⁾ studied the loss of coherency of lath shaped S precipitates in Al-2.7%Cu-1.36%Mg alloy aged for 24 h at 325°C. They found that S-laths lost coherency by first attaching the matrix dislocations to the lath/matrix interface. It was followed by the formation of an array of dislocation loops with

Burgers vector of type $a/2 [101]$ spaced along the length of the laths. The average spacing of the loops was 26.0 nm compared to a value of 17.0 nm if there was complete relief of misfit. They also found that S phase loses coherency less rapidly than do the θ' plates in Al-4.0%Cu alloy. For example, after 4 days of ageing at 260°C, many θ' plates in Al-4.0%Cu alloy started to lose coherency, whereas after 25 days at the same temperature most of the S laths in Al-2.7%Cu-1.5%Mg alloy were still coherent.

Sen and West⁽¹⁵³⁾ studied the influence of various factors on the precipitation of S phase in an Al-3.3%Cu-1.6%Mg alloy aged at 260°C after various conditions of initial quenching, pre-ageing and plastic deformation. They found that a reduction in the quenching rate slightly reduced the subsequent hardening on ageing which was accompanied by a slight coarsening of S laths. Cold working accelerated the subsequent ageing and refined the S lath size, as a result of enhanced nucleation on dislocations. The pre-ageing treatment had both positive and negative effects on hardening depending upon the pre-ageing temperature, which was related to the supersaturation condition. They also found that the coarsening of S phase follows the Lifshitz-Slyozov-Wagner (LSW) theory of coarsening.

2.4.5 The Distinction Between S' and S Phase

It was stated in Section 2.4.3 that the crystal structures of both S' and S phase are orthorhombic and their lattice parameters are close to each other. Silcock⁽¹²²⁾ found that distinction between these two phases is very slight and somewhat arbitrary. Wilson and Partridge⁽²³⁾ found that S' and S phase have the same crystal structure

as S phase but with slightly different lattice parameters. Alekseyev et al.⁽¹³⁰⁾ agree that the S' phase has the same crystal structure as S phase but suggest that the S' phase has "broken coherency" along the b-axis. Wilson⁽¹²⁷⁾ also attempted to differentiate between S and S' precipitates by their morphologies. He identified S' phase as lath shaped precipitates formed at lower ageing temperatures and S phase as massive precipitates observed in specimens aged at higher temperatures. Thus, there appears to be no clear cut distinction between the S and S' phases.

2.4.6 Effect of Precipitation on Hardness and Tensile Properties

The effect of precipitation on hardness of high purity Al-Cu-Mg alloys have been measured by several investigators. Hardy⁽⁴⁾ showed that hardness of high purity Al-Cu-Mg alloys is strongly dependent on the heat treatment of the alloy (Fig. 2.26) and its solute content (Fig. 2.27). Silcock,⁽¹²²⁾ in an x-ray diffraction study of Al-3.15%Cu-1.5%Mg alloy, related the observed changes in hardness with ageing time at different temperatures to the microstructural changes. Fig. 2.26 due to Silcock⁽¹²²⁾ correlates the hardness with various precipitating phases in this alloy.

Very little information is available on the tensile properties of the high purity Al-Cu-Mg alloys. However, it is expected that the tensile strength would also behave in a similar manner to the hardness. Wilson et al.⁽⁷⁾ have reported that the 0.2% yield strength of quenched Al-2.5%Cu-1.2%Mg alloy increases by 140% due to ageing for 90 min at room temperatures. They attributed this increase in strength to the formation of GPB zones. Further ageing at 190°C for

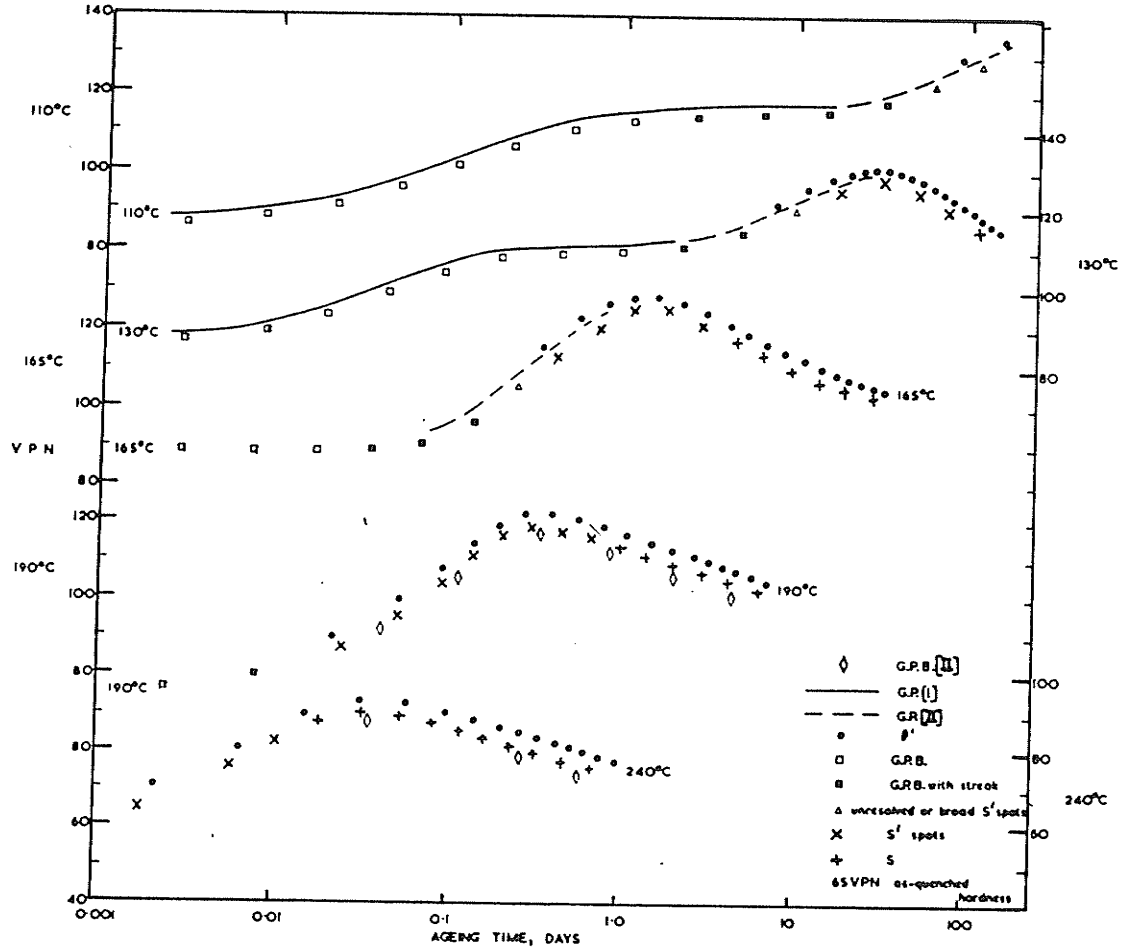


Fig. 2.26 Structures occurring at various points on the hardness curve for acetone - quenched and aged Al-3.53% Cu-0.48% Mg alloy(122)

16 h resulted in precipitation of S' phase and increased 0.2% yield strength by 200%.

Robinson and Hunter⁽¹⁴⁷⁾ measured the tensile properties of a series of Al-Cu-Mg alloys aged at room temperature for 4 days. Their results are plotted in Fig. 2.28. It shows that the yield strength of the alloys increases linearly with the increase in the total solute content up to 5.25%. This is consistent with the hardness results of Hardy⁽⁴⁾ as shown in Fig. 2.27.

2.5 EFFECT OF SMALL QUARTERNARY ADDITIONS ON THE PRECIPITATION BEHAVIOUR OF Al-Cu-Mg ALLOYS

The addition of small amounts of solutes to various aluminum alloys has been shown to modify the precipitation reaction appreciably. Several mechanisms by which solutes may modify the precipitation behaviour have been recognized.⁽¹⁶⁹⁾ Some of these are listed below:

- (1) Interaction with vacancies which leads to a reduction in the rate of lattice diffusion of substitutional elements,
- (2) Modification of the interfacial energy between the precipitate and the matrix and the rate of nucleation.
- (3) A change in free energy relationship in an alloy system, so that precipitation of different phases is favoured.
- (4) Segregation to grain boundaries and inhibition of discontinuous precipitation, nucleation, etc.

These effects of small additions are generally valid but there are no rules which govern the behaviour of individual solutes.⁽¹⁰⁾ Most of the early work on the effects of small addition of solutes on the Al-Cu-Mg alloy system has been reviewed by Hardy.⁽⁵⁾

2.5.1 Silver

Addition of silver to Al-Cu-Mg alloys has been widely studied by many investigators.^(123,132,148,150-153) Polmear⁽¹⁴⁸⁾ has shown that alloys based on the Al-Cu-Mg system are greatly affected by the addition of silver although it has almost no effect on the Al-Cu alloy. The silver atoms interact with vacancies to reduce the GPB zone formation and improve mechanical properties. Sen and West⁽¹⁵³⁾ observed a similar increase in peak hardness when silver was added to the alloy, Al-3.2%Cu-1.5%Mg. Studies on a wide range of ternary and quaternary alloys showed that the addition of silver increased the hardening rate, when ageing was conducted in the medium temperature region. This was attributed to the formation of a uniformly distributed BCC $Mg_{32}(AlZn)_{49}$ type phase.^(123,126,150) Sen and West⁽¹²⁶⁾ postulated that the silver atoms are somehow responsible for trapping vacancies and hence fewer dislocation loops formed in the quaternary alloy. With fewer nucleation sites, formation of S phase is restricted and the T phase is formed. Silver also promotes the formation of an entirely new phase. Aultz and Vietz⁽¹⁵²⁾ observed GPB(II), S' and θ' precipitates in an Al-2.5%Cu-0.5%Mg alloy aged to peak hardness at 200°C. The addition of 0.5% Ag to this alloy resulted in the formation of a new precipitate along with a fairly small amount of lath shaped S-precipitate. The new phase was a hexagonal shaped plate type precipitate formed on {111} matrix when ageing was done at a temperature between 135°-350°C. Chester⁽¹⁵¹⁾ and Aultz and Vietz⁽¹⁵²⁾ found the new phase has a hexagonal crystal structure with lattice parameters $a = 0.496$ nm, $c = 0.848$ nm and it is oriented with $[00.1]_{hex} \parallel [111]_M$ and $[10.0]_{hex} \parallel [\bar{1}\bar{1}0]_M$. The same phase was observed in

Al-4.4%Cu-0.27%Mg-0.7%Ag alloy by Taylor et al.⁽¹³²⁾

2.5.2 Transition Elements, Ti, Mn, Fe and Ni

Cho et al.⁽¹⁵⁴⁾ studied the influence of Ti, Mn and Fe addition on Al-Cu-Mg alloys by DSC and TEM. They have reported that the addition of Mn causes the rate of GPB zone formation to increase and that this effect becomes pronounced by the addition of Ti. Conversely, Fe reduces the rate of GPB zone formation. The combined addition of Fe, Mn and Ti increases the rate of GPB zone formation by small amounts, but the nucleation and growth of S' is reduced considerably.⁽¹⁵⁴⁾

Wilson and Forsyth⁽¹⁵⁵⁾ studied the effect of 1% Fe and 1% Ni addition on the age hardening characteristics of Al-2.5%Cu-1.2%Mg alloys using TEM and tensile testing techniques. They found that the addition of both solutes reduced the ability of this alloy to age harden. The solutes combined with Cu and Al atoms to form insoluble phases and reduced the Cu content of the solid solution. The combined (1% Fe and 1% Ni) addition of both the elements, however, restored the age-hardening capability of the alloy by forming a Ni/Fe rich phase with little copper in it.

2.5.3 Silicon

Wilson and Partridge⁽²³⁾ have shown that the effect of the addition of 0.25% Si to an Al-2.5%Cu-1.5%Mg alloy is similar to that of cold work prior to ageing, namely, the S' phase becomes more finely dispersed. In a subsequent paper, Wilson⁽¹²⁷⁾ studied the effect of Si addition in detail and concluded that a strong binding energy

between Si atoms and vacancies reduced the number of dislocation loops and also decreased the diffusion rate of solute in this alloy. This resulted in a decreased rate of GPB zone formation, and a higher density and more uniform dispersion of S' precipitates. This observation was further confirmed by Cho et al.⁽¹⁵⁴⁾ Wilson⁽¹²⁷⁾ has further reported that addition of 0.24% Si to the alloy also causes a strong bonding between solute atoms, vacancies and GPB zones, so that the stability of the zones is enhanced and the temperature at which S' could be formed is raised.

Suzuki et al.⁽¹²⁸⁾ observed increases in hardness of Si containing Al-2.0%Cu-0.9%Mg alloy isochronically aged at different temperatures for 100 min (Fig. 2.29). They reported that the increase in hardness of the aged ternary alloy is due to the change in aged microstructure that had three kinds of precipitates in contrast to the one type of precipitate formed in the Si free alloys. Moreover, addition of 0.5% Si to dilute Al-2.0%Cu-0.9%Mg alloy promoted the precipitation of θ' and suppressed the precipitation of S' phase. These results have not been confirmed so far by any other investigator. Suzuki et al. have further reported that the addition of Si to a concentrated alloy (Al-4.0%Cu-1.8%Mg) has the tendency to lower the peak aged hardness.

The complex effect of Si may be rationalized in terms of the Al-Cu-Mg-Si phase diagram. Two sections through the Al-Cu-Mg-Si system at 1.4% Cu and at constant temperature and pressure are shown in Fig. 2.30.^(156,157) The presence of many phases in the aluminum corner of the equilibrium diagram at 520°C and at 175°C should be noted. This suggests that ageing of a supersaturated solid solution

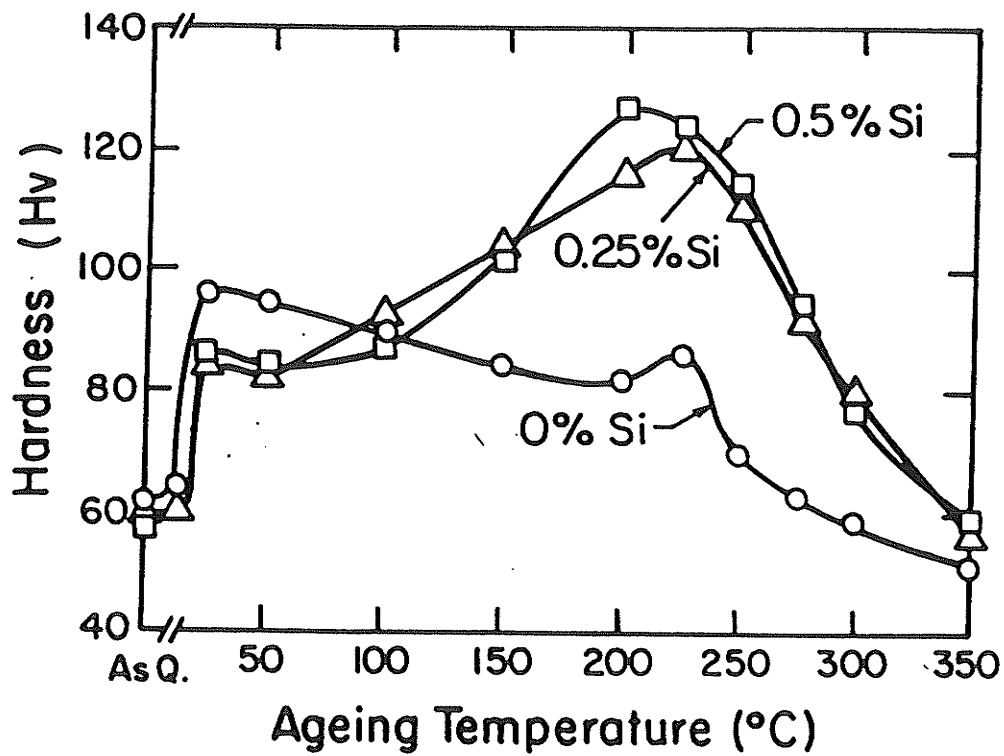


Fig. 2.29 Hardness vs. ageing temperature curves of Al-2% Cu-0.9% Mg alloys having different Si contents. Specimens were solution-treated at 505°C for 1 h, quenched into iced water and isochronally aged for 100 min⁽¹²⁸⁾

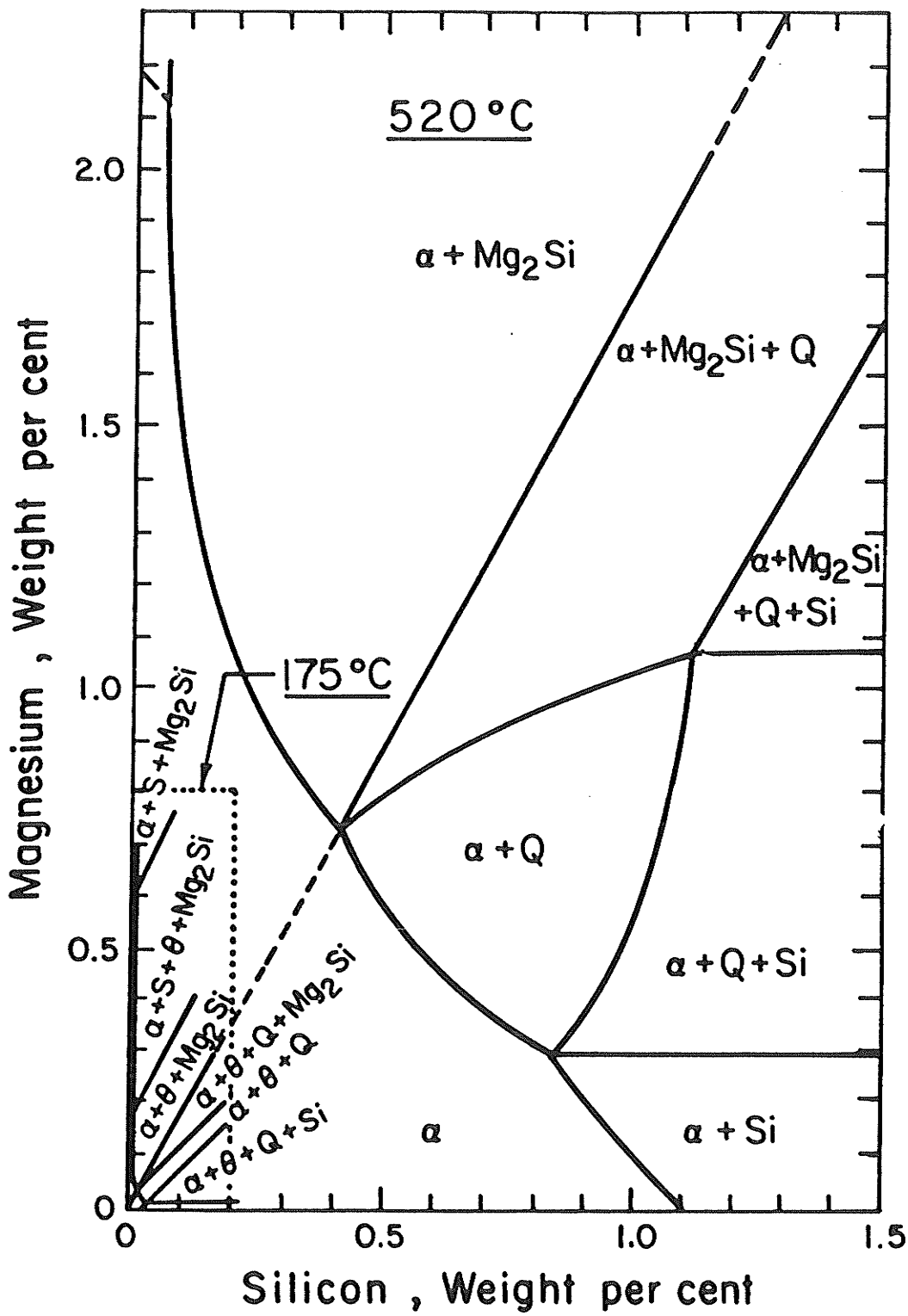


Fig. 2.30 Sections at 1.4% copper of the isotherms of the Al-Mg-Si-Cu system at 520°C and 175°C (156)

at 175°C may cause the precipitation of many types of phases. These are: (i) CuMgAl_2 - S type; (ii) CuAl_2 - θ type; (iii) Mg_2Si - β type and (iv) $\text{Cu}_2\text{Mg}_8\text{Si}_6\text{Al}_5$ - Q type. The type of phase precipitates on ageing is known to depend mainly upon the Cu/Mg and Mg/Si ratio in the alloy.⁽¹³⁾ The ageing behaviour of alloys in which the Cu content is at or above the solubility limit (4-5% Cu) and Mg and Si are present in small amounts or in the proportions to form Mg_2Si , is very similar to the Al-Cu alloys.⁽¹³⁾

The second group of alloys has a Cu/Mg ratio of at least 2.5 and usually a low (< 0.2) Si content, so that most of the Mg is combined with copper to form CuMgAl_2 . The ageing characteristics of this second group of alloys differ only slightly from those of ternary Al-Cu-Mg alloys. Moreover, if Si is present, the Mg/Si ratio for the formation of the CuMgAl_2 must be above 1.73, i.e. there must be more Mg in alloys than the amount necessary for the formation of Mg_2Si . If there is more copper than the amount necessary to form this compound, CuAl_2 will be formed.⁽¹³⁾

The third group of alloys in which copper is very low (< 0.4%) or Mg content is decidedly higher than the Si content, the ageing characteristics correspond to those of ternary Al-Mg-Si alloys.⁽¹³⁾

The fourth group comprises the alloys in which the Cu content is approximately one half of Mg and Si content is the same as or higher than the Mg content. The age hardening of these alloys is mainly due to the precipitation of $\text{Cu}_2\text{Mg}_8\text{Si}_6\text{Al}_5$ phase.

The amount of Si present at a fixed Cu/Mg ratio will determine the type of phase that will form on ageing. If Mg/Si ratio is exactly equal to 1.73, all the Mg and Si will combine to form Mg_2Si . On the

other hand, if Mg:Si ratio is precisely 1.08, all the Mg and Si would combine with copper to form the quaternary phase $\text{Cu}_2\text{Mg}_8\text{Si}_6\text{Al}_5$, with the excess copper being present as CuAl_2 . If the ratio of Mg to Si is between 1.08 and 1.73, some Mg_2Si will also be present. If it is below 1.08, there will be an excess of Si.⁽¹³⁾ Table 2.4 summarizes the phases observed in the quaternary Al-Cu-Mg-Si alloys on ageing at elevated temperatures.

Fig. 2.29 shows that the addition of 0.25 to 0.5% Si increases the hardness of Al-2.0%Cu-0.9%Mg alloy by about 50%. A similar observation has been made by Wilson et al.⁽¹²⁷⁾ They found that 0.25% Si in the alloy containing 2.5% Cu and 1.27% Mg can increase the yield strength by 75% on ageing at 190°C. Thus, Si additions appear to have a potential to increase strength of Al-Cu-Mg alloys.

2.6 SCOPE OF THE PRESENT WORK

The review of literature presented in the earlier sections shows that the precipitating phase in the ternary Al-Cu-Mg alloys with a Cu/Mg ratio close to 2.2 is S'. However, very little is known about the precipitation process in alloys with low solute concentrations. The kinetic parameters that control the precipitation rates have not at all been investigated. The distribution of the S' phase in the matrix and the unusual electron diffraction effects of the S' phase have also not been understood. In addition, very little work is done on the effects of increasing the amount of Si additions on the Al-Cu-Mg alloys although Si is a promising additive. In view of these factors the low solute containing Al-1.5%Cu-0.75%Mg alloy was chosen to study its precipitation behaviour by TEM and DSC

Table 2.4 Summary of published information on the ageing characteristics of Al-Cu-Mg alloys containing silicon

Item #	Alloy Composition (wt%)			Ratio		Phases reported	Ref.
	Cu	Mg	Si	Cu/Mg	Mg/Si		
1	2.42	1.25	0.24	2.08	5.2	CuMgAl ₂	127
2	2.39	1.23	0.26	1.94	4.73	CuMgAl ₂	127
3	2.00	0.900	0.25	2.2	3.6	CuMgAl ₂ + Mg ₂ Si + unknown x	128
4	2.00	0.900	0.50	2.2	1.2	CuAl ₂ + Cu ₂ Mg ₈ Si ₆ Al ₅ + unknown x	128
5*	4.00	0.8	0.8	5.0	1	CuAl ₂	158
6*	1.34	0.65	0.94	2.06	.69	CuMgAl ₂ + β	8
7*	2.39	0.42	0.24	5.69	1.75	CuAl ₂	159
8*	4.00	0.89	0.90	4.5	1	CuAl ₂	160
9*	2.50	1.3	0.70	1.9	-	CuMgAl ₂ + β	160

* Commercial alloys

techniques. An attempt was made to understand the crystallography and morphology of the S' phase and establish the kinetics of the overall precipitation process. The effects of Si additions (0.25, 0.50, 0.75 and 1%) on the precipitation behaviour were also examined.

CHAPTER III

EXPERIMENTAL TECHNIQUES AND PROCEDURE

3.1 MATERIALS AND PROCESSING

As-cast ingots, ($23 \times 15 \times 2 \text{ cm}^3$) of high purity aluminium alloys, whose chemical composition is given in Tabel 3.1, were supplied by the Aluminium Company of Canada. In order to prepare homogeneous and equilibrated specimens of the alloys, $3 \times 15 \times 2 \text{ cm}^3$ pieces were cut from each alloy and homogenized at 530°C for 48 h. The homogenized specimens were skimmed, upset forged and hot and cold rolled. About 70% reduction in area was given by hot rolling at 500°C in a number of passes. After each pass the specimen was annealed at 530°C for 10 min. The hot rolled alloys were equilibrated at 530°C for 12 h and water quenched to room temperature.

The equilibrated material was cold rolled ($\approx 80\%$) and used for preparing specimens for metallographic, differential scanning calorimetry (DSC), and transmission electron microscopic (TEM) studies. The specimens for the extraction of insoluble particles were prepared from the equilibrated material. Specimens for TEM were cut from cold rolled sheets, solution treated and quenched to room temperature. Different solution treatment temperatures were used in order to obtain approximately the same grain size in all the alloys. The solution treated specimens were aged at room temperature for 48 h which was followed by ageing at 130°C and 190°C for various lengths of time in an oil bath and an air furnace, respectively. The ageing temperatures were stable to $\pm 2^\circ\text{C}$. Specimens for optical and scanning electron microscopy (SEM) were cut from cold rolled sheets and solution

Table 3.1: Chemical composition of alloys.

Alloy #	Composition, Wt %			
	Cu	Mg	Si	Al
1	1.53	0.79	-	Bal.
2	1.52	0.74	0.23	Bal.
3	1.51	0.75	0.49	Bal.
4	1.54	0.75	0.76	Bal.
5	1.52	0.77	1.03	Bal.

treated at 530°C for 1 h. Some of the solution treated specimens were aged at room temperature followed by ageing at 130°C and 190°C for various lengths of time.

During the course of this investigation it was necessary to prepare a synthetic compound containing 19.3% Cu, 36.5% Mg, 30.2% Si and 14.0% Al for structural studies. Appropriate amounts of high purity (99.999%) elements, Cu, Mg, Si and Al, were melted in an induction furnace in an argon atmosphere. The as cast compound was vacuum sealed in a quartz tube and solution treated at 530°C for 300 h. The single phase structure of the compound was confirmed by optical and scanning electron microscopy.

3.2 EXTRACTION OF INSOLUBLE PARTICLES

Some of the alloys were found to contain insoluble particles. In order to identify and characterize them, 5 x 5 x 40 mm³ size specimens were used for electrochemical extraction of the insoluble particles. They were solution treated at 530°C for 6 h and water quenched. The solution treated specimens were stabilized at room temperature by ageing for 48 h and then further aged at 190°C for various lengths of time.

The precipitate particles were extracted by electrolytically dissolving the matrix of the heat treated specimens in a 2.5 wt% KI-methanol bath.⁽¹⁴²⁾ An aluminium strip kept inside the periphery of the 500 ml beaker containing about 300 ml of solution served as a cathode and a polished and cleaned bar of the specimen (5 x 5 x 40 mm³) suspended in the centre of the beaker served as the anode. A magnetic stirrer was continuously used during the anodic

dissolution which was carried out at 2-5 volts for 20-24 h at a current density of 40-80 mA/cm². Upon complete dissolution of the specimen the electrolytic bath was treated with 40 ml saturated aqueous solution of disodium ethylenediamine tetracetate (EDTA) for settling the suspended particles and the complex which formed during the electrolytic process. The clear liquid at the top was discarded and the remaining residue was treated with 40 ml of 50% HCl.⁽¹⁶¹⁾ The contents were centrifuged and decanted. The residue was washed thoroughly in distilled water and methanol several times and dried in an oven at 40°C.

3.3 OPTICAL MICROSCOPY

The alloy specimens were mechanically polished and etched with dilute Keller's etchant (1% HF, 1.5% HCl, 2.5% HNO₃ and 95.0% H₂O) to reveal the microstructure and the grain size of the specimens.⁽¹⁶²⁾ Some of the specimens were also etched with the saturated molybdic acid containing 10% HF in distilled water to reveal the grain size and the insoluble particles present in the alloys.⁽¹⁶³⁾ The ASTM intercept method⁽¹⁶²⁾ was used to measure the grain size of the alloys in a Lietz Tas Plus image analysis system.

3.4 ELECTRON MICROSCOPY

3.4.1 Transmission Electron Microscopy

The transmission electron microscopic studies were carried out on a Philips 300 Transmission electron microscope operated at 100 kV.

The TEM specimen of different alloys (1.2 mm thick) were

abraded on different grades of SiC paper to a thickness of 0.1-0.2 mm. Discs of 3 mm diameter were punched out and thinned in a Tenupol jet thinning unit using a solution of 5% perchloric acid in methanol as the electrolyte. Electropolishing was carried out at -60°C at 12.5 volts and at a current density of $18-20 \text{ mA/mm}^2$. As soon as hole formation was indicated the specimen was quickly taken out, washed in ethanol-methanol and dried. When the specimen was left in electrolyte for more than a few seconds, copper tended to deposit on the specimen. The thin foils stored in dessicators remained free from oxides and could be re-examined after periods of several months.

3.4.2 Scanning Electron Microscopy

The mechanically polished and unetched metallographic specimens were examined in the back scattered mode in a JEOL-840 scanning electron microscope equipped with TN-5500 energy dispersive analysis (EDS) system.

3.4.2.1 Chemical Analysis

The EDS spectra from particles in metallographic specimens visible in the back scattered mode were used for rapid chemical analysis and to observe the effect of ageing. The electrochemically extracted insoluble particles were placed on a carbon replica supported on a Be-grid. In order to avoid inclusion of x-rays generated by the specimen holder, the Be-grid was placed on a carbon block which rested on a brass SEM specimen holder. Several EDS spectra were obtained

from different particles at different accelerating voltages and detector positions to optimize the spatial resolution of the x-ray signals and the efficiency of the production of characteristic x-rays. Generally for an efficient production of the x-rays the energy of electrons striking the specimen should be ≈ 2.5 times the energy of the particular characteristic x-ray. The x-ray spectra were obtained in the spot mode of the SEM from suitable locations in the extracted insolubles and particles visible in the metallographic specimens. The peaks in the x-ray spectra were identified and quantitative analysis was carried out by using Tracor Northern micro quantitative analysis (MICRO Q) program based on K-ratio and ZAF correction procedures. This program requires spectra from pure metal standards of interest which are acquired under similar conditions as unknown to give accurate chemical analysis.

3.4.2.2 Volume Fractions of Insoluble Particles

The volume fractions of insoluble particles were determined from bulk metallographic specimens of the alloys using back scattered images. The images were stored on a disk and analysed by using Tracor Northern Stored Image Analysis (SIA) program.

3.5 DIFFERENTIAL SCANNING CALORIMETRY (DSC)

The Du Pont 910 DSC instrument was used in this investigation. It consists of a cell base module connected to the 9900 programmer recorder. The DSC Cell plug into a cell base. A schematic diagram of the calorimeter cell is shown in Fig. 3.1. The cell employs a constantan disc as its primary means of heat transfer to the sample

DSC CELL CROSS — SECTION

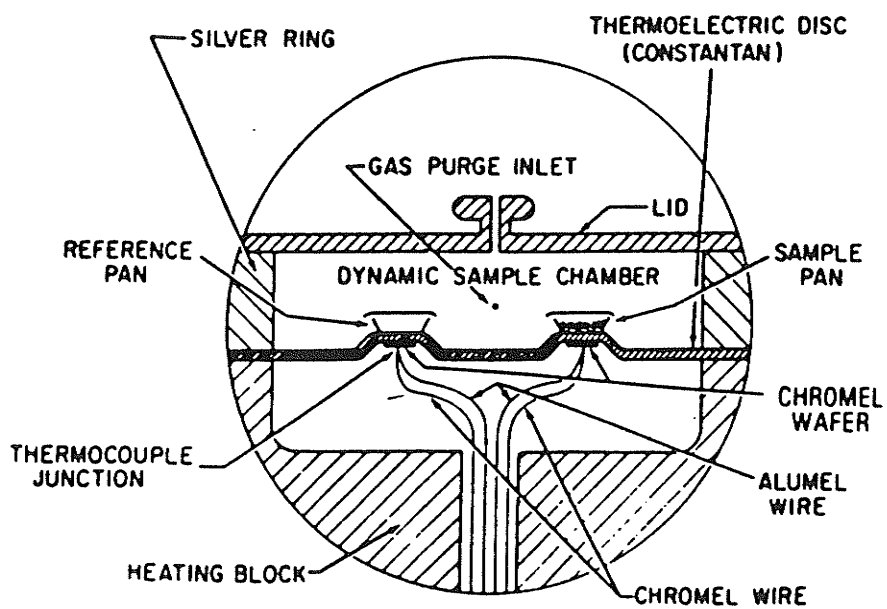


Fig. 3.1 Schematic diagram of the DSC cell

and reference positions, and as one element of the temperature measuring thermocouple. The samples and a reference are placed in pans which sit on raised platforms on the constantan disc. Heat is transferred through the disc and up into the sample and reference via the sample pans. The differential heat flow to the sample and reference is monitored by chromel-constantan area thermocouples formed by the junction of constantan disc and chromel wafer which covers the underside of the platforms. Chromel and alumel wires are connected to the underside of the chromel wafers, and the resultant chromel-alumel thermocouple is used to directly monitor the sample temperature. Hence, deviations from the programmed temperatures can be directly detected. The temperature of the environment of the sample is controlled by a sophisticated feedback control temperature programmer with its own thermocouple system located in the silver heating block. Purge gas is admitted to the sample chamber through an orifice in the heating block wall positioned midway between the two raised platforms. The purge gas enters the cell base at the rear and is preheated by circulation through the block before entering the sample chamber at the block temperature.

Specimens for use in the DSC were prepared from cold rolled strips ($\approx 80\%$) by cutting 5 mm dia discs in a spark cutting machine in order to avoid deformation.⁽¹⁶⁴⁾ The specimens were solution treated and water quenched. Appropriate ageing heat treatments were given to some of them. Heating rates of 5°C/min, 10°C/min, 15°C/min and 20°C/min were used. During each run, dry nitrogen at the rate of 30 ml/min was passed through the cell to avoid oxidation. Each experiment was performed twice and maxima and minima in the curves

were found to be reproducible to within $\pm 2^\circ\text{C}$. The overall shape of the DSC curve was also found to be highly reproducible.

3.6 X-RAY DIFFRACTION

The x-ray diffraction patterns from the extracted precipitate particles and the polished metallographic specimens of solution treated and quenched alloys were obtained using a 114.6 mm Debye-Scherrer camera with Ni-filtered Cu $K\alpha$ radiation at 40 kV. The specimens were exposed for about 8 h. The 'd' spacing of each reflection was calculated by the standard procedure used for powder diffraction analysis and the corresponding intensity was estimated by visual examination.

The reflections due to the insoluble particles were identified by comparing them with the reflections due to the synthetic quaternary compound. The lattice parameters of the alloys and the electrochemically extracted insoluble particles were determined by using a standard computer program based on the Cohen's least square method.⁽¹⁶⁵⁾ The Nelson-Riley extrapolation technique was also used to determine lattice parameters of the bulk alloys and extracted particles. Both methods gave similar results.

3.7 DENSITY MEASUREMENTS

The densities of the alloys were calculated from their respective lattice parameters. The density of 4.03 gm/c.c. for the synthetic quaternary compound was determined by measuring the loss of weight of a sample of the compound in a liquid. Ethyle iodide was found to be a satisfactory liquid for this purpose. In order to overcome errors due to internal porosity, the compound was finely

crushed, examined under a binocular microscope and transferred to a small container. The crushed pieces held in the container were evacuated in a vacuum chamber and the ethyle iodide was transferred into the container. A thin metal wire was used for suspending the container in the ethyle iodide. The length of the wire that was immersed in the liquid was always kept constant. This procedure and prolonged evacuation produced reproducible results. The density of liquid was also determined by weighing an Al block in distilled water and ethyle iodide. The densities of the liquid and the quaternary compound were measured at the same temperature. Atmospheric pressures noted and corrections due to air density were made. (166,167)

CHAPTER IV

PRECIPITATION IN THE Al-1.53%Cu-0.79%Mg ALLOY

4.1 MICROSTRUCTURAL CHARACTERIZATION

Specimens of the Al-1.53%Cu-0.79%Mg alloy were solution treated at 460°C for 10 min and water quenched. The optical micrograph (Fig. 4.1) of the as quenched specimen showed insoluble free single phase microstructure with an average grain size of $\approx 160 \mu\text{m}$. The as quenched specimens were then room temperature aged for 48 h followed by ageing at 130° and 190°C for various lengths of time. The microstructure of the aged specimens were examined by transmission electron microscopy.

4.1.1 Initial Stages of Ageing: Defect Structure and GPB Zones

Transmission electron microscopic studies showed that the solution treated and quenched specimen as well as those aged at room temperature for 48 h and further aged at 130°C up to 600 h and at 190°C upto 4 h contained appreciable amounts of quenched-in defects. A typical TEM micrograph obtained from a specimen aged at room temperature for 48 h shows the presence of dislocation loops and helical dislocations (Fig. 4.2). The latter have formed due to condensation of vacancies on the screw dislocations whereas the former form by condensation of vacancies into collapsed discs (Fig. 4.3) during or immediately after quenching from solution treatment temperature. The formation of dislocation loops has been discussed by Kuhlman-Wilsdorf⁽²²⁾ and Embury and Nicholson.⁽¹⁶⁸⁾ They have suggested that the Burgers vector of the dislocation loops is $a/2 \langle 110 \rangle$ and

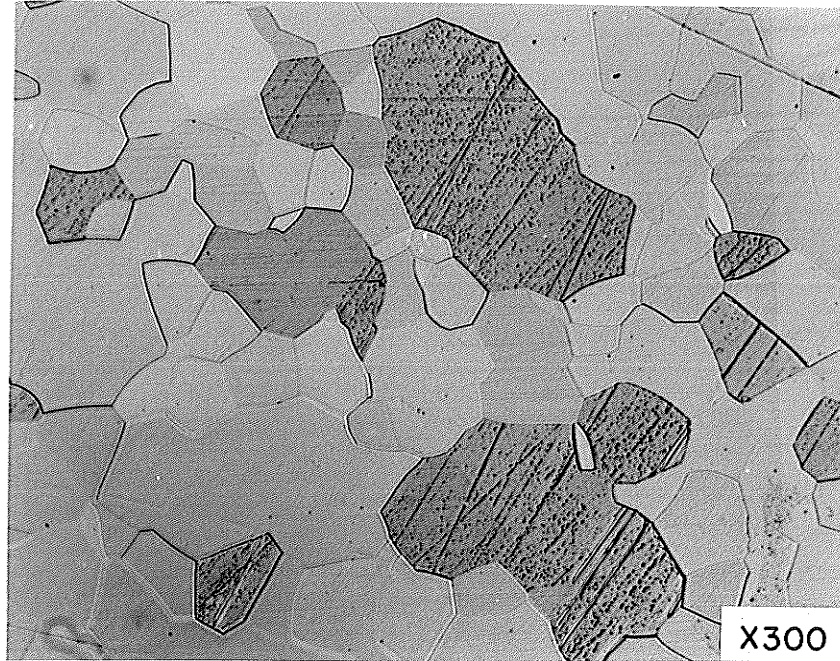


Fig. 4.1 Optical micrograph of the solution treated and water quenched Al-1.53%Cu-0.79%Mg alloy

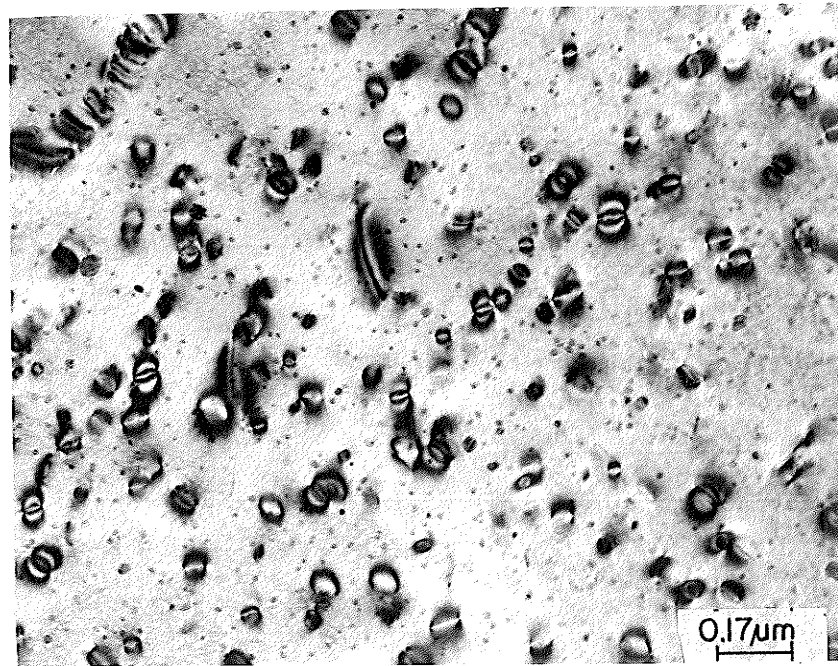


Fig. 4.2 Bright field image of the Al-1.53%Cu-0.79%Mg alloy aged at room temperature for 48 h

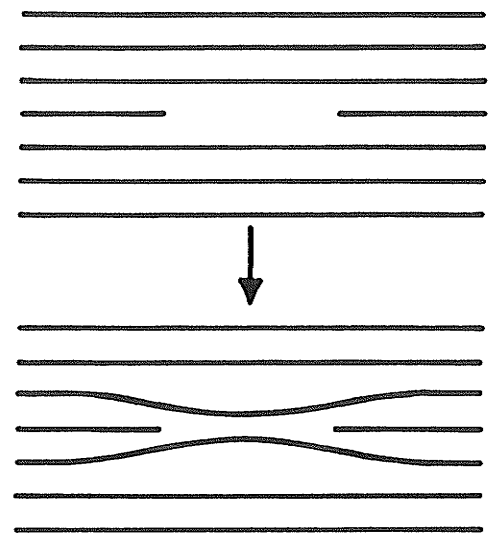


Fig. 4.3 The formation of a dislocation loop by the collapse of a disc of vacancies⁽²²⁾

they lie on $\{110\}_M$ planes. The presence of dislocation loops in the present alloy indicates that considerable amount of excess vacancies were retained during quenching. The thickness of the foil was estimated to be about 1500 Å. For this thickness of foil, the vacancy concentration was estimated to be of the order of $\approx 10^{-4}$. This value is similar to the values of the quenched-in vacancy concentration in pure aluminum⁽¹⁶⁹⁾ and ternary Al-3.2%Cu-1.5%Mg alloys.⁽¹⁷⁰⁾ Further ageing of the stabilized specimens up to 24 h at 130°C (Fig. 4.4) increased the size of dislocation loops, but the estimated vacancy concentration was not very much different from that in room temperature aged specimen. Increase of ageing time to 192 h and 288 h at 130°C seems to have caused the alignment of the loops along $\langle 100 \rangle_M$ direction and increased their sizes. These two factors have been interpreted to suggest that the dislocation loops have been decorated by solute atoms (Fig. 4.5). Ageing beyond 384 h showed clearly the presence of precipitate particles associated with dislocations (Fig. 4.6). Ageing of room temperature aged samples at 190°C produced decorated dislocation in them during the first 30 min of ageing. Further ageing for 2 h produced larger and fewer dislocation loops and helical dislocations (Fig. 4.7), while after 4 h of ageing specimens showed the presence of fine visible precipitates associated with dislocations (Fig. 4.8).

Wilson⁽¹²⁷⁾ and Horiuchi et al.⁽¹⁷¹⁾ have suggested that these excess vacancies assist the diffusion of Cu and Mg complexes. The sum of the atomic diameters of Cu (0.2556 nm) and Mg (0.3196 nm) is approximately twice that of the atomic diameter of aluminum, so that the formation of Cu-Mg complexes in equiatomic 1:1 ratio may

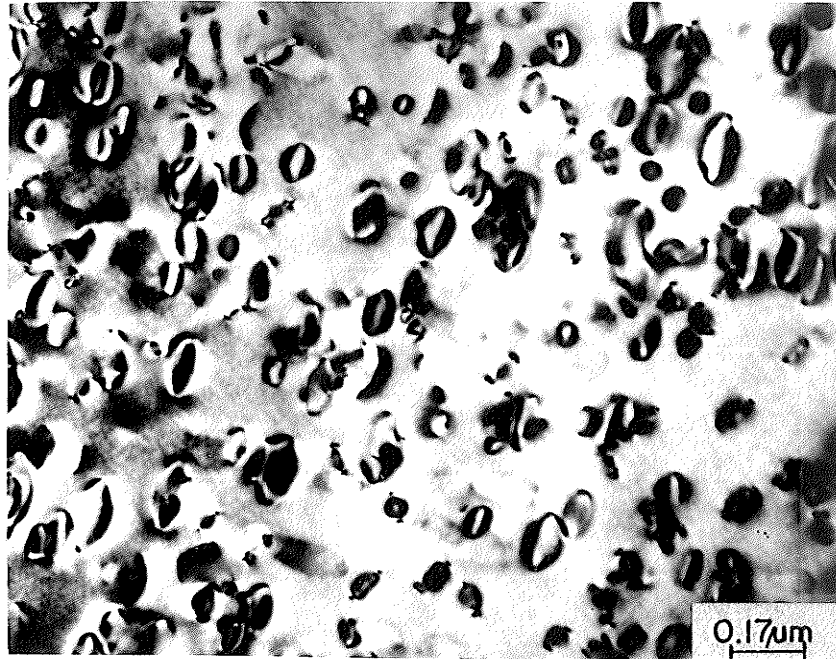


Fig. 4.4 Bright field image of the Al-1.53%Cu-0.79%Mg alloy aged at room temperature and further aged at 130°C for 24 h

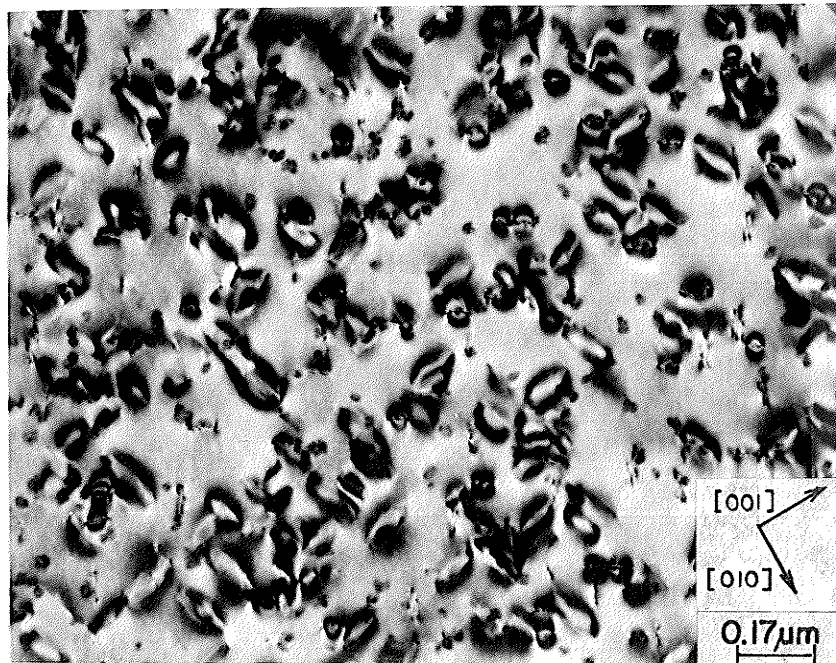


Fig. 4.5 Bright field image of the Al-1.53%Cu-0.79%Mg alloy aged at room temperature for 48 h and further aged at 130°C for 288 h

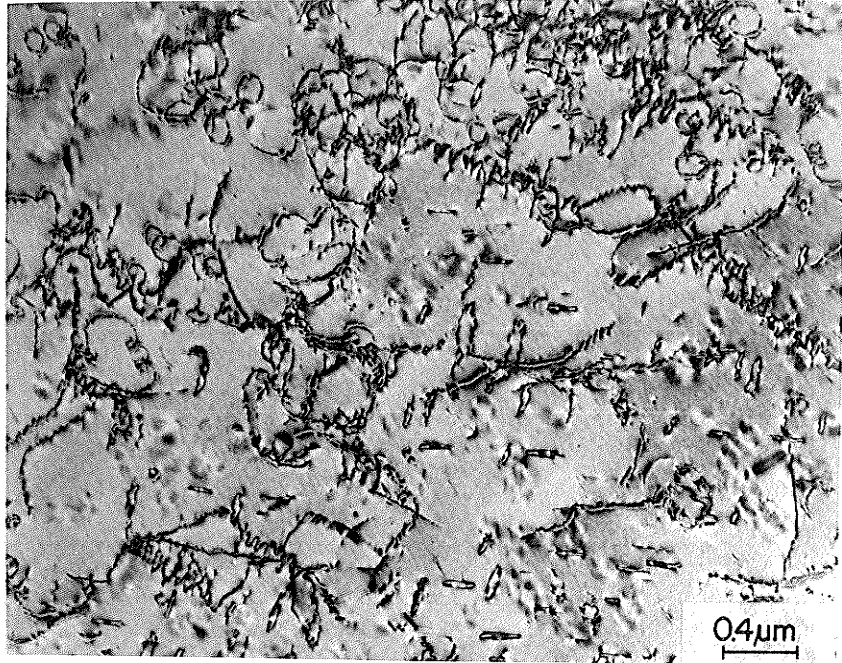


Fig. 4.6 Bright field image of the Al-1.53%Cu-0.79%Mg alloy aged at room temperature for 48 h and further aged at 130°C for 600 h

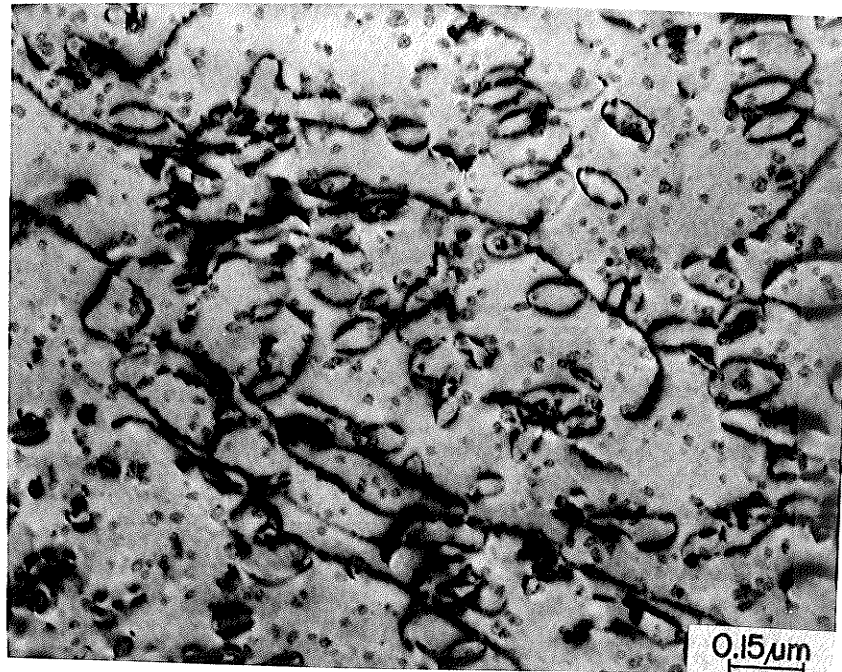


Fig. 4.7 Bright field image of the Al-1.53%Cu-0.79%Mg alloy aged at room temperature for 48 h and further aged at 190°C for 2 h

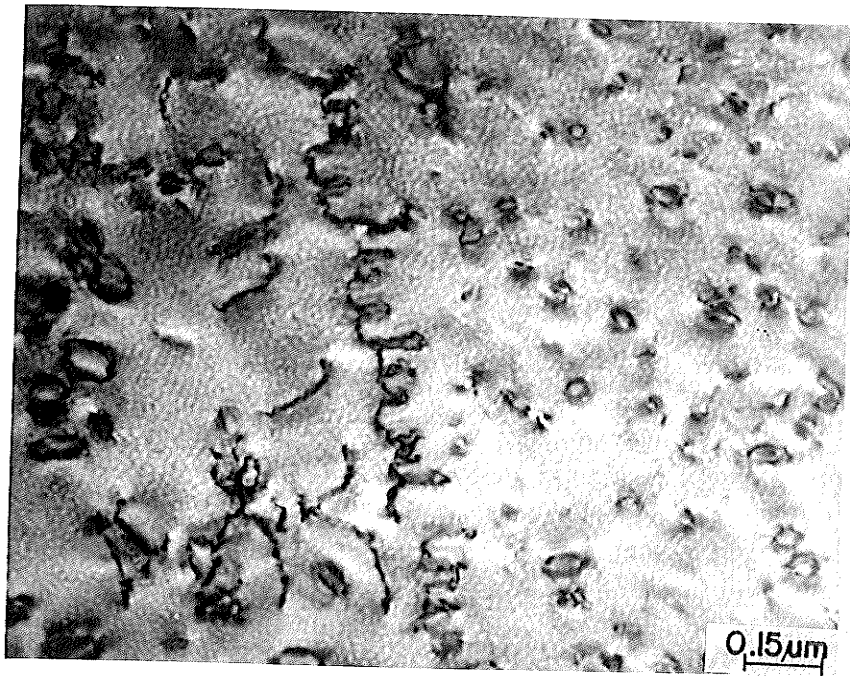
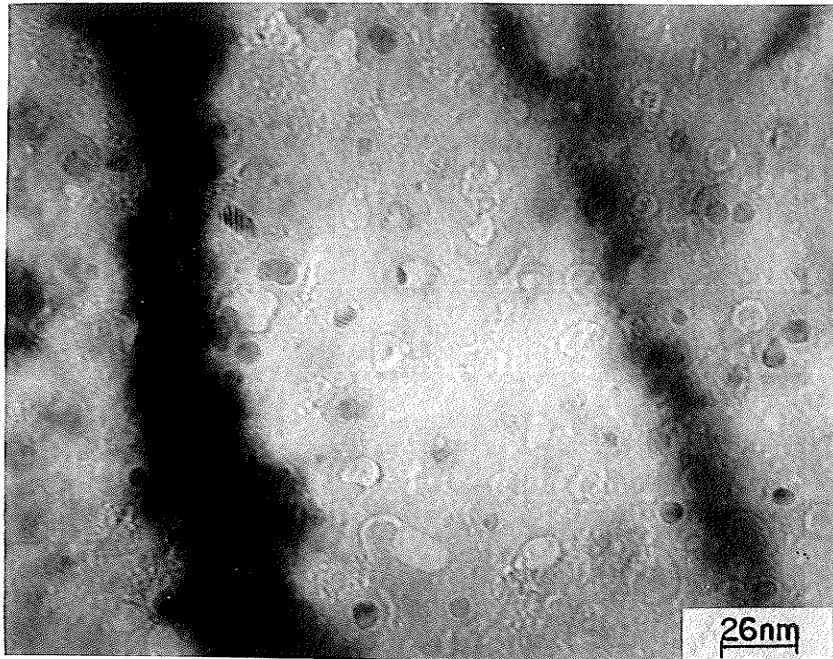


Fig. 4.8 Bright field image of a specimen aged at room temperature for 48 h followed by ageing at 190° for 4 h.

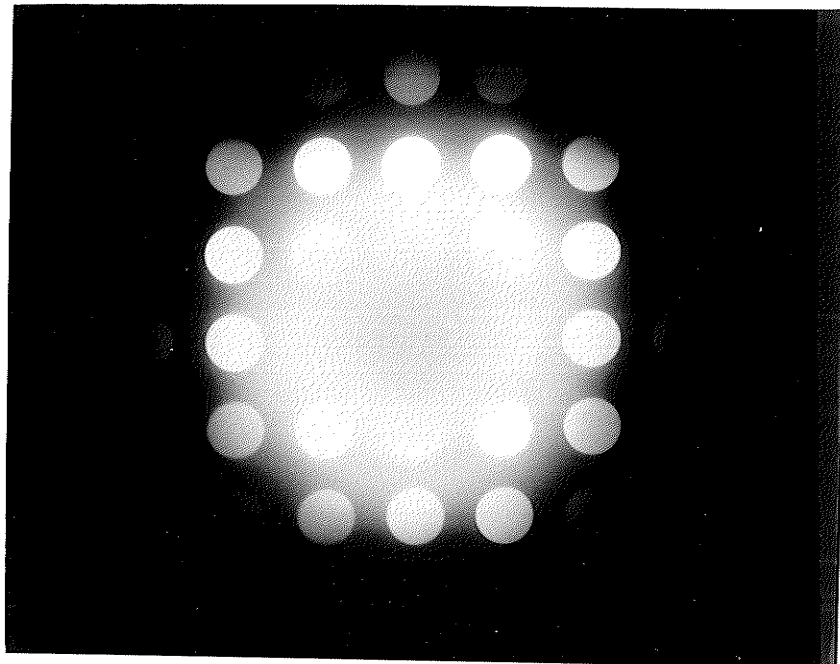
be expected to reduce lattice strain.⁽¹⁷⁰⁾ Therefore, one might also expect GPB zones to be formed in the initial stages of ageing of this alloy. These zones are too small to be resolved in the Philips 300 transmission electron microscope used in this investigation. Thus, a few specimens of the alloy were examined in the JEOL-200 FX transmission electron microscope operated at 200 kV. A typical micrograph obtained from a specimen aged at 130°C for 16 h is shown in Fig. 4.9(a) with its SADP in Fig. 4.9(b). The microstructure shows GPB zones fringes suggesting them to be cylindrical, (10-20 Å in diameter) and lying along $\langle 100 \rangle_M$ direction. These observations are consistent with the x-ray studies of Bagaryatsky⁽¹²¹⁾ and Silcock⁽¹²²⁾ who reported them to be of cylindrical shape (1-2 nm dia) lying along $\langle 100 \rangle_M$ directions. High resolution lattice imaging studies of Takahashi and Sato⁽¹³⁵⁾ also showed similar results.

4.1.2 Formation of the S' Phase

The first clear indication of the presence of second phase particles were seen in specimens aged for more than 384 h at 130°C and 4 h at 190°C. A typical bright field image obtained from a specimen aged for 4 h at 190°C is shown in Fig. 4.10(a). The precipitate particles are not clearly visible, however, strain field contrast, which could be due to the presence of coherent precipitate is observed. The coherency strains also gave the surface a mottled appearance. The presence of precipitate particles was confirmed by the presence of faint streaks (encircled) in the SAD pattern shown in Fig. 4.10(b). These streaks are parallel to $\langle 100 \rangle_M$ direction. Further ageing of the specimens at 190°C resulted in the growth of these particles (Fig.

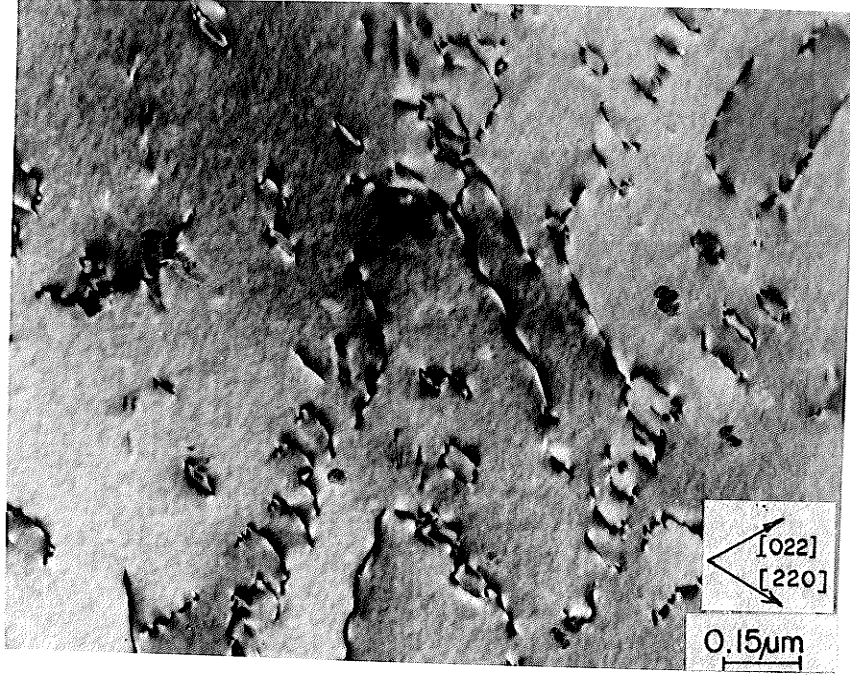


(a)



(b)

Fig. 4.9 (a) Bright field image of the Al-1.53Cu-0.79Mg alloy aged at room temperature for 48 h and further aged at 130°C for 16 h
(b) The corresponding SAD pattern



(a)



(b)

Fig. 4.10 (a) Bright field image of the Al-1.53%Cu-0.79%Mg alloy aged at room temperature for 48 h and further aged at 190°C for 4 h
(b) The SAD pattern of (a). The streaks due to precipitates are encircled

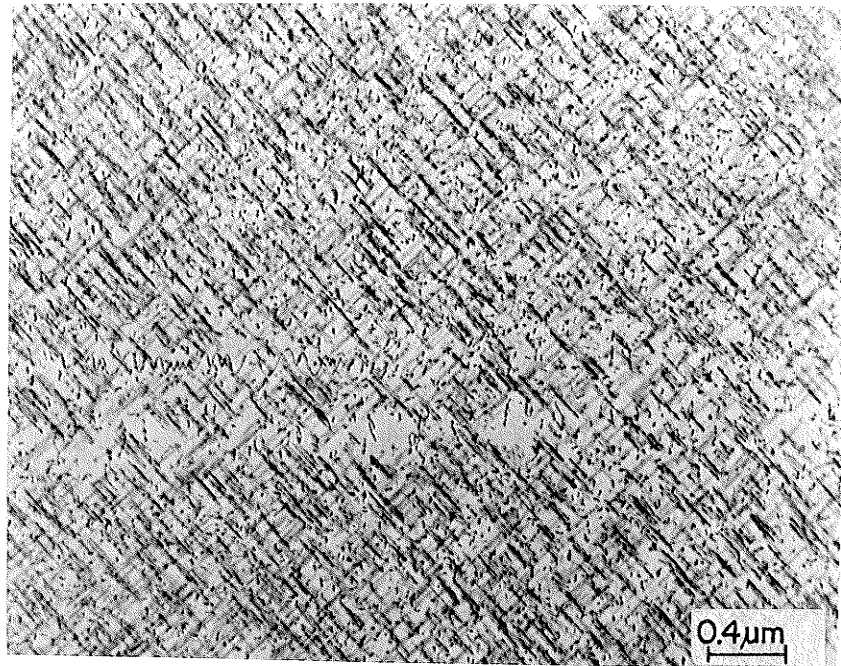
4.11(a)) and the SAD pattern showed definite precipitate reflections in Fig. 4.11(b). The precipitate reflections can be indexed as due to the orthorhombic S' phase by a method discussed in Section 4.1.2.2. The advanced stage of ageing at 130°C for 768 h also showed similar features (Fig. 4.12(a) and (b)). The identification of the precipitates is in agreement with the conclusions of an x-ray diffraction study by Bagaryatsky⁽¹²³⁾ and Silcock⁽¹²²⁾ on Al-Cu-Mg alloys with a Cu/Mg ratio of 2.2:1.

4.1.2.1 Nucleation of the S' Phase

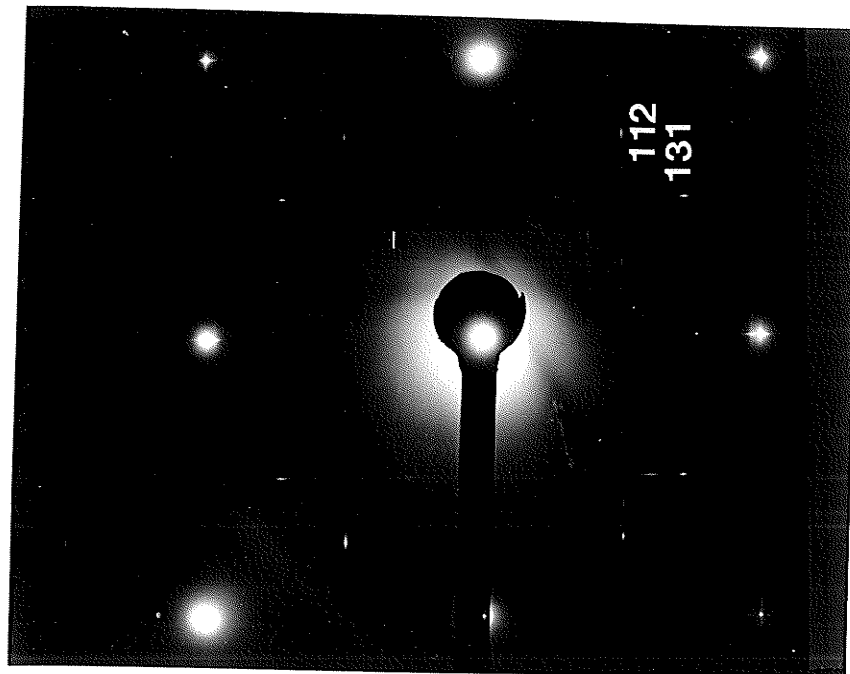
The bright field image obtained from a specimen aged for 600 h at 130°C showed the S' phase to be associated with dislocations (Fig. 4.13(a) and (b)). It can be more clearly seen in Fig. 4.14 which is a micrograph of a specimen aged at 130°C for 288 h. The S' phase has nucleated on (110) planes with a tendency to grow along [001] direction. This observation is consistent with the models of Alekseyev et al.⁽¹³⁰⁾ shown in Fig. 4.15 and of Wilson and Partridge.⁽²³⁾ The S' precipitates also nucleate on helical dislocations as evidenced by the trace of helical dislocation on the micrograph shown in Fig. 4.11(a). Thus, it can be concluded that dislocations are primarily responsible for the nucleation of the S' phase.

4.1.2.2 Theoretical Prediction of the Electron Diffraction Pattern of the S' Phase

A typical example of the microstructure of a specimen aged for 168 h at 190°C is shown in Fig. 4.16(a) with its SAD pattern in Fig. 4.16(b). The analysis of the SAD pattern due to matrix suggests



(a)

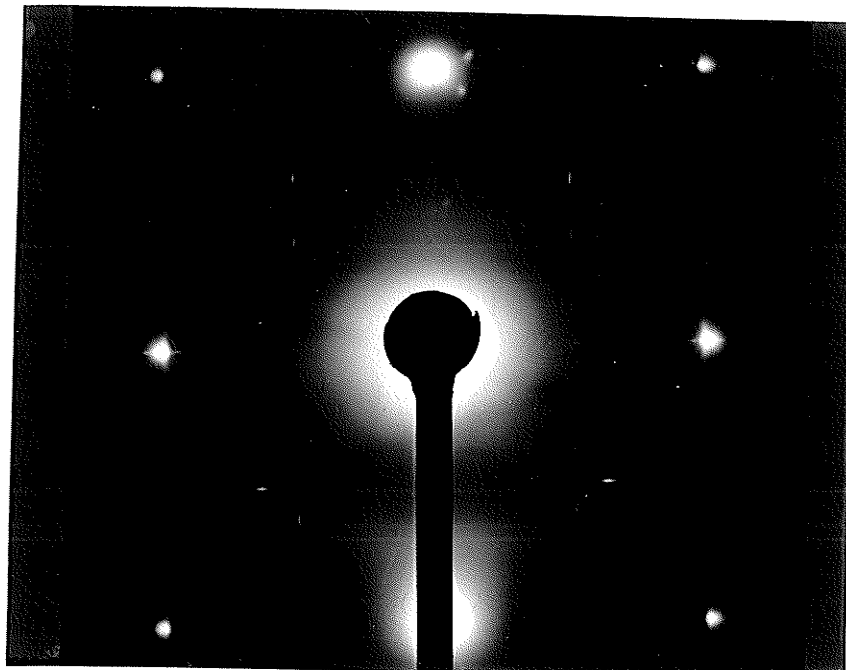


(b)

Fig. 4.11 (a) Bright field image of the Al-1.53%Cu-0.79%Mg alloy aged at room temperature for 48 h and further aged at 190°C for 6 h. The traces of helical dislocation are visible
(b) The SAD pattern of (a)

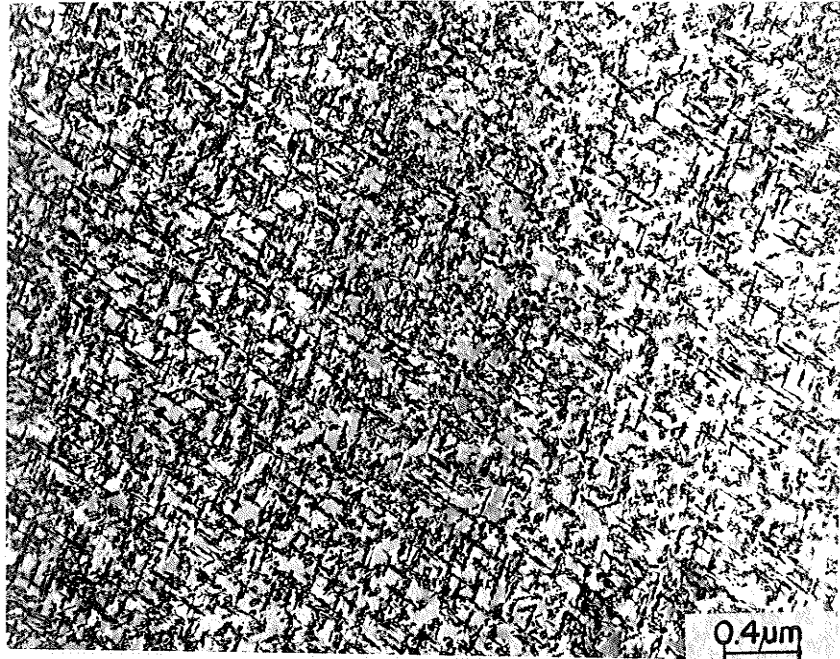


(a)

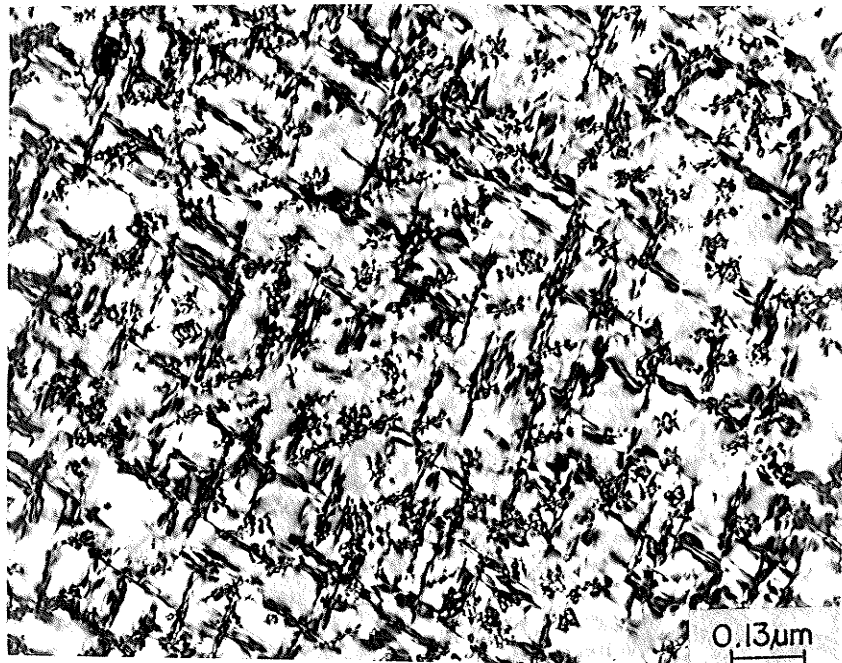


(b)

Fig. 4.12 (a) Bright field image of the Al-1.53%Cu-0.79%Mg alloy aged at room temperature for 48 h and further aged at 130°C for 768 h
(b) The SAD pattern of (a)



(a)



(b)

Fig. 4.13 (a) Bright field image of the Al-1.53%Cu-0.79%Mg alloy aged at room temperature for 48 h and further aged at 130°C for 600 h

(b) Same area as in (a) at a higher magnification

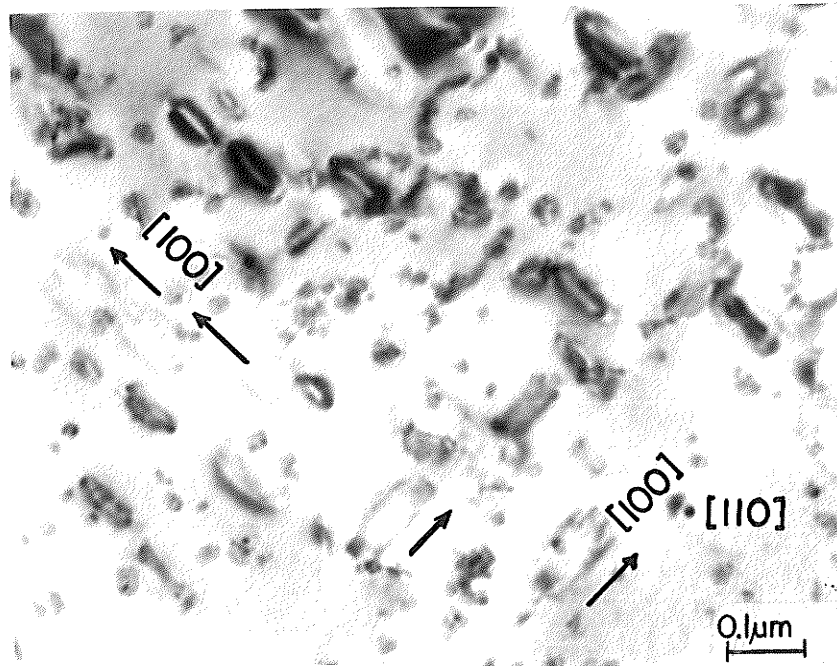


Fig. 4.14 Bright field image of the Al-1.53%Cu-0.79%Mg alloy aged at room temperature for 48 h and further aged at 130°C for 288 h. Nucleation of the S' phase on loops is marked by arrows

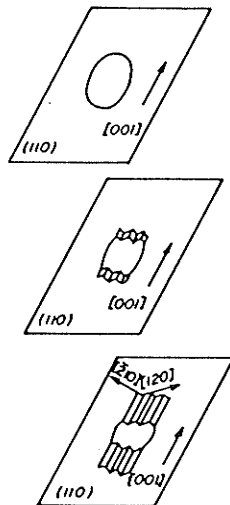
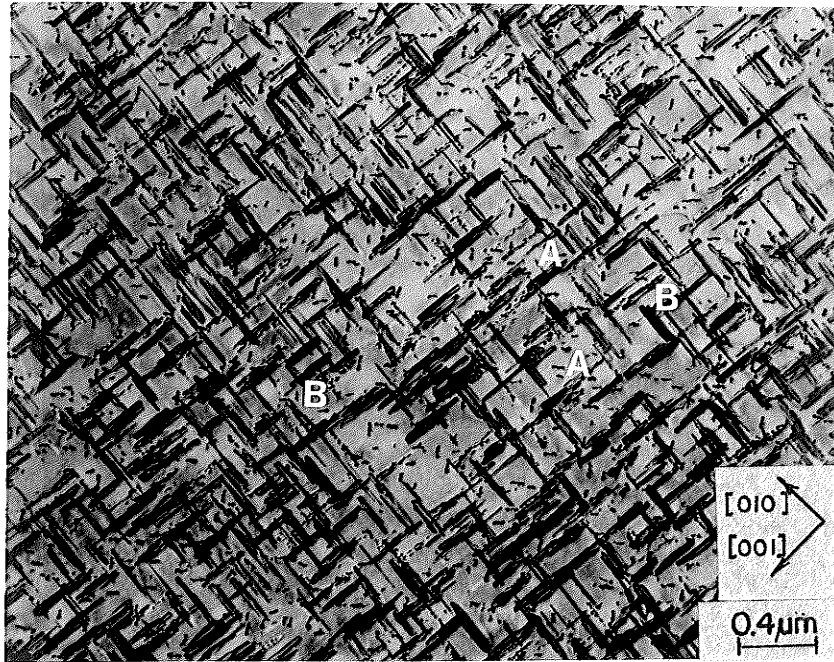
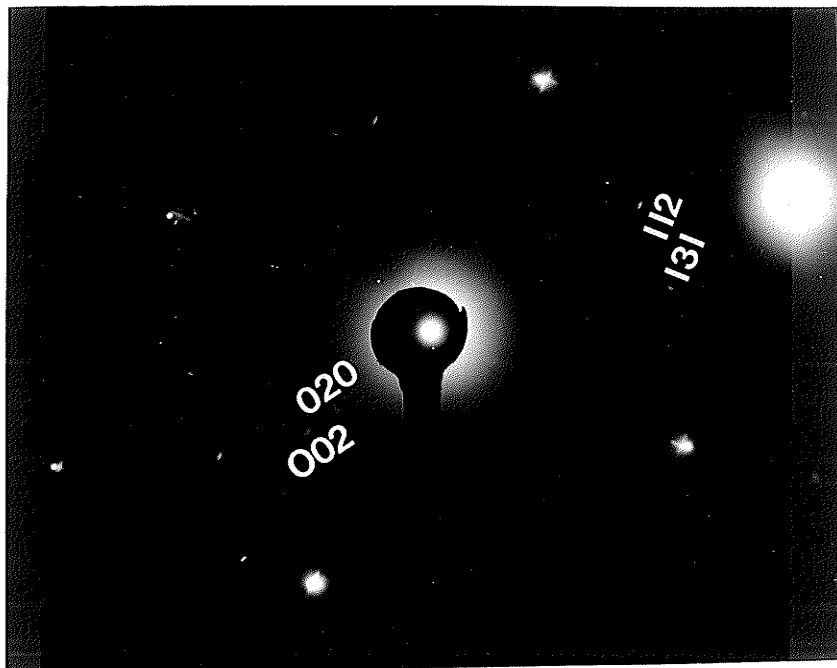


Fig. 4.15 Schematic diagram of a suggested sequence for the nucleation of the S' phase⁽¹³⁰⁾



(a)



(b)

Fig. 4.16 (a) Rod shaped S' precipitates in the Al-1.53%Cu-0.79%Mg alloy aged for 168 h at 190°C. Groups of 'end on' precipitates parallel to $\langle 110 \rangle$ and $\langle 100 \rangle$ are marked A and B, respectively
(b) SAD pattern from an area similar to that shown in (a). {020}, {002}, {112} and {131} reflections of the S' precipitates are marked

the thin foil to be in [100] orientation, however, the diffraction pattern due to the precipitates is very complex. The SAD pattern can be interpreted by simulating a theoretical diffraction pattern using known orientation relationships as described below.

The following orientation relationships between S' and the matrix were established by Bagaryatsky⁽¹²¹⁾ and Silcock⁽¹²²⁾ using the x-ray diffraction technique,

$$[100]_{S'} \parallel [100]_M ; [010]_{S'} \parallel [021]_M ; [001]_{S'} \parallel [01\bar{2}]_M$$

If the [100] direction of a single crystal of fcc matrix phase is parallel to the [100] direction of S' phase, four possible variants of S' are possible. This occurs because there are four <021> matrix directions which are at 90° to [100]_M and can become 'c' direction of S' phase. These directions are [0 $\bar{1}2$]_M, [021]_M, [0 $\bar{2}1$]_M and [012]_M. These four orientations are referred to as variant 1, 2, 3 and 4 respectively. Since there are three <100>_M axes which can be chosen as parallel to [100]_{S'}, there are a total of 12 possible crystallographic variants of the S' phase from a single crystal of matrix phase. The four variants 1, 2, 3 and 4 which arise from the matrix-S' orientation relationship of [100]_M || [100]_{S'}, are shown in a stereogram in Fig. 4.17.

Based on the structure of the S' phase its strongest reflections are expected to be 131, 020, 200, 111 and 112. Considering the variants with [100]_M || [100]_{S'}, only those g_{S'}, reciprocal lattice vectors of S' phase, lying almost perpendicular to the [100]_M beam direction will be able to satisfy the Bragg diffraction condition. The simplest way to check this condition is to form a transformation

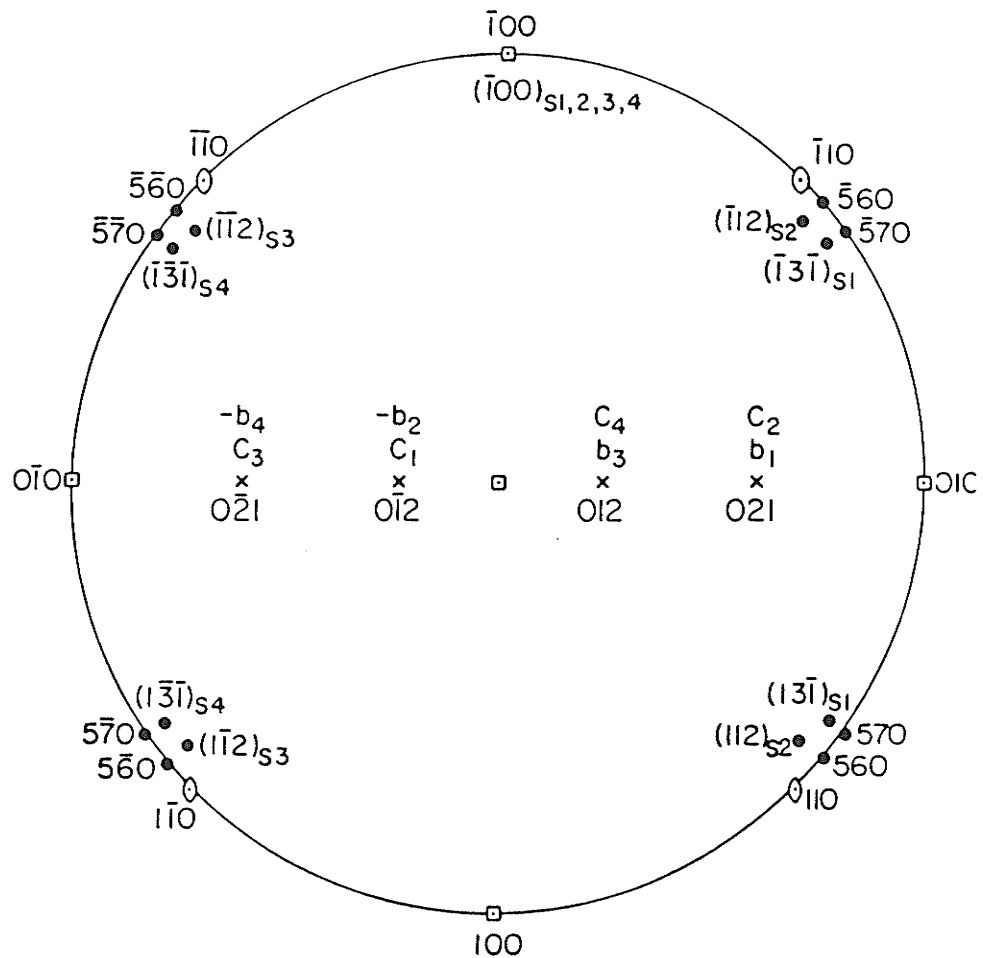


Fig. 4.17 Stereogram showing the b and c axis directions of four orthorhombic S' variants sharing a common 'a' axis direction parallel to $[100]$ in the parent cubic crystal. The directions of $g_{S'}$ vectors for $\{112\}_{S'}$ and $\{131\}_{S'}$ reflections from the four variants are also shown (round brackets). The matrix directions are unbracketed

matrix to convert plane normals in the S' phase to the directions referred to as the face centred cubic matrix phase. In the S' phase the (h, k, l) plane normal is parallel to the direction $[h/a, k/b, l/c]_{S'}$. Thus for variant 2, expressing the S' phase plane normals as row vectors,

$$[100]_M \rightarrow [100]_{S'}$$

$$\left[\frac{0\bar{1}\bar{2}}{\sqrt{5}}\right]_M \rightarrow [010]_{S'}$$

$$\left[\frac{0\bar{2}1}{\sqrt{5}}\right]_M \rightarrow [001]_{S'}$$

the transformation matrix is:

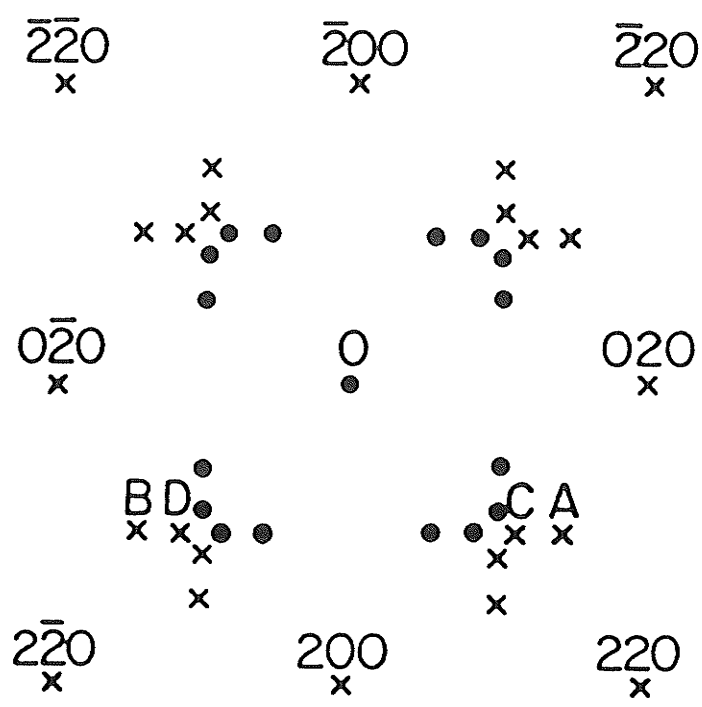
$$S' \approx M = \begin{vmatrix} 1 & 0 & 0 \\ 0 & 1/\sqrt{5} & -2/\sqrt{5} \\ 0 & 2/\sqrt{5} & 1/\sqrt{5} \end{vmatrix}$$

For this variant only the strong reflections $(112)_{S'}$ and $(\bar{1}\bar{1}\bar{2})_{S'}$ have $g_{S'}$ vector nearly perpendicular to $[001]_M$. They are parallel to the unit normals $[0.6398, 0.7651, 0.726]_M$ and $[0.6398, 0.7651, \overline{0.726}]_M$ which are calculated to be lying at $\mp 4.16^\circ$ respectively from the $(001)_M$ plane. Similarly for variant 4, $(\bar{1}\bar{3}\bar{1})_{S'}$ and $(131)_{S'}$ are the only visible reflections lying at $\mp 2.5^\circ$ to the $(001)_M$ plane. These $g_{S'}$ vectors are lying sufficiently close to the foil plane to give Bragg reflections. For variant 3, $(11\bar{2})_{S'}$ and $(\bar{1}\bar{1}2)_{S'}$ are favoured reflections and $(13\bar{1})_{S'}$ and $(\bar{1}\bar{3}1)_{S'}$ are favoured reflections for variant 1. These eight reciprocal lattice vector directions are also plotted on the standard stereographic projection in Fig. 4.17. It is observed that the $\{112\}_{S'}$ vectors have projections in the $(001)_M$ plane close to $[560]_M$, $[5\bar{6}0]_M$, $[\bar{5}\bar{6}0]_M$ and $[\bar{5}60]_M$ and the $\{131\}_{S'}$ vectors close to $[570]_M$, $[5\bar{7}0]_M$, $[\bar{5}\bar{7}0]_M$ and $[\bar{5}70]_M$.

There are also four similar S' phase variants with $[010]_M \parallel [100]_{S'}$, and these will produce diffraction spots rotated about $[001]$ by 90° relative to the $[100]_M \parallel [100]_{S'}$ variants discussed above.

The stereogram in Fig. 4.17 shows the directions of all the $g_{S'}$ vectors lying in, or close to, the $(001)_M$ plane. The simulated diffraction pattern of Fig. 4.18 was constructed by plotting lines parallel to these $g_{S'}$ vectors through the centre of the pattern and placing diffraction spots at a distance from the origin proportional to the length of the $g_{S'}$ vector under consideration. The crosses mark primary reflections and the solid circles show precipitate double diffraction spots caused by strong matrix reflections. The reflections A, B, C and D represented by crosses are primary reflections due to the S' phase. The origin of these primary reflections is given in the Table included in Fig. 4.18. The primary and double diffraction spots around the "forbidden" $\{110\}_M$ reflections give a characteristic grouping of 8 diffraction spots due to the S' phase. The theoretical diffraction pattern is in close agreement with the observed diffraction pattern shown in Fig. 4.16(b). The presence of double diffraction spots depends critically upon the value of the deviation parameter S_g which is governed by the thickness of the foil and the angle of tilt. Tilting of the $\{001\}_M$ foil weakens the matrix reflections and causes some of the double diffraction spots shown in Fig. 4.16(b) to disappear - which is in agreement with observations reported by Chester. (151)

The four variants with $[001]_M \parallel [100]_{S'}$ are simple to analyse since for these 4 variants, S'-phase $g_{S'}$ vectors of the type $(0 k l)_{S'}$,



A		(13 $\bar{1}$) ₁ , (131) ₄	Angle COD = 100.5°
B		(1 $\bar{3}$ 1) ₁ , (1 $\bar{3}\bar{1}$) ₄	Angle AOB = 109.5°
C		(112) ₂ , (11 $\bar{2}$) ₃	
D		(1 $\bar{1}\bar{2}$) ₂ , (1 $\bar{1}$ 2) ₃	

Fig. 4.18 Interpretation of diffraction pattern with [001] matrix beam direction. The crosses represent primary reflections while solid circles are double diffraction spots. The variants contributing to reflections A, B, C and D are listed in the Table below

will lie in the $(001)_M$ foil plane. The strong S' reflections of this type are expected to be, in order of decreasing intensity, 020, 002, 042, 022 and 021. Their predicted positions on the $(001)_M$ great circle can be calculated using the appropriate rotation matrix. These variants 9, 10, 11 and 12 have $[001]_M \parallel [100]_{S'}$. For variant 9 with $[210]_M \parallel [010]_{S'}$ and $[\bar{1}20]_M \parallel [001]_{S'}$, the matrix which transforms S' g-vectors to directions referred to the matrix axes is,

$$T \\ S \approx M = \begin{vmatrix} 0 & 0 & 1 \\ 2/\sqrt{5} & 1/\sqrt{5} & 0 \\ 1/\sqrt{5} & -2/\sqrt{5} & 0 \end{vmatrix}$$

For variant 9 the in-foil unit vector from the $(0\ k\ 1)_{S'}$ plane is parallel to:

$$\frac{1}{\sqrt{5}} \left[\left(\frac{2k}{b} + \frac{1}{c} \right), \left(\frac{k}{b} - \frac{2l}{c} \right), 0 \right]_M$$

Thus $(020)_{S'} \parallel (210)_M$ for variant 9 and it does not overlap $(002)_{S'}$ reflections from other variants. Overlapping reflections do not in fact occur for variants 9, 10, 11 and 12. The S' reflections $(002)_{S'}$ and $(020)_{S'}$ are marked on the diffraction pattern of Fig. 4.16(b). The $(002)_{S'}$ reflection comes from variant 9 and the $(020)_{S'}$ from variant 12, as their $g_{S'}$ vectors being parallel to $[\bar{1}20]_M$.

Recently, Cusiat, Duval and Graf⁽¹⁴⁶⁾ have attempted to interpret the "superlattice" spots in Fig. 4.16(b) as periodic antiphase domain satellites rather than being due to double diffraction. However, they did not show convincing evidence of the presence of periodic antiphase domain images to support their interpretation. It is,

therefore, concluded that satellite spots in Fig. 4.16(b) are due to double diffraction phenomenon as had been earlier suggested by Weatherly and Nicholson⁽⁹⁴⁾ and Hirsch, Howie, Nicholson, Pashley and Whelan.⁽¹⁷²⁾

4.1.2.3 Analysis of SAD Patterns and Morphology of the S' Phase

In order to confirm the theoretical predictions of simulated diffraction pattern and to study morphological development of the S' phase, bright field and centred dark field (CDF) images were examined and lattice parameters were measured from SAD patterns obtained from specimens aged for various times at 190°C.

4.1.2.3.1 Morphology From Bright Field Images

In the bright field image of an $(001)_M$ foil (Fig. 4.16(a)), rods of the S' phase parallel to $[010]_M$ and $[100]_M$ directions in the plane of the foil and perpendicular to the foil $[001]_M$ are clearly visible. These rods are circular in cross-section with a diameter of $\approx 90 \text{ \AA}$. This dimension is consistent with the streaking of the $(020)_{S'}$ and $(002)_{S'}$ reflections in Fig. 4.16(b) in $[120]_M$ and $[210]_M$ directions. Despite the long ageing time of 168 h at 190°C the rods have not coalesced to form laths, although there is some tendency for rods to group together parallel to (110) and $(\bar{1}\bar{1}0)$ matrix planes and occasionally parallel to (100) and (010) matrix planes. These features are most clearly seen in the four "end-on" variants. The average length of the rod is $\approx 90 \text{ \AA}$, giving a rod volume of $\approx 1.146 \times 10^7 \text{ \AA}^3$. By observing the projections of the rod images in a $\{110\}_M$ foil, the foil thickness was estimated to be 1525 \AA .

4.1.2.3.2 Interpretation of Centred Dark Field (CDF) Images

The analysis in Section 4.1.2.2 clearly implies that CDF images formed using the diffraction spots A and B of Fig. 4.18 will show variants 1 and 4 of S' phase, while C and D will light up variants 2 and 3. Figs. 4.19(a), (b), (c) and (d) show CDF images using the A, B, C and D reflections shown in Fig. 4.18, while Figs. 4.19(e) and (f) are taken from $(002)_{S'}$ and $(020)_{S'}$ spots shown in Fig. 4.16(b). The CDF images from all six reflections highlight S' rods parallel to $[100]$ matrix directions. Since both B and A reflections come from the same two variants, 1 and 4 they light up some identical rods in the images, which are marked with X in Figs. 4.19(b) and 4.19(a). Similar common features occur in the images using reflection D and C from variants 2 and 3 and marked Y in Figs. 4.19(d) and 4.19(c). Some rods in Fig. 4.19(a) are, however, also weakly visible in Fig. 4.19(c), and are marked X1. Similarly, some strongly lit rods in Fig. 4.19(c) also appear weakly in Fig. 4.19(a) and are marked Y1. Less obvious "ghosts" are observed between Fig. 4.19(c) and 4.19(d). Great care was taken not to shift the specimen as the different CDF images were formed from the diffraction pattern shown in Fig. 4.20(a). Fig. 4.20(b) shows the bright field image. The weak coincidences arise because the diffraction aperture had a reciprocal lattice diameter of $\approx 0.018 \text{ \AA}^{-1}$, which is close to the 0.017 \AA^{-1} separation of the spots B-D and C-A in Fig. 4.18. This fact together with the 90 \AA diameter of the rods and their associated 0.011 \AA^{-1} diameter reldiscs, did not allow spot C to be isolated without including part of the reldisc of spot A to give weak ghosts of A rods in Fig. 4.19(c). The CDF images formed using the diffraction spots $(002)_{S'}$ and $(020)_{S'}$



(a)



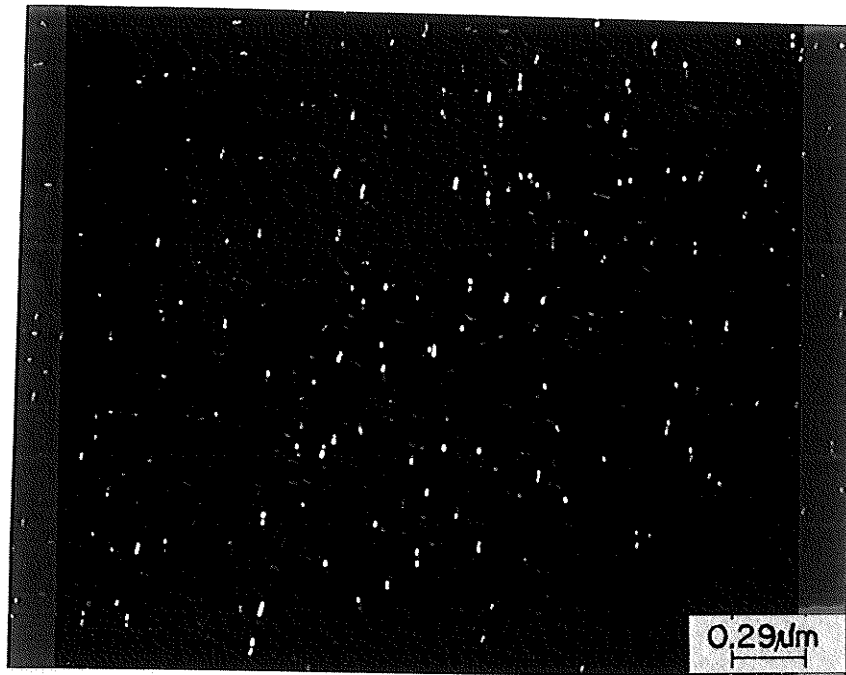
(b)



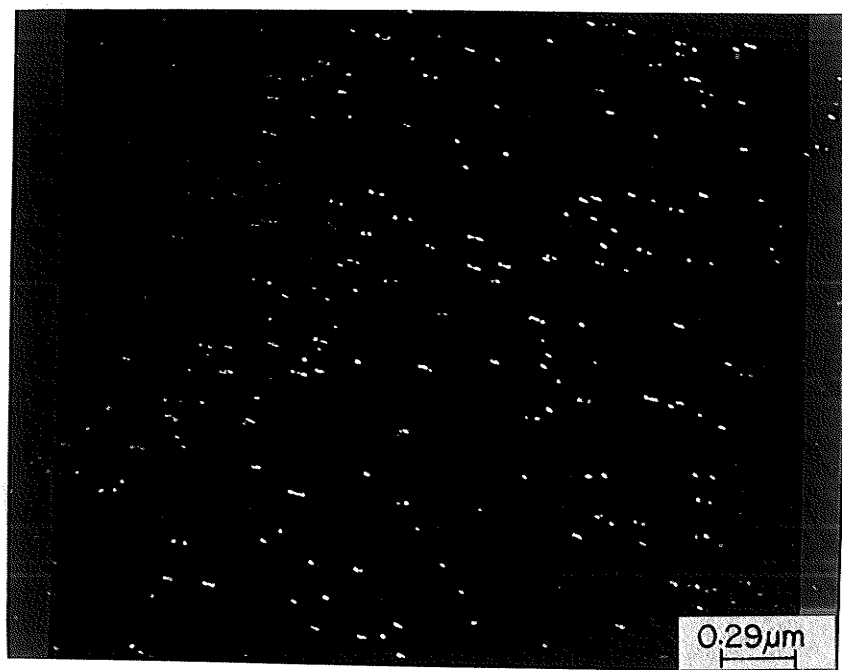
(c)



(d)



(e)



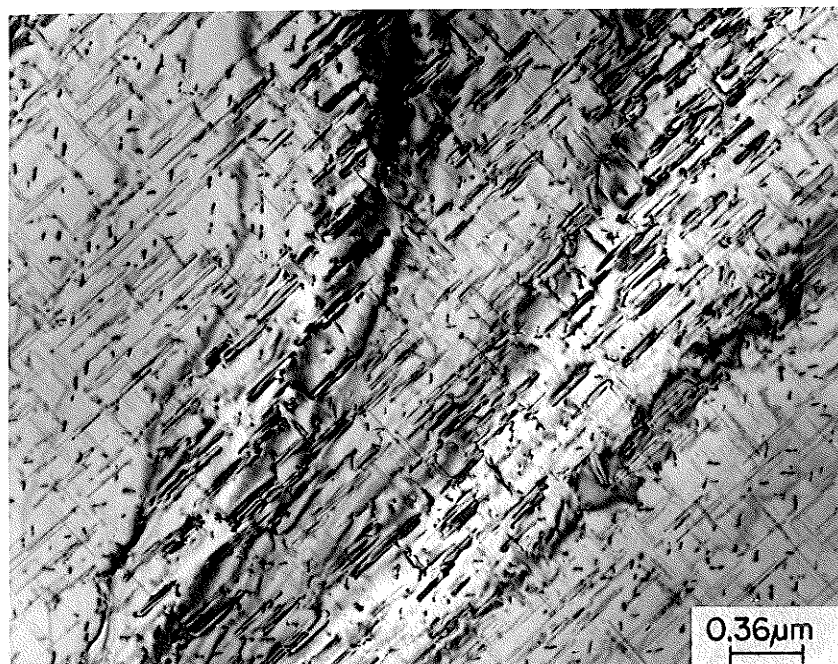
(f)

Fig. 4.19 Centred dark field images of the alloy aged for 168 h at 190°C. (a), (b), (c) and (d) are taken with the A, B, C and D reflections shown in Fig. 4.18, while (e) and (f) are taken with $\{002\}_S$, and $\{020\}_S$, shown in Fig. 4.16(b).

Some of the precipitates (marked X) are common to (a) and (b). Similar features (marked Y) are common to (c) and (d). Rods in (a) which appear weakly in (c) are marked X1 and rods in (c) weakly appearing in (a) are marked Y1



(a)



(b)

Fig. 4.20 (a) SAD pattern used to produce the centred dark field images of Fig. 4.19. (b) is a bright field image from the same pattern